1-28-2015

A Biomechanical Analysis of One-Third Tubular Plates for the Treatment of Benign Lesions in the Distal Femur

Justin Brantley

Justin A. Brantley

Candidate

Biomedical Engineering

Department

This thesis is approved, and it is acceptable in quality and form for publication:

Approved by the Thesis Committee:

Mahmoud Reda Taha , Chairperson

Elizabeth Dirk

David H. Chafey

A Biomechanical Analysis of One-Third Tubular Plates for the Treatment of Benign Lesions in the Distal Femur

by

Justin A. Brantley

B.S., Mechanical Engineering, New Mexico State University, 2011

THESIS

Submitted in Partial Fulfillment of the
Requirements for the Degree of

Master of Science
Biomedical Engineering

The University of New Mexico

Albuquerque, New Mexico

December, 2014

Dedication

To my family for their endless love, support, and encouragement. Without you, I would not have accomplished all that I have thus far.

Acknowledgments

I would like to thank my advisor, Professor Mahmoud Reda Taha, for his guidance and support, and for supporting my research and education. I would like to thank Dr. Robert Schenck, Mary Jacintha, and the Department of Orthopaedics & Rehabilitation for allowing me to work as a researcher in the department, and for the financial support of this project and many others. Thank you to my committee members, Dr. David H. Chafey and Dr. Elizabeth Dirk, for the time they have committed to this thesis. I would like to acknowledge Dr. Robert Quinn for developing this project and for providing support throughout this entire study. Thank you to Dr. Heather Menzer and Dukens LaBaze for all of their assistance and guidance on this project. Thank you to James Love for manufacturing some of the components of the experimental fixture. I would like to acknowledge Dr. Deana Mercer for endlessly supporting this and many other research projects within the department. Special thanks to Dr. Christina Salas for all her guidance and support and for being a colleague, mentor, and friend.

A Biomechanical Analysis of One-Third Tubular Plates for the Treatment of Benign Lesions in the Distal Femur

by

Justin A. Brantley

B.S., Mechanical Engineering, New Mexico State University, 2011

M.S., Biomedical Engineering, University of New Mexico, 2014

Abstract

The purpose of this study was to evaluate the use of one-third tubular plates for the treatment of benign defects in the medial distal metaphysis of the femur. Benign cysts are a common occurrence in long bones, and are of concern in load-bearing bones, such as the tibia and femur. These space-occupying growths are removed by curettage of the affected region. Numerous post-curettage management options have been described in the literature, which generally include filling the defect with either synthetic or biological materials. Unfortunately, complications, such as infectious disease transmission, thermal injury, and a robust inflammatory have all been reported in the literature. In response to these concerns, a number of studies reported successful healing of benign cortical defects in long bones with no augmentation after curettage, however, the lack of structural support results in an increased risk of fracture through the defect site. Therefore, it is advantageous to investigate a treatment option that adds structural support to the defect site and permits the use of osteoconductive and osteoinductive materials within the bone cavity. The purpose of

this thesis was threefold: First, a quasi-static experimental comparison of intact and cortical defect specimens was conducted to determine the structural consequences incurred by the introduction of a 15 mm cortical defect under isolated axial and torsional loads. Second, an experimental combined axial/torsional fatigue analysis was employed to further analyze the behavior of the defect specimens, and to determine the structural stiffness regained by the addition of a one-third tubular plate. Third, a numerical approach was used to consider the structural consequences of varying sized defects under isolated and combined quasi-static axial and torsional loading, and to further analyze the results of adding the plate to the defect specimens. This study revealed that a one-third tubular plate might be a clinically viable option for structural support of small cortical defects in the distal femur. Furthermore, the loss in stiffness by the defect is exacerbated under combined axial/torsional loading. This is a more physiologically relevant loading mode and may provide more clinically useful results.

Contents

List of Figures

List of Tables

Chapter 1

Introduction

1.1 Introduction

Benign bone cysts are non-cancerous growths that form within bone. They are most common in young patients under the age of 30, and commonly occur in the femur, tibia, humerus, and pelvis. These growths occur in a number of forms, including tumors and non-neoplastic (i.e., not a tumor) bone simulating conditions. While these benign cysts are not direct evidence of cancer, they can pose risk to the patient. Large cysts in weight-bearing regions are at high risk of fracture and may be removed prophylactically to mitigate the risk of injury to the patient. Some benign tumors, in particular giant cell tumors, are highly aggresive and while they are non-cancerous, they can cause significant pain and damage to the surrounding bone. [1, 2] The preliminary step in treating these growths involves monitoring the size and growth rate of the tumor prior to surgical intervention. If the tumor is large, it may compromise structural integrity, especially in weight-bearing bones. If growth persists, the physician proceeds to surgical treatment with the goal of removing the tumor and restoring the structural integrity of the bone. Generally, the

growth is surgically removed by curettage, or physical scraping, of the affected region of the bone. Consequently, once the space-occupying growth has been removed, a large hole, or defect, remains at the site. A number of post-curettage management options have been described in the literature. Previous studies reported successful healing of the defect with no augmentation after curettage, while others reported success after filling of the defect with biological and synthetic materials, such as autogenous bone graft, allogenic bone graft, poly(methyl-methacrylate) bone cement, and artificial bone substitutes. High success rates have been reported for many of these methods, however, most restrict the patient to no weight-bearing immediately post-operatively. Bone responds positively to mechanical loading, therefore faster time to weight-bearing may result in proportionally faster healing rates.

This study investigates the use of a 1/3 tubular plate for structural reinforcement of cortical defects after curettage. The 1/3 tubular plate is a small, non-locking stainless steel plate that has the form of 1/3 of the circumference of a cylinder. They are 1 mm thick, 9 mm wide, and range from 2 to 12 holes (25–145 mm, respectively) in length. Due to their small size, they have a lower strength than large plates, such as locking compression plates, and are easily contoured to the surface of the bone. This plate is proposed as a way to provide structural reinforcement to the defect, sufficient for immediate weight-bearing, while still permitting the use of bone graft as a filler to promote adequate healing. This combined treatment method may result in better healing outcomes with lower rates of post-operative fracture through the defect than current treatment methods.

1.2 Problem Statement

The goal of this thesis was to assess the proposed treatment method. Our intent was to assess the structural viability using an integrated experimental and compu-

tational approach. In the first phase of experimental work, synthetic femurs were used to compare intact specimens with no defect against specimens with a small post-curettage cortical defect on the medial, distal metaphysis. Initial experiments revealed the structural effect of the defect under quasi-static loading (isolated axial and torsional loading) and a torsional load-to-failure. The second phase of experimental work utilized two groups of synthetic femurs: the first group was subjected to the same defect with no structural reinforcement, and the second group was subjected to the defect, then augmented with a 3-hole 1/3 tubular plate. The two groups were assessed under combined axial and torsional cyclic loading.

A computational model, using the finite element method, was developed in parallel with the experimental work. The results of the experiments were used to develop validated finite element models of the femur with no defect. The femur with a defect and no treatment, and the femur with a defect and treatment were then modeled to visualize localized stresses and strains. Furthermore, the validated models were used to make predictions by varying parameters within the model. The final results of the experimental and numerical methods were used to understand the viability of the proposed treatment method.

This study was presented with numerous research challenges in both the experimental and numerical work. Quasi-static isolated stiffness testing and isolated load to failure analyses (i.e., pure compression, pure torsion, or pure bending) are often used to consider the structural effects of orthopaedic implant and bone constructs. This study employed isolated quasi-static stiffness testing, isolated load to failure analyses, and combined axial-torsional cyclic loading in a full bone model. The combined axial-torsional loading needed to accurately represent the physiological loads imposed on the femur during everyday activity. This included off-axis loading of the femur through the mechanical axis, loading the femoral head in a way the models the hip, and capturing the rigid characteristics of the knee. Next, the removal of

the intramedullary cyst was challenging to simulate in a way that was accurate and repeatable. Both cortical and cancellous bone needed to be removed in ways that represented the cortical window and cancellous bone removed by curettage of the defect site. Because only a small defect was introduced, it became challenging to elucidate clear differences between groups, thus requiring rigorous testing and analysis. Finally, the numerical analysis was conducted using the finite element method on a full bone model that identically replicated the experimental loading conditions, including the simulated hip and knee joints. The use of a full bone model introduced highly nonlinear geometry and body-to-body contacts that significantly increased the model complexity. Thus, a highly complex and sophisticated numerical model was required to accurately replicate the experimental conditions.

The results of this study contribute to the orthopaedic community by evaluating the viability of a novel augmentation method for small cortical defects in the distal femur. Similarly, the experimental and numerical analyses contribute to orthopaedic surgeons and researchers by further elucidating the effects of varying sized defects. Previous studies have evaluated the effects of defects in isolated experimental loading conditions, such as bending and torsion. Similarly, previous studies have evaluated these defects under isolated loads in simplified finite element models, such as representation of the diaphysis as a simple cylinder. This study was the first to evaluate the effects of cortical defects under combined axial and torsional loads. This loading configuration replicates physiologically relevant loads (combined compression, tension, and torsion) that are imposed on the femur during normal gait. Few studies use full bone models to evaluate the viability of orthopaedic constructs. This study reveals that combined loading yields different results that isolated conditions. This may motivate future research studies to employ such conditions when evaluating orthopaedic constructs. The results of this study have implications among orthopaedic clinicians and researchers.

1.3 Structure of Thesis

This thesis is structured into four main chapters: Chapter 2 describes the anatomy of the femur, benign tumors, a review of research on cortical defects in bone, a review of current methods for treatment of benign growths, a background of the finite element method, and applications of the finite element method in orthopaedics. Chapter 3 outlines the experimental methods and results, and concludes with a discussion of the experimental results. Chapter 4 describes the methods, results, and discussion of the finite element simulations. Finally, the thesis is concluded in Chapter 5 with a final discussion, remarks on the study limitations, and suggestions for areas of future research.

Chapter 2

Literature Review

2.1 The Femur

The femur, shown in Figure 2.1, is the bone of the thigh and is the longest and strongest bone in the body. [3,4] The femur is an exceptional structure for its ability to withstand large dynamic and static forces over sustained periods of time. It possesses a long shaft, and articulates with the hipbone at the proximal end and with the knee at the distal end. The femur is separated into three distinct regions: the proximal region, including the greater and lesser trochanters, the neck, and the head; the diaphysis, or the shaft; and the distal region, including the metaphysis (region connecting shaft and epicondyles), and condyles, or articulating surfaces, of the knee. [3,4] These anatomical landmarks are illustrated in Figure 2.2.

The structure of the femur is unique in that its mechanical and anatomical axes are not co-linear. As can be seen in Figure 2.1, the proximal region of the femur (hip) is more lateral to the anterior-posterior (sagittal) plane of the body than the distal end (knee). The mechanical axis, shown in Figure 2.3, is the line that connects the femoral head to the intercondylar notch, and is the axis of weight bearing through

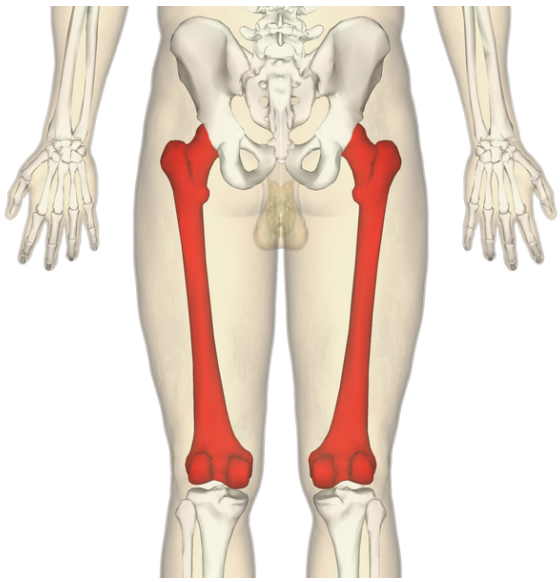

Figure 2.1: Image showing femur from posterior view of thigh region. The femur is highlighted in red. Image adapted from BodyParts3D. [5]

the femur. This leads to off axis, eccentric loading that imposes a large bending mode about the fixed point of the knee. The bending load creates a combination of compressive forces along the medial surface and tensile forces along the lateral surface. Additionally, the femoral head is loaded under internal and external torsion during walking and running.

There is large variation in femur anatomy and alignment between individuals that leads to slight differences in loading mechanics. A study was conducted in 1987 by Yoshioka et al. [6] that investigated the general anatomy and functional axes of 32 cadaver femurs. Within the specimens they observed an average length of 46.6 cm ($\pm$ 22.8 cm) among males and 44.2 cm ($\pm$ 27.7 cm) in females. A neck-shaft angle (the angle between the axis through the neck and the axis through the shaft) of 129° ($\pm$ 7.3°) was observed in males and 133° ($\pm$ 6.6°) was observed in females. A tibio-femoral angle (angle between femur's anatomical axis and mechanical axis, shown in Figure 2.3) of 5° was observed for both males and females ($\pm$ 0.9°; $\pm$ 1.1°,

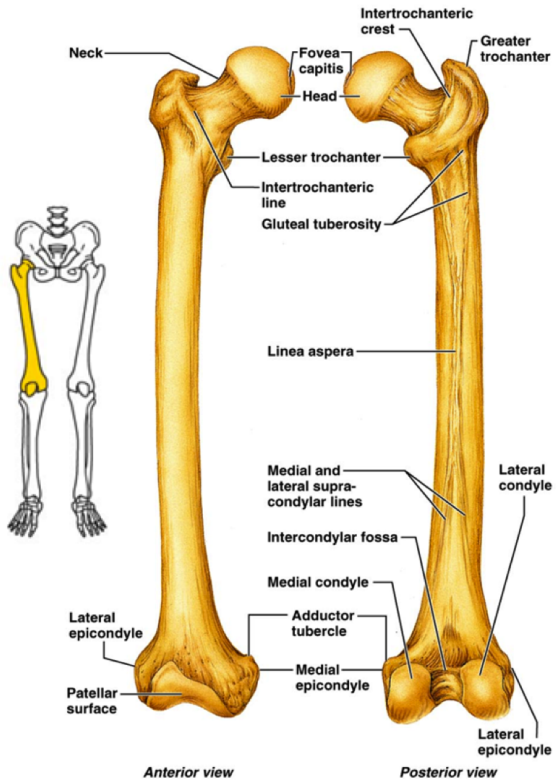

Figure 2.2: Image showing the anatomical landmarks of the femur. Image adapted from Pearson Education, Inc.

respectively). Finally, they measured the degree of anteversion, or forward twist of the femoral neck from the medial-lateral (coronal) plane. A forward twist of the neck of 7° (± 6.8°) was observed in males and 8° (± 8°) was observed in females, which corresponds to an overall average of 13.1° of anteversion using traditional measurement techniques[1]. These anatomical parameters, specifically tibio-femoral angle and anteversion, are closely replicated in the experimental configuration described in Section 3.3.

[1]Previous researchers have measured anteversion using a slightly different method that results in a greater degree of measured anteversion. In the methods section, anteversion is a parameter that is considered for mechanical loading of the femur. The second method that results in a larger measurement is the method used for the experimental configuration

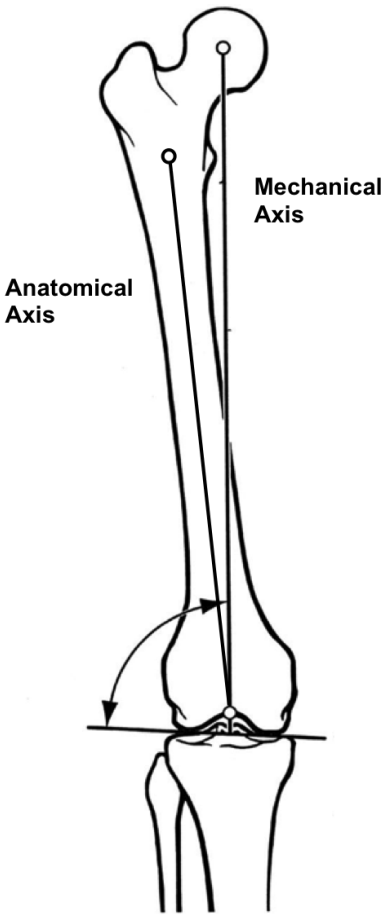

Figure 2.3: Image showing the mechanical axis of the femur. Image adapted from Gugenheim et al. [7]

2.2 Benign Bone Tumors

Tumors are masses of tissue that form due to unregulated cell growth and proliferation, and can be classified as malignant (cancerous) or benign. [1, 8] Cancer is a group of diseases that is characterized by six distinctive characteristics, often called the "Six Hallmarks of Cancer": Cancer cells: 1) possess growth signal autonomy, or rapid cell growth independent of external proliferation signals; 2) elude growth inhibition from external inhibitory signals; 3) resist apoptosis, or normal programmed cell death, which regulates the number of cells in a tissue; 4) have unlimited cell

replication potential; 5) can form vascularized tumors through angiogenesis, meaning cancerous masses form new blood vessels to maintain cell viability throughout the tumor; and 6) metastasize, or invade, other regions of the body, altering normal cell function, which generally leads ultimately to death. [8, 9] Although benign tumors possess many of these characteristics, they are not direct evidence of cancer, due primarily to their inability to metastasize.

Primary bone tumors (cancer originating in the bone) are very rare, with an incidence of less than 0.2% of all cancer cases in the United States in 2014. The American Cancer Society estimates 3,020 primary bone cancer cases resulting in 1,460 deaths in 2014, based on cancer statistics from 1995-2010. [10] Cancerous lesions in bone can commonly arise as secondary tumors from primary metastatic cancer originating in other regions of the body, including the breasts, lungs, and prostate. [11] The majority of primary bone tumors are benign and generally asymptomatic, and are usually only detected by radiographic examination of the region. [12] Therefore, a precise incidence rate of benign bone tumors is difficult to determine. Benign bone tumors are commonly observed as small defects originating in the medullary canal, and often do not breach the cortex. On the contrary, malignant bone tumors are often associated with significant cortical damage. Benign bone growths also commonly occur as bone-simulating non-neoplastic conditions that appear, upon initial radiographic evaluation, as primary bone malignancies.

A number of factors play an important role in the pathologist's diagnosis of bone tumors, including cytologic evaluation, tumor architecture, and the type of matrix produced by the tumor. Generally, age, location, and size offer preliminary insight to the pathologic state of the tumor. The common age and anatomical site distributions of many common benign bone tumors and non-neoplastic bone simulating conditions are summarized in Tables 2.1 and 2.2, respectively. Although insightful, an adequate diagnosis is not complete without the results of a thorough tissue examination.

Table 2.1: Common benign bone tumor classifications with age and body location. Adapted from Davies et al. [12] and the World Health Organization [13].

Histologic Type	**Peak Age**	**Common Location**
Cartilage Tumors		
Osteochondroma	10–30	Distal femur, proximal tibia, proximal humerus, rarely in flat bones
Enchondroma	10–40	Hands,feet,long tubular bones
Periosteal chondroma	10–40	Proximal humerus, distal femur, hip region, pelvis
Chondroblastoma	10–30	Distal femur, proximal tibia, proximal humerus, calcaneus; typically epiphyseal
Chondromyxoid fibroma	10–30	Proximal tibia, distal femur, pelvis, metatarsals
Osteogenic Tumors		
Osteoid osteoma	5–25	Proximal femur, most long bones
Osteoblastoma	10–40	Spine, long tubular bones, jaws
Fibrogenic tumors		
Desmoplastic fibroma	10–30	Mandible, femur, pelvis; all very rare
Fibrohistiocytic tumors		
Benign fibrous histiocytoma	20–60	Pelvis, femur; usually diaphyseal or metaphyseal
Giant cell tumors		
Giant cell tumor	20-45	Distal femur, proximal tibia, distal radius, sacrum; often epiphyseal

Table 2.2: Table of conditions simulating primary benign bone tumors with age and body location. Adapted from Davies et al. [12]

Histologic Type	**Peak Age**	**Common Location**
Aneurysmal bone cyst	5–20	Femur, tibia, humerus, vertebrae
Simple bone cyst	Infancy–20	Proximal femur, humerus and tibia, calcaneus, ilium
Fibrous dysplasia	5–30	Long bones, jaws, skull, ribs
Non-ossifying fibroma	5–20	Distal femur, proximal and distal tibia
Osteofibrous dysplasia	Infancy–20	Tibia

2.3 Structrual Consequences of Cortical Defects in Long Bones

The structural consequences of cortical defect size and shape have long been debated by researchers and clinicians. Structural defects can impose consequences by affecting either the cancellous regions, cortical regions, or both, and can be introduced via natural or man-made methods. As described in Section 2.2, benign tumors are generally endosteal and do not penetrate the cortex. Therefore, we will focus on the existence of man-made defects such as screw holes and biopsy windows. We know from mechanics of materials that stress concentrations can take place at holes, slots, notches, threads, or any general changes in geometry or material properties. [14]

These stress risers result in increased localized stress that ultimately leads to yielding at the defect site. While the bulk of the component may remain elastic and the global stress is lower than the yield point, the introduction of the stress concentration will result in localized yielding and ultimately, catastrophic failure at the site. This concept is foundational in the analysis of bone defects as stress concentrations. A number of studies have sought to quantify critical defect size and risk of pathologic fracture of metastatic lesions in long bones. [15–17] Beals et al. [15] reviewed 338 patients with pathologic femoral fractures through lytic lesions. They concluded that defects greater than 2.5 cm should be prophylactically stabilized. Parrish and Murray [16] and Fidler [17] reviewed patients with impending fractures through metastatic lesions. Both studies recommended prophylactic fixation of defects encompassing 50% or more of the cross-sectional area of the cortex. Although these guidelines were setforth following review of metastatic bone defects, a number of *in vitro* studies have investigated these claims using biomechanical analyses of human and animal long bones. These studies were conducted in the absence of cancerous defects and therefore offer insightful results regarding periosteal and endosteal cortical defects.

Dr. Charles Bechtol first described the importance of engineering in orthopaedics in 1952. [18] In his iconic article, he noted the weakening effects of small drill holes, and made predictions regarding the size and shape of small stress concentrations in bone. Numerous *in vitro* studies investigated his predictions using human and animal bone. Brooks et al. demonstrated in canine femora that 2.8 mm and 3.6 mm drill holes are capable of reducing the energy-absorption capacity of a bone by up to 55%. [19] Clark et al. investigated the effect of biopsy-hole shape and size on bone strength in paired human cadaver femora. [20] Three window geometries were investigated: Group 1) a rectangular hole with square corners, Group 2) a rectangular hole with rounded corners, and Group 3) an oblong hole with rounded ends. The specimens were divided into two groups so that Group 1 was compared to Group 2 on paired specimens, and Group 2 was compared to Group 3 on paired

specimens. The femurs were loaded to failure in torsion at a rate of 50°/minute according to a protocol described by Burstein and Frankel. [21] All specimen failures resulted from a spiral fracture through the biopsy window. They found that the oblong hole (Group 3) was able to withstand 44% more torque and 83% more energy (taken as the area under the linear torque–displacement curve) than the rectangular hole with round corners (Group 2, $p < 0.01$). Bechtol predicted that a rectangular hole with rounded holes would resist failure more than a rectangular hole with square corners due to high stress concentrations at the corner points. [18] This, however, was disproved by Burstein, who reported that there is no statistical difference between the two groups. They continued their analysis by investigating the effect on torsional stiffness and energy absorption of varying hole length and width in the Group 3 geometry. They compared three groups of six specimens each[2] at a fixed length and varying width. Additionally, they considered three groups of six specimens each with defects of varying length and fixed width. Their results show that varying the width of the hole results in a statistically significant decrease in stiffness and energy absorption. They found no statistical reduction in either stiffness or energy absorption due to lengthening the cortical window. Clark et al. [20] completed their analysis by demonstrating that approximately 4% more material is removed for a window with parallel cuts versus an oblong hole with rounded ends. Interestingly, this resulted in a corresponding 4% decrease in torsional stiffness and a 4% increase in calculated stress. In order to remove an adequate biopsy sample, a large enough piece of cortex must be removed. They conclude that although the rectuangular windows permit greater access to the medullary canal, the reduction in stiffness results in a great structural disadvantage; therefore, an oblong window with rounded edges, a narrow width, and necessary length, should be used to remove a large enough sample for biopsy.

[2]One specimen in one of the groups was discarded due to the incidence of a hairline fracture during creation of the defect.

McBroom and Hayes [22] tested small bony defects using four-point bending and observed a reduction in strength of 70% for defects involving 30% of the cortex. They also observed that bone strength decreases linearly as the hole size increases linearly. [22] It was predicted that prophylactic intervention was only required for defects involving destruction or removal of greater than 50% of the cortex. This prediction, however, was not tested until years later. Edgerton et al. tested similar defects in torsion and found a 72% decrease in strength for circumferential defects involving 20% of the cortex. They also concluded that the ratio of defect diameter to bone diameter was an accurate predictor of the weakening effects of cortical defects and could be used for quantifying critical sizes in future studies. [23] Following these studies, Leggon et al. sought to quantify the strength reduction and effects of diaphyseal defects on long bones involving 50% of the anterior cortex. [24] Although a 50% defect was hypothesized to be of critical size for prophylactic intervention, no study had yet quantified the strength reduction incurred by a defect of this size. They utilized paired canine femora to consider six total groups including intact bones, bones with 50% cortical defects (oblong in shape, 1.9 cm in length, cut back until one half of the cross-sectional area was removed), and 50% cortical defects treated with a variety of treatment options. They observed a reduction in bone strength of 87.3% as a consequence of the defect. Similarly, McBroom et al. [25] investigated the flexural strength reductions imposed by eight varying sized drill holes in the diaphysis of paired canine femora. They varied the defects such that the ratio of drill hole to bone diameter (a/D) ranged from 0.1 to 0.8. They observed a progressive reduction in strength as the ratio of a/D increased. The 0.1 a/D defect resulted in 80% of the intact bone strength, whereas the 0.8 a/D defects retained only 30% of the flexural strength. The decrease in strength was observed to be linear, except for the line between 0.1 and 0.2, which displayed a much more drastic reduction in stiffness than the other ratios. The authors compared their results to predictions us-

ing beam theory and finite element analyses[3]. They observed that the beam theory and non-linear finite element predictions correlated well with the *in vitro* results as well as previously published data on stress concentration factors for circular holes in a cylindrical tube. These results are further described in Section 2.6. Similarly, Edgerton et al. [26] investigated posterior uni-cortical femoral defects ranging from 10–60% of the mediolateral bone diameter. The 60% defect was equal to the diameter of the medullary canal, and thus no damage was done to the adjacent cortices (medial and lateral). The specimens were loaded to failure in internal rotation at a rapid rate of 30°/second. Their results show that there is a steady decrease from 100% of the ultimate torque to only 30% of the ultimate torque for a 60% defect. They observed the same trend as McBroom et al. [25], where the slope between the 10% and 20% cortical defects (m = -3.5) was approximately four times greater than the decrease from 20–60% (m = -0.85). An energy loss of 60% was observed from increasing the defect size from 10% to 20%. Interestingly, for a 10% defect, they observed no difference in ultimate torque and an increase in ultimate rotation and ultimate energy when compared to the intact contralateral specimens. Their results for ultimate torque, rotation, and energy are shown in Figure 2.4.

Endosteal defects that do not completely penetrate the cortical wall can still pose a particular risk to the structural integrity of the bone. Hipp et al. investigated the flexural strength reduction due to partial-thickness endosteal defects of varying diameter in matched canine femora. [27] The defects were introduced into the diaphysis of one of the matched specimens. The defect was 11 mm in length and uniformly thinned along the endosteal surface, with the exception of the center, where a larger spherical volume was removed. The contralateral specimen remained intact and the results were utilized for comparison to a negative control. Their results demonstrated

[3]The finite element method is a numerical approach to solving complex analytical mechanics problems. The finite element method and its applicability in orthopaedics is described in greater detail in Section 2.6

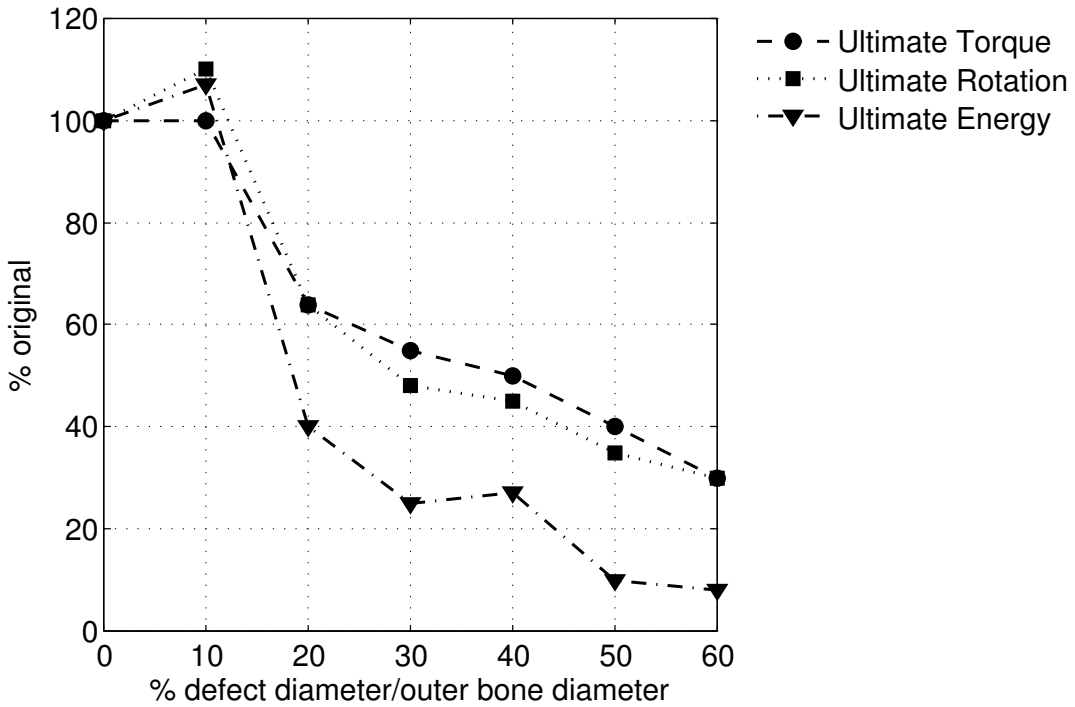

Figure 2.4: Percent original ultimate torque, rotation, and energy for varying sized defects. Data adapted from Edgerton et al. [26]. The error bars shown on the original plots were not included in this adaptation.

a linear decrease in bone strength in both modes of loading as the size of the defect increases (i.e., the cortical wall becomes thinner). They observed strength reductions up to 78% in the presence of a larger endosteal defect. Their results correlated well with predictions from beam theory and a finite element analysis, which were then utilized to consider the effects of eccentrically positioned defects (described in further detail in Section 2.6). For a centrally located defect tested experimentally, a reduction in cross-sectional area of 50% resulted in a 60% loss in strength. In the case of an eccentrically positioned defect, a defect size of 20–60% intact cortex will have the same flexural strength as a centrally placed defect with only 20% remaining cortex. This finding is particularly interesting for consideration in the clinic where proper multi-plane imaging must be used to properly diagnose the location and size of the

defect. If, for example, the defect is assumed to be centrally placed, but is instead eccentrically located such that one cortex is much thinner than the other, the patient may be at high risk for fracture due to underestimated weakening. The authors performed an evaluation of the worst case error (R_e) for a range of measurement errors (M_e) using a 4 mm cortical wall thickness. The error (R_e) was determined as

$$R_e = \frac{D - M_e}{C - M_e} \tag{2.1}$$

where M_e is the measurement error, D is the minimum intact wall thickness and C is the actual wall thickness. This model was used to calculate the worst case error for a range of measurement errors of remaining cortical wall. The results of the their predictions are shown in Figure 2.5. In a study of cortex thickness in human cadaveric femurs, Smith et al. [28] reported measurement discrepancies of 0.18–0.6 mm in radiographic measurements. As shown in Figure 2.5, measurement errors of 0.6 mm results in incorrect estimations off by up to 25%. Thus, it is important to accurately quantify the size of both periosteal and endosteal defects. The previous studies have reported the structural impact of periosteal and endosteal defects in human and animal bone. Prior to intervention, it is important to understand the consequences of cortical defects in order to implement the optimal treatment in the operating room. These studies demonstrate that even small cortical defects negatively affect the structural integrity of bone in axial compression, bending, and torsion, which are all physiological relevant loads imposed on the distal femur. Similarly, we see that endosteal defects can have catastrophic outcomes if not properly characterized. Thus, proper intervention must be investigated to determine methods of treatment that will result in the greatest patient outcomes.

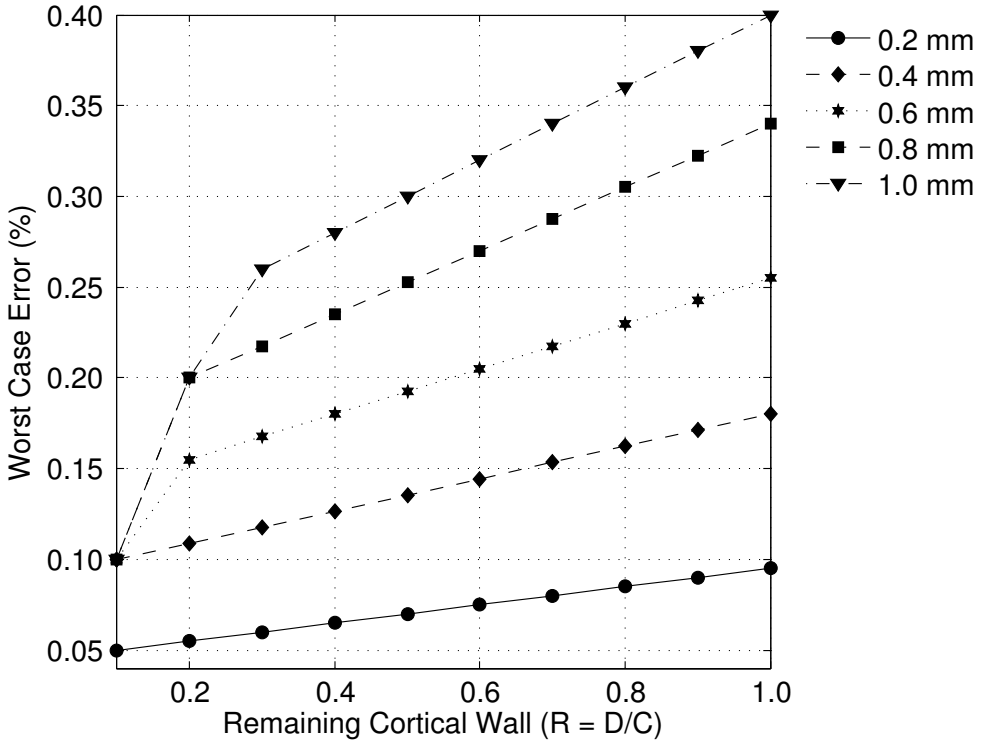

Figure 2.5: Worst case error versus remaining cortical wall for a range of measurement errors. Adapted from Hipp et al. [27]

2.4 Current Methods for Treatment of Benign Lesions in Long Bones

The objective of treatment of benign lesions in bone is to remove the tumor and restore the structural integrity of the bone. This is especially of concern in load-bearing bones, such as the tibia and femur. Benign lesions that are free of pain and in non-load-bearing regions generally do not require intervention and are often left alone. In load bearing regions, however, prophylactic intervention is often recommended and even required. Benign bone tumors are often removed by intralesional curretage, which results in the creation of a bone defect. Large defects and cavities are often reinforced with fillers and bones substitutes, such as autologous

bone grafts [29, 30], allografts [31–34], poly (methyl-methacrylate) (PMMA) bone cement [35–37], and other bone substitutes [30, 38]. Each of these methods have their respective advantages and limitation.

Autogenous bone graft is one of the most effective methods for promoting healing and restoration of bone defects due to their osteoconductive (graft material serves as scaffold for new bone ingrowth) and osteoinductive (graft stimulates osteoprogenitor cells to differentiate into osteoblasts) properties. [30] This graft material is available either as vascularized or nonvascularized cortical bone or as bone marrow grafts. Cancellous bone graft is highly vascularized and very easily incorporated into the defect, however, due to loose packing and low stiffness, it is only effective as a space filler that provides very little structural support. This makes it most effective as a supplementary filler, or as a graft for endosteal defects with little to no cortical bone damage. Once incorporated, however, it is capable of ultimately achieving strength equal to cortical graft after approximately 6–12 months. [30] Cortical bone graft is most often harvested from the iliac crest but can also be taken from other bones such as the fibula or ribs. Cortical bone graft is mostly osteoconductive and provides excellent structural support within the defect, but has very low osteoinductive properties. Interestingly, cortical bone grafts lose their initial structural strength and often must be supported with additional fixation to maintain proper stability. Both cortical and cancellous bone grafts provide excellent outcomes with low rates of disease transmission. Unfortunately, there is limited supply of autologous bone graft and if an excess amount is removed, there is risk for donor site morbidity.

Allograft, or allogenic bone, is available in many forms, each with distinct biological properties. Demineralized bone matrix consists of crushed or pulverized bone and is osteoconductive and slightly osteoinductive. It vascularizes very rapidly and is a very suitable material for filling defects, however, it offers no structral support to the cavity. Other forms include cancellous and cortical allografts, which can be used

as supplementation or as an alternative to autograft, and even whole bone segments. Allograft materials can eliminate or alleviate the demand for autogenous bone graft, however, a small risk of infectious disease transmission has been reported. [30, 33]

PMMA bone cement is a common bone filler that is used to provide instant stability, and is especially useful in larger, more unstable defects. However, PMMA is not a bioactive material and may not be the most suitable biological method for filling defects. [35]. Another concern is that the setting of PMMA is an exothermic reaction, which releases a large amount of heat directly to the defect site. This may be advantageous by killing residual tumor cells within the cavity [35]; however, thermal injury near to the surface of the joint may damage surrounding chondrocytes [39], which has been associated with degenerative arthritis. [40, 41] A long-term follow-up study published in 2007 revealed that the cementation of giant cell tumors did not greatly increase the risk of osteoarthritis, although some relationship was observed. [42]

Materials such as hydroxyapatite and β-tricalcium phosphate are common bone substitutes used for filling defects. Theses materials are classified as polycryastilline ceramics and naturally occur in bone. Ceramics are naturally brittle in nature and possess poor tension properties, therefore they are best suited for uses such as filling and supporting compressive loads. These ceramics are osteoconductive materials that provide very little mechanical stability to the defect site. For best results, they should be packed densely within the defect with direct contact to the surrounding bone to maximize new bone ingrowth. [43] Hydroxyapatite has been reported for use in filling defects after curretage [44, 45], however some reports have shown that this material stimulates a robust inflammatory cytokine response. [46, 47] Similarly, Hirata et al. [48] reported successful filling of defects after curettage with β-tricalcium phosphate. Both hydroxyapatite and β-tricalcium phosphate require months of time for incorporation [45, 48], and neither provide much structural stability.

Recently, Hirn et al. [49] and Yanagawa et al. [50] investigated the outcomes of patients with defects in the lower extremity that were left unfilled after curettage. Among 51 patients, Yanagawa et al. [50] observed 3 post-operative fractures; one was deemed avoidable if perioperative weight bearing had been limited, while two occurred through local tumor reoccurrances. A total of 9 patients had local reoccurrance with 7 occurring from giant cell tumors. The volume of the tumors removed ranged from 3–31 cm^3. The patients were restricted to no weight or partial weight bearing for up to 3 months after the procedure. Hirn et al. [49] conducted curretage of benign tumors in the knee region (proximal tibia or distal femur) with no defect augmentation in 146 patients. The average tumor volume was 63 cm^3 (range: 1–240 cm^3) with 44% of the defects under 5 cm in diameter and the remaining 66% having a diameter of 5 cm or greater. 6 patients had preoperative fracture while 14 had postoperative fracture through the defect. They observed that there was significant difference ($P = 0.003$) in average size of defect sites that fractured versus those that did not (108 cm^3 and 60 cm^3, respectively). They concluded that the risk of fracture for defects with diameter less than 5 cm was 3% while the risk increased to 15% for defects greater than 5 cm in diameter. However, the average time to full weight bearing for defect with diameter less than 5 cm was 5.4 weeks while the average time for defects greater than 5 cm was 6.7 weeks. Overall, 9 patients were observed to have unsatisfactory outcomes resulting in a 94% success rate. Kreicbergs et al. [51] reviewed outcomes of patients with benign defects treated by curettage, with some treated by curettage alone and some with defect augmentation. They observed similar outcomes of 95% success in patients with curettage as the sole method of treatment.

The outcomes of patients after curretage vary greatly, including average time to weight-bearing, pre- and post-operative fracture risk, and tumor reoccurrance. Each method of defect augmentation (or lack thereof) after curretage possesses its' own advantageous and disadvantageous, however, it is clear that other methods of

treatment should be investigated to improve overall patient outcomes.

2.5 Synthetic Bones in Orthopaedic Research

2.5.1 Synthetic Versus Cadaveric

Synthetic bone models are becoming increasingly popular for use in orthpaedic research and education. Traditionally, human cadaver specimens have been utilized for these purposes. While cadaver specimens are still the quintessential model for both applications, researchers and educators acknowledge that there may be substantial benefits of using synthetic bone analogues. Human cadaver specimens possess three properties that are undesirable in both settings: 1) cadaver specimens are very expensive—nearly three times the cost of composite models [52], 2) there is high variability between specimens, and 3) they are challenging to store and handle. The demand for cadaver specimens is often met through the use of unclaimed deceased, often elderly or infermed persons, who become possessions of the state *post-mortum* [53, 54]. Consequently, these specimens may not be an accurate representation of the behavior of an orthopaedic construct for a young healthy person who presents with orthpaedic trauma. Due to limited inventory, it may be difficult to procure the required number of specimens for validation in a healthy bone model. A number of studies have sought to validate the use of composite specimens in orthopaedic research as means to minimize costs, control variability, and simplify handling.

2.5.2 1st Generation Composite Bones

The first biomechanically equivalent human bone analogues were introduced in the late 1980's by Pacific Reserach Laboratories, Inc. These models consisted of a rigid polyurethane foam cancellous region and a glass braided cylinder reinforced with epoxy for the cortex. It was quickly learned that these models were not an ideal representation of human bone due to delamination of the braided glass fibers and epoxy, however, some similarities were observed in later testing. [55] Szviek et al. [56] tested the material properties of a polyurethane foam similar to the rigid foam core of the 1st generation bone analogues. Their results were in the range (although on the low end) of Young modulus values reported in a previous study of human trabecular bone. [57] Although the material properties indicated by the manufacturer matched values for cortical bone, the issue of bonding the two materials was a greater concern and led to disapproving reports of use of the 1st generation model.

2.5.3 2nd Generation Composite Bones

The 2nd generation model, introduced in the early 1990's, contained a cortex constructed from e-glass fiber cloth, mat, and roving that was layered around a rigid or cellular polyurethane core. [58] The outer cortex was formed by pressure-injecting epoxy into the e-glass fabric, resulting in a glass-fabric-reinforced epoxy, thus promoting greater integration of the two materials. These models were created at the expense of no medullary canal and technical, labor-intensive construction. Despite the added manufacturing cost, the second generation model proved to be a more accurate representation of human bone. Szivek et al. [59] were the first to report the deformation response of the new analogues under single-leg loading. Their results revealed that the structural stiffnesses were in reasonable agreement with real bone stiffness values, and may be a valid model under a single leg loading stance.

Cristofolini et al. [60] measured the viscoelastic and strain response of 2nd generation composite, fresh frozen cadaver, and dried-rehydrated cadaveric femurs under axial loading, four-point bending, and torsion. They found no significant differences between the groups, and reported that the composite specimen properties fell in the range of the cadaveric groups. Additionally, they reported a decerease in variability among composite specimens 20-200 times lower than the cadaver groups. This result indicates that a smaller detectable difference can be observed when using synthetic bones. Cristofolini and Viceconti [61] conducted a similar study, investigating anatomical dimensions and the axial, torsional, and bending stiffness of synthetic and cadaveric tibias. They concluded that the synthetic models are most suitable for flexural and axial loading; however, torsional stiffness values exceeded those of normal human bone. Large inter-specimen variability as high as 99.9% was reported for the cadaveric group compared to 0.1% variability within the synthetic group. The authors comment that geometrical comparison resulted in satisfactory similarities, however, the endosteal surface is too narrow and results in a more "stove-pipe" geometry than actual human tibias. Shortly after, a new design of the 2nd generation model was introduced that utilized a short-glass fiber-reinforced (SGFR) epoxy rather than the GFR epoxy for the cortical region. It was hypothesized that this would offer an improvement in material uniformity, simplify manufacturing, and permit greater anatomic detail. Heiner and Brown [62] investigated the axial, bending, and torsional response of the SGFR model compared to the GFR model. They found that SGFR models were significantly less stiff than the FFR specimens and additionally, resulted in lower variability than the FFR group under axial loading.

2.5.4 3rd Generation Composite Bones

The results of the previous study led to the innovation of the 3rd generation model, which utilized a SGFR epoxy that is pressure injected around the polyurethane

core [63]. The molds for the pressure injection were cast directly from bones of an adult male cadaver. This improved overall anatomical precision including gross size, cortical wall thickness, topographical features, and inclusion of a medullary canal. The anisotropy of cortical wall thickness was simulated by serial sectioning of the specimens, which was then utilized to build appropriate heterogeneity into the model. Heiner and Brown [62] reported stiffness values in the range of human bone, including the response torsional loading which was previously reported to be significantly higher [61], which demonstrates an improvement in material properties from the FFR epoxy to the SGFR epoxy.

2.5.5 4th Generation Composite Bones

The current 4th generation composite bone model employs the same fabrication, utilizing injection-molded SGFR epoxy around a polyurethane core, with only alterations to the epoxy resin component. The primary changes of the cortical layer are primarily for enhancement of the fracture toughness, fatigue life, tensile and compressive strength and modulus, thermal stability, fatigue crack resistance, implant subsidence, and moisture resistance. [64] Select material properties of the 4th generation composite femurs and human cadaver femurs are shown in Table 2.3. Chong et al. [65] investigated the fracture toughness and fatigue crack propagation rate of the 4th generation cortical material in comparison to the 3rd generation. They evaluated ultimate tensile strength and elastic modulus (E) using injection-molded dog-bone specimens (ASTM D63803[4]). Subsequently, the authors investigated the fracture toughness (K_{IC}) and fatigue crack resistance using compact tension specimens

[4]American Society for Testing and Materials (ASTM) is an international organization that establishes technical standards in one of six categories: 1) specification, 2) test methods, 3) practice, 4) guide, 5) classification, and 6) terminology. Over 12,000 ASTM published standards are currently referenced within the technical community. [66]

Table 2.3: Table of 4th generation composite and human cadaveric femur material properties. The value in parenthesis represents the coefficient of variation (= standard deviation ÷ mean). Flexural rigidity AT = anterior cortex in tension; Flexural rigidity LT = lateral cortex in tension; UTS = ultimate tensile strength; $E_{Tensile}$ = Young's modulus in tension;"L" and "T" represent longitudinal and transverse, respectively. †Only a range of values was provided; coefficient of variation not calculated.

Property		4^{th} Generation	Study	Cadaver	Study
Axial stiffness	(N/mm)	1860 (7.5%) 1230 (16.3%)	[67] [68]	1387 (14.6%) 2480 (25.0%)	[60] [67]
Torsional stiffness	($N{\cdot}m^2$/deg)	3.21 (2.6%) 4.14 (5.3%)	[67] [68]	4.41 (37.0%) 3.35 (32.2%)	[67] [57]
Flexural Rigidity AT	($N{\cdot}m^2$)	241 (4.5%) 252 (3.6%)	[67] [68]	317 (23.0%) 369 (42.7%)	[67] [60]
Flexural Rigidity LT	($N{\cdot}m^2$)	273 (5.8%) 305 (5.6%)	[67] [68]	290 (42%) 277 (29.2%)	[67] [60]
UTS	(MPa)	107 (5.4%)	[65]	L: 132.0 (12.2%) T: 57.9 (9.5%)	[69]
$E_{Tensile}$	(GPa)	15.8 (1.3%)	[65]	L: 17.7 (22.0%) T: 13.1 (23.6%)	[69]
Fracture Toughness	($MPa{\cdot}m^{1/2}$)	4.07 (7.6%)	[65]	1.6–8.3†	[70]

under plane strain conditions.[5] Their results revealed an increase of approximately 40% for the ultimate tensile strength and modulus of elasticity and nearly 50% in fracture toughness from the 3rd to the 4th generation composite bones. Their values fall within the ranges of previously published data on fresh frozen cadaveric bones, matching more closely than 3rd generation material properties. [69–71]

Subsequently, Chong et al. [72] compared the *in vitro* fatigue performance of 3rd and 4th generation femurs implanted with a cemented total hip arthroplasty (THA) construct. The experiments were carried out under *in vivo* conditions, including submersion in a physiological-temperature water bath in a cyclic, single-leg stance loading configuration. The 3rd generation constructs averaged failure at 3.16 $\pm$ 1.54 million cycles, whereas all 4th generation constructs survived beyone the cease of the experiments at 10 million cycles. Heiner followed these studies by reporting the axial stiffness, torsional rigidity, and flexural rigidity (anterior-posterior and lateral-medial loading). [67] These values were reported to align more closely with previously reported values for cadaveric specimens than the 3rd generation composite bones. [62] The 4th generation models are available with solid rigid and cellular polyurethane foam cores. Zdero et al. [73] compared screw pullout force, shear stress, and energy-to-pullout in the cancellous regions of 4th generation composite and cadaveric human bones. Their results revealed no statistical difference between any of the groups, concluding that the cancellous material in either composite model is an appropriate substitute for human bone. Similarly, Zdero et al. investigated cortical screw purchase in the distal, diaphyseal, and proximal regions of 3rd generation femurs (16 mm diameter canal), 4th generation femurs (16mm and 20mm diameter

[5]In mechanics of materials, plane stress and strain are defined as states in which the shear and normal vectors are assumed to be zero, respectively. In thick bodies, we argue that at a point, a large force must be exerted to move material in the thickness direction; therefore, the strains are expected to be very small in the thickness direction and thus small enough to be neglected. The assumption of plane strain is a method of simplifying the mathematical analysis.

canals), and human bone. They observed no statistical difference between any of the groups, although the 4th generation models with the 20 mm diameter medullary canals more closely represented human cortical bone. The results of these studies demonstrate that the 4th generation composite femurs have material properties corresponding more closely to natural human bone than previous models. Generally, these properties lie at the high end of the ranges for natural human bone; therefore, the 4th generation may be best suited to studies involving healthy human bone. Numerous studies in the literature have utilized these composite bones for comparison of fracture management and fixation constructs. There is evidence that the reduced variability between groups and the high level of material and geometrical consistencies of the composite bones may provide a reliable and informative platform for orthopaedic biomechanics research, especially for a comparison of means between similar groups. [52]

2.6 Finite Element Modeling in Orthopaedics

2.6.1 The Finite Element Method

The finite element method (FEM) is a numerical tool used for developing solutions to complex, analytical engineering and physics mathematics problems. [74] FEM has been used in a wide range of applications, including structural analysis, thermodynamics (fluid flow, heat transfer, mass transfer), and electromagnetics. The FEM provides a method to develop approximations for challenging analyses involving complicated geometries, load conditions, material properties, etc. in which an analytical solution is not obtainable.

In 1989, Hipp et al. [27] used experimental and finite element methods to evaluate the effects of endosteal defects under bending and torsional loads. The experimen-

tal methods and results of this study are described in Section 2.3. The four-point bending setup was modeled exactly like the model developed by McBroom et al. [25]. Because torsional loading is not exclusively uniaxial loading, one-half of a cylinder was required to observe all the stresses. A number of endosteal defects were investigated using the FEA: 1) four endosteal defects of varying size, 2) one elongated defect, and 3) one defect modeled eccentrically within the canal. Figure 2.6 shows an illustration of the diaphyseal model with endosteal defect. These were investigated using both linear, orthotropic cortical bone properties and nonlinear, isotropic, elastic-plastic properties. The endosteal defects were modeled with varying cortical wall thickness ratios (minimum cortical wall thickness at defect/intact wall thickness outside of defect) of 0.2, 0.4, 0.6, and 0.8. In order to simulate weakened regions of cortical bone within the defect, the material properties along the endosteal wall were represented by isotropic elements with reduced elastic modulus. This region is illustrated in Figure 2.6 as the shaded elements within the defect. The results of this

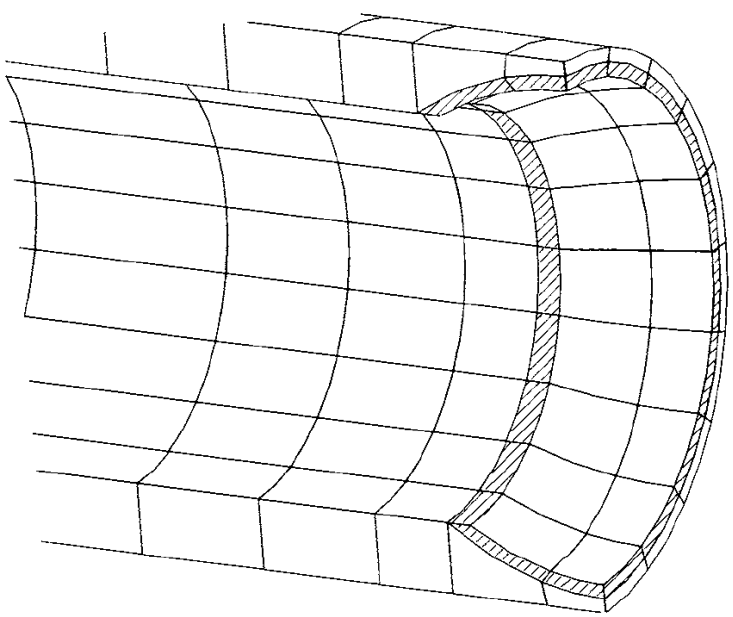

Figure 2.6: Endosteal defect in the cylindrical femur diaphysis model. Figure adapted from Hipp et al. [27]

analysis revealed that both the nonlinear and linear FEA correlated well with the experimental data. These results are similar to McBroom et al. [25], showing that the linear FEA underestimated the intact strength, while the beam theory predictions overestimated slightly. The nonlinear FEA showed the greatest agreement with the experimental results. Figure 2.7 shows the results of four-point bending experiments and the three prediction methods.

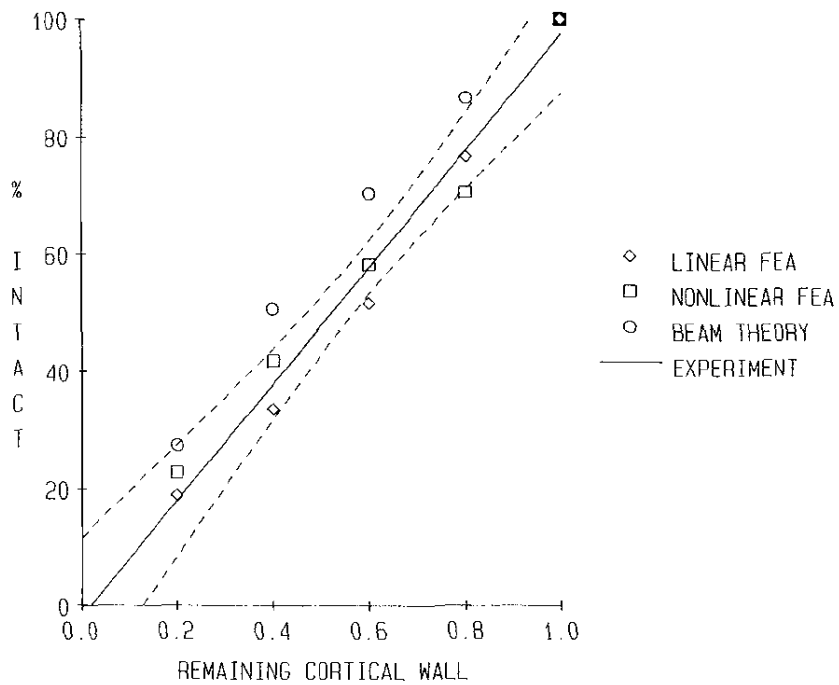

Figure 2.7: Intact strength results for four-point testing of endosteal defects and predictions from FEA and beam theory. The black line represents the experimental data and the dashed lines are the 95% confidence interval. Figure adapted from Hipp et al. [27]

It was observed that the loss in strength linearly decreases as a function of the degradation of the material properties in the cortical wall. [27] An interesting observation from their four-point bending results revealed that asymmetric defects have structural consequences comparable to much larger, centrally located defects. Once validated, the model was expanded to consider torsional stresses on the bone; no

experimental data were collected under torsional loads. The FEA results revealed that the highest stresses occurred at the thinnest region of the cortex when exposed to torsional loads. The same trend showing that asymmetric defects have larger consequences than centrally placed defects of the same size was observed in the torsional analysis. Their predictions of the consequences of incorrect measurements are shown in Figure 2.5 in Section 2.3. Because no experimental data were used to validate their results, future work was required to evaluate the validity of the model under torsional loads.

In 1990, Hipp, Edgerton, and Hayes [75] used a FEA to investigate the structural consequences of transcortical holes on long bones loaded in torsion. This study utilized the experimental results of loading sheep femora with transcortical drill holes to failure in torsion. [23] The authors considered both a linear elastic, orthotropic model and a non-linear, isotropic, elastic-plastic material model. They evaluated the torsional consequences due to: 1) varying drill hole sizes, 2) varying wall thickness at fixed drill hole diameters, 3) asymmetric wall thicknesses, 4) curvature along the long axis of the bone, and 5) oblong defect holes with varying defect length. Reasonable agreement was observed between the predictions and the experimental data. Both the linear FEA and the beam theory predictions overestimated the loss in strength, while the non-linear FEA underestimated the loss in torsional strength. Figure 2.8 shows the results of the experimental data and the FE and beam theory predictions.

A number of clinically relevant conclusions were drawn from the results. Fidler et al. [17] had suggested prophylactic intervention for defects encompassing 50% of the cross-section. This study revealed that transcortical holes encompassing 40% of the cross-sectional area reduced the torsional strength by 70%. Second, as many authors have concluded, these results will vary significantly for weaker bones with thinner cortices, such as osteoporotic bone. Third, defect geometry plays a large role

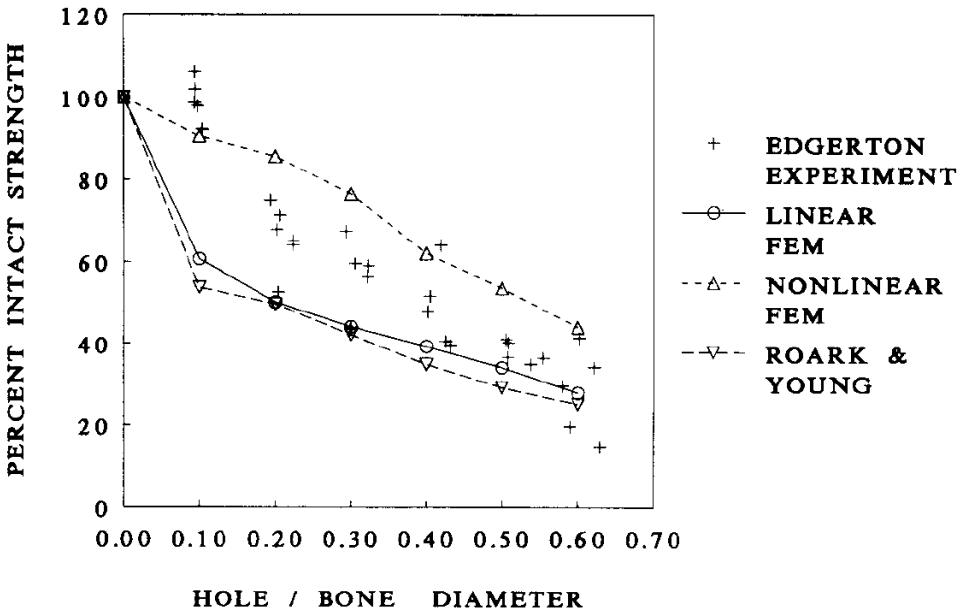

Figure 2.8: Plot showing the % intact strength results for torsional testing of transcortical drill holes and predictions from FEA and beam theory. Figure adapted from Hipp et al. [75]. The experimental data were adapted from Edgerton et al. [23]

in strength reduction, and therefore the results of this study were not conclusive for other geometries. Some differences were observed between the analytical results and the experimental data from Edgerton et al. [23] The authors considered a number of study weaknesses that may have affected the results, including modeling technique and assumptions. For example, only one element was utilized through the thickness of the cortical wall. Greater mesh refinement may have reduced the predicted values of strength reduction, bringing the analytical results in closer agreement with the experimental data. Additionally, they recognized the weakness in single cycle, single load boundary conditions. The results will likely vary since the femur is loaded in combined axial compression, bending, and torsion.

Finite element modeling has been significantly improved by the increased accuracy in bone material properties through quantitative computed tomography (QCT).

The models allow for specimen specific models that accurately model geometry and bone density. QCT differs from routine CT by the inclusion of a calibration phantom, which provides known reference material property data. QCT data has been used to improve beam theory predictions and finite element models by permitting individual stiffness assignment at each element. Keyak and colleagues presented the integration of QCT data and FE models for improved predictions in a number of papers. [76–79] In 2005, Keyak et al. [80] presented predictions of strength of femoral shafts with and without femoral lesions using QCT and FEA. Unlike many of the *in vitro* studies, the researchers obtained cadaveric femoral shafts from donors with history of malignant cancers (breast, prostate, and lung). The diaphysis was isolated from the femur and the section was imaged using QCT. The shafts were imaged to observe the presence of visible metastases. They ranged from undetectable to mixed lytic and blastic regions. They developed a finite element model of the shaft using the resolution data with 1-mm cube-shaped elements, as shown in Figure 2.9. The material properties of each element was calculated from the density determined in the QCT scans. The shaft in the FE model were loaded in four-point bending and the cadaveric specimens were loaded under the same conditions to failure.

They observed a strong correlation between the predicted and measured force outputs, and discovered the model remained accurate regardless of the presence of tumor involvement. They concluded that their failure loads are in agreement with previous researchers and that cancerous lesions significantly reduce the strength of the shaft. However, because of the presence of actual metastases, they found that the material properties of cancerous regions were significantly reduced. Therefore, the strength of the shaft was not directly correlated the geometry of the defect, but rather the material properties adjacent to the lesion. Consequently, they were unable to provide further geometric guidelines on the consequences of lesions in long bones. This technique may be applicable for studying benign tumors, however, the structural consequences of metastatic lesions are clearly incomparable to those

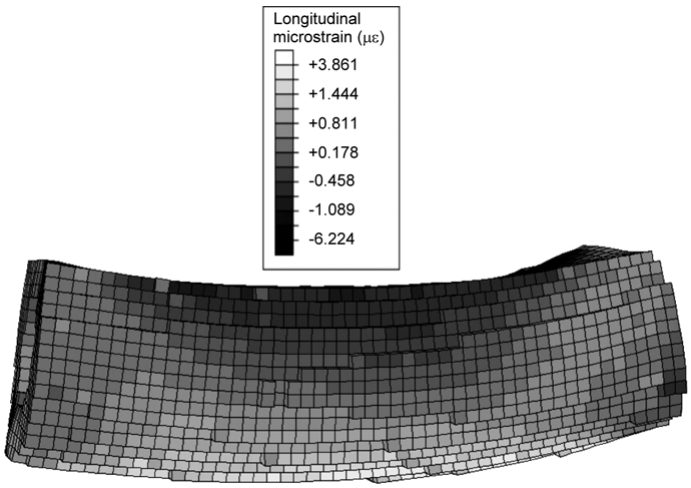

Figure 2.9: Image of finite element model of femoral shaft from QCT scans. Image adapted from Keyak et al. [80]

imposed by equally sized benign lesions. Thus, a separate FE investigation is required to determine the structural consequences of varying defect size and geometries.

A number of studies, including the previous studies, have developed FE models for cadaveric specimens. The challenge associated with cadaveric work is high variability, thus making accurate FE model validation challenging. With the advent of synthetic bone analogues, simpler, validated FE models can be used to make accurate predictions. In 1996, after the introduction of synthetic bone analogues, a standardized geometry computer model was proposed by Viceconti et al. [81] to improve orthopaedic FE simulations. Recently, Cheung et al. [82] developed a computer model based on the improved third-generation model—a previous three-dimensional model was developed for the initial third-generation composite femur, however, due to geometrical and material changes, this computer model was no longer applicable. Cheung et al. constructed the model from CT scans of the third-generation composite femur. This model was later made available for free download and can be found in the Bel Repository at BiomedTown's website. [83] The authors loaded a third-generation composite femur under an axial load with the femur oriented 11° in

abduction. They fixed strain gauges to the surface of the outer cortex to measure the strain at varying locations along the surface of the femur. The bone was removed and was then implanted with a titanium intramedullary nail. The original strain gauges were left in place and additional gauges were added to the surface of the nail. The specimens were loaded again under axial compression in the 11° abduction position. The FE model was setup to duplicate the experimental loading conditions for the bone with and without the nail. Although the purpose of this study was not to focus exclusively on the development of the model, they did comment on the good agreement regarding strain measurements observed between the experimental and FE data.

Soon after, Papini et al. [84] compared the FE results using the third-generation composite femur against cadaveric and synthetic femurs under axial and torsional loads. An image of the model is shown in Figure 2.10. The length, mid shaft diameter, neck angle, and neck to shaft angle were measured for all the cadaveric specimens. The cadaveric femurs were loaded in axial compression at a rate of 8 mm/min up to a maximum of 1.5 kN while the synthetic femurs were loaded at the same rate up to a max displacement of 2 mm. In torsion, the human femurs were loaded up to 12 N-m of torque at a rate of 0.1 deg/sec in external and internal rotation. The synthetic femurs were at a rate of 0.1 deg/sec up to a maximum rotation of ±1.5 deg. The third generation composite femur model was given the material properties of the synthetic femurs provided by the manufacturer. They observed that the medium composite femur was larger than the average cadaveric specimen, so the model was scaled down to match the average shaft diameter.

The researchers observed that very good agreement was achieved between the FE model and the experimental data when small adjustments were made to the material properties in the model. They comment that the model can be "calibrated" to fit a variety of bone qualities, ranging from poor to excellent, by simply modifying the

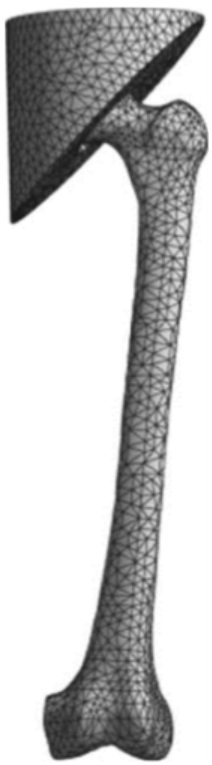

Figure 2.10: Image of the third generation composite femur model in simulated acetabulum for axial and torsional loading. Image adapted from Papini et al. [84]

Young's modulus to match the experimental data. This study validated the use of the third-generation composite femur model, and has been used in a number of studies that utilize the synthetic femurs. Furthermore, since only the material properties were changed in the fourth-generation composite femur, the same model can be used when using synthetic specimens. One primary limitation of this model is the assumption that the bone has linear, isotropic behavior. In real bone, one can expect nonlinear, anisotropic, and viscoelastic behavior, varying greatly depending on the quality of the bone. If, however, these specimens are being utilized for a comparison of groups, such as *treatment A* versus *treatment B*, these specimens, along with the computer model, may be useful for determining small differences between groups while eliminating larger interspecimen variability.

Chapter 3

Experimental Methods, Results, & Discussion

3.1 Experimental Objectives

The purpose of this study was to determine the structural consequences of a 1.5 mm cortical defect on the medial aspect of the distal metaphysis of the femur. This defect was chosen as a model to simulate a small cortical window for the removal of a benign cyst that occupies space, but does not affect the overall quality of the bone. Next, the proposed treatment of augmenting the defect with a 3-hole 1/3 tubular plate was investigated under physiological loading conditions. Fourth-generation composite femurs were chosen to compare fully intact (i.e., no defect), defect, and treated specimens. We hypothesized that the defect would significantly reduce the axial and torsional stiffnesses, and that the plate would restore the structural integrity of the defect bones back to the intact state. This hypothesis was investigated using quasi-static axial and torsional loading, load-to-failure torsion testing, and combined axial/torsional fatigue testing.

(a)

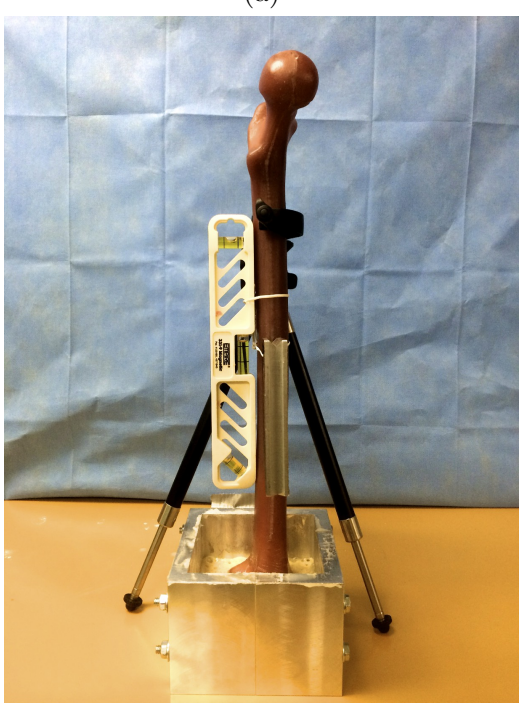

(b)

Figure 3.1: Potting fixture. (a) Anterior-posterior view (b) Medial-lateral view

3.2 Test Specimens

4th generation composite femurs were utilized for biomechanical analysis in this study. The superior most important property used in determining the choice of specimens was to minimize variability. Synthetic specimens offer accurate and consistent geometry and material properties with minimal variability, especially when compared with cadaveric specimens. The purpose of this study was to compare stiffness, fatigue, and load to failure results for three groups: *a*) neat specimens (i.e., no defect and thus no treatment), *b*) defect specimens with no treatment, and *c*) defect specimens augmented with the proposed treatment method.

4th generation medium left composite femurs were obtained from the manufacturer (Sawbones Model #3403, Pacific Research Laboratories, Vashon Island, WA). The 4th generation model is made of a short glass fiber reinforced epoxy resin that is injection-molded around a 17 pcf solid rigid polyurethane foam core, creating the cortical and cancellous regions, respectively. Material properties of the 4th generation models used in this study, provided by the manufacturer [64], are shown in Table 3.1.

3.3 Loading Configuration

The primary loads imposed on the femur are bending, axial compression, and torsion. Additionally, previous studies have reported these as the primary modes of experimental loading for quantification of defect consequences on the stiffness and rigidity femur. [21] True physiological loading combines an eccentric axial/bending load during weight bearing and internal to external torsional loading (caused by weight shift) during the full gait cycle. In order to accurately simulate physiological loading conditions, a custom fixture was utilized to direct the load through the

Table 3.1: Material properties for 4th generation composite femurs. σ = Strength; E = Modulus. [64]

Simulated cortical bone

		Tensile		**Compressive**	
	Density (g/cc)	σ (MPa)	E (GPa)	σ (MPa)	E (GPa)
Longitudinal	1.64	106	16.0	157	16.7
Transverse		93	10.0		

Simulated cancellous bone

		Tensile		**Compressive**	
	Density (g/cc)	σ (MPa)	E (MPa)	σ (MPa)	E (MPa)
Solid	0.27	—	—	6.0	155
Cellular	0.32	—	—	5.4	137

femoral head along the mechanical axis. A custom aluminum simulated acetabulum was previously employed by our laboratory for loading of a femur in axial compression, torsion, and bending. [85] This fixture, modeled after the fixture demonstrated by Papini et al. [84], permits accurate loading for axial and torsional stiffness and fatigue testing. In order to simulate the rigid characteristics of the knee, the femur was cast distally in a thermo-setting liquid plastic (Smooth-Cast® 321; Smooth-On, Inc., Easton, PA) to restrict all translational and rotational motion. The femur was oriented with the anatomical axis 6° off the mechanical axis. The potting configuration is shown in Figure 3.1. The specimens were loaded onto an an MTS 858 Mini Bionix II (MTS Systems Corporation, Eden Prairie, MN) servohydraulic testing machine for testing. The distal cast was placed in a vice fixed atop a 15 kN

axial/torsional load cell. The acetabulum was oriented so the femoral head was 15° in anteversion [84, 86] and lowered until minimal contact was made with the femoral head. The actuator head was raised slightly and a 3.2mm Krischner-wire (Zimmer Inc., Warsaw, IN) was placed through the head to fix the proximal end within the acetabular cup.

Figure 3.2: Loading fixture on the servohydraulic testing machine.

3.4 Preliminary Methods

3.4.1 Sample Preparation

The purpose of the preliminary experiments is to develop an understanding of the torsional and axial effects imposed by the defect prior to any fatigue loading. Preliminary results will be used to conduct a power analysis for determining sample size for the fatigue analysis. Ten 4th generation medium left composite femurs were utilized for preliminary analysis. The specimens were split into two groups: *Group A* consisting of neat femurs with no defect and no treatment, and *Group B* specimens consisting of femurs with a defect and no treatment. The defect was created on the medial cortex, centered between the anterior and posterior surfaces, 55 mm from the distal articular surface. It is hypothesized that approximately a 15 mm diameter cortical window is the maximum sized defect that a 3-hole 1/3 tubular plate will sufficiently support. The femur was rigidly mounted in a vice with the medial cortex exposed for drilling of the defect. A 5/8-inch ($\approx$ 15 mm) steel drill bit was used to create a cylindrical defect through the cortex until the medullary canal was breached. Curettage was simulated using a 3/4-inch ($\approx$ 20 mm) spherical ball end router bit. One half of the bit was ground off to ensure that it would fit through the cortical window. A volume of 4189 mm^3 ($V_{sphere} = \frac{4}{3}\pi r^3$; r = 10 mm) was removed from the cancellous analog material in the canal.

3.4.2 Loading Protocol

The specimens were loaded in three test configurations: *a*) axial compression, *b*) torsion in internal rotation (anterior directed load through femoral head), and *c*) torsion in external rotation (posterior directed load through the femoral head). For axial loading, each specimen was pre-loaded with 100-N in compression and then subjected

to an axial displacement of 2-mm at a rate of 8-mm/min. [84] In torsional loading, the proximal end was subjected to rotational displacements of ±1.5° (internal and external rotation) at a rate of 0.1°/s. Each specimen was loaded first from 0° to 1.5° (external) then unloaded to zero in 1 second. After three repetitions, the test alternated to -1.5° with an unloading rate of 1 second. All three tests were repeated consecutively for three repetitions and the mean value of the three tests was used to represent specimen stiffness. The stiffness was calculated from the linear region on the force-displacement curve for axial loading and the torque-rotation curve for torsional loading (described in further detail in Section 3.4.3). Following stiffness testing, all specimens were loaded to failure in internal rotation. The specimens were pre-loaded with 100-N in compression and rotationally displaced at a rate of 0.1°/s until catastrophic failure occurred.

3.4.3 Statistical methods

Ordinary least squares (OLS) regression, or simple linear regression, was utilized to calculate the regression line for the independent (torque/axial force) and dependent variables (linear/rotational displacement) in the load-displacement plots. Given two vectors, x_i and y_1, we can calculate the OLS regression solution using the following equation:

$$y_i = \beta_0 + \beta_1 x_i + e_i \tag{3.1}$$

Where β_0 and β_1 represent the y-intercept and slope, respectively, and e_i represents the error. For a solution passing through the origin, the OLS solution resolves to:

$$y_i = \beta_1 x_i + e_i \tag{3.2}$$

From this, we can calculate the slope of the regression as $\hat{\beta}$:

$$\hat{\beta} = \frac{\Sigma x_i Y_i}{\Sigma x_i^2} \tag{3.3}$$

The solution for $\hat{\beta}$ can be determined using as a linear algebra formulation:

$$\beta = x_i^{-1} Y_i \tag{3.4}$$

Equation 3.4 was utilized to calculate the stiffness, or slope passing through the origin, for the force-displacement and torque-rotation curves. One-way analysis of variance (ANOVA) was used to statistically compare the stiffness and load to failure results between groups for each of the test configurations. No comparison was made between axial and torsional stiffness within or between groups (e.g., *Group A* axial to *Group A* torsional). For axial and load to failure, only two groups were compared; therefore, the results are equal to a two sample student t-test. Torsional stiffness was compared between groups (e.g., *Group A* internal to *Group B* internal) and within groups (e.g., internal to external within *Group A*). A level of $p_{\surd} \leq 0.05$ was considered statistically significant.

3.5 Preliminary Results

3.5.1 Measurement of Axial Stiffness

The mean stiffness of the neat group *Group A* was 1.23 ± 0.07 kN/mm (Figure 3.3a), while the stiffness of the defect group *Group B* was only 1.16 ± 0.08 kN/mm (Figure 3.3b), resulting in a reduction in stiffness of ≈ 6%. However, statistical analysis revealed no statistical difference in axial stiffness between the two groups ($p = 0.086$). Overall, there was a 5.5% coefficient of variation (COV = standard deviation/mean) for stiffness in the neat group among all 15 collected values ($n_{group} = 5 \times 3$ tests each). Similarly, a COV = 7.0 % was observed for measurements of axial stiffness in the defect group. Figure 3.3 shows the axial force versus displacement curves for the neat and defect specimens. The solid black line represents the linear least square regression of force and displacement.

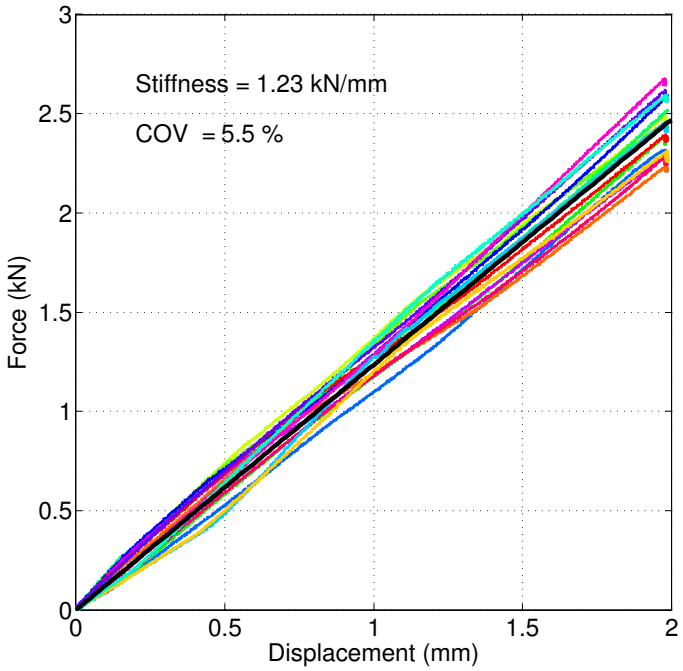

(a) Neat

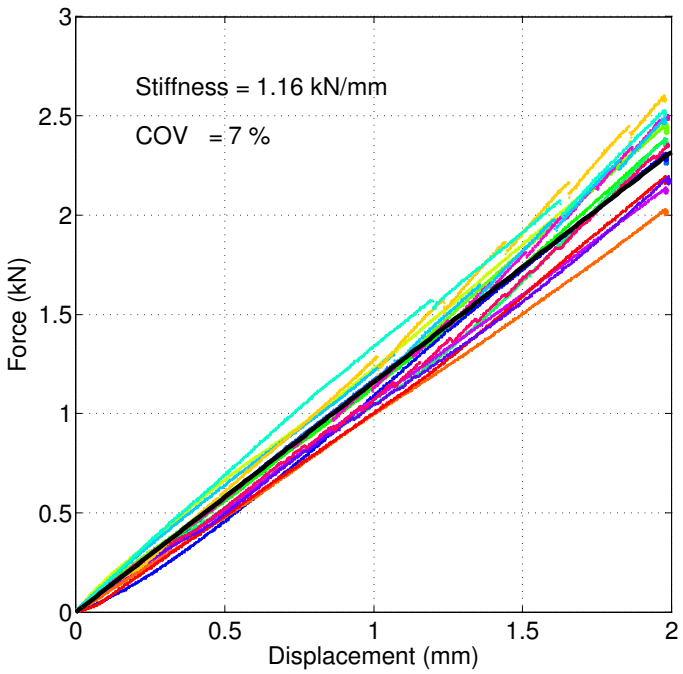

(b) Defect

Figure 3.3: Axial force (kN) vs. displacement (mm)

3.5.2 Measurement of Torsional Stiffness

The internal torsional stiffness was measured as the linear relationship between the torque and the rotation for an anterior directed load through the femoral head, and the external rotation was for a posterior directed load through the femoral head. The mean internal torsional stiffness of the neat group, *Group A*, was 4.92 ± 0.42 N· mm/degree (Figure 3.4a), while the internal torsional stiffness of the defect group *Group B* was only 4.53 ± 0.56 N·mm/degree (Figure 3.4b). The introduction of the defect resulted in a reduction in stiffness of ≈ 8%. The mean stiffness of external torsional stiffness for the neat specimens was 5.16 ± 0.26 N·mm/degree (Figure 3.5a). The external torsional stiffness of the defect group reduced to 4.67 ± 0.32 N·mm/degree (Figure 3.5b), resulting in ≈ 10% loss in stiffness. No statistical difference was detected between the neat and defect specimens in internal rotation ($p = 0.14$). There was, however, a statistical difference between the groups for external rotation ($p = 0.006$). No statistical difference was detected between internal and external rotation within groups (*Group A*: $p = 0.5$; *Group B*: $p = 0.4$), indicating that the two rotational tests are statistically equivalent within specimen types. The greatest inter-specimen variation in stiffness was observed for internal rotation of the neat specimens with a COV = 8.4 %, followed by internal rotation of the defect specimens with a COV = 7.3 %. Lower variation was observed in the defect stiffness tests than in the neat stiffness tests, which was likely due to the introduction of a stress concentration. No plastic deformation was observed in any of the specimens.

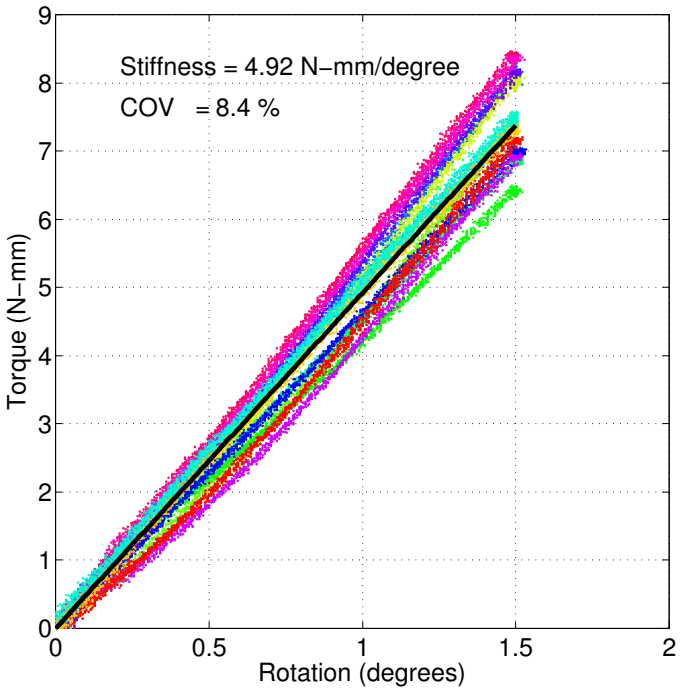

(a)

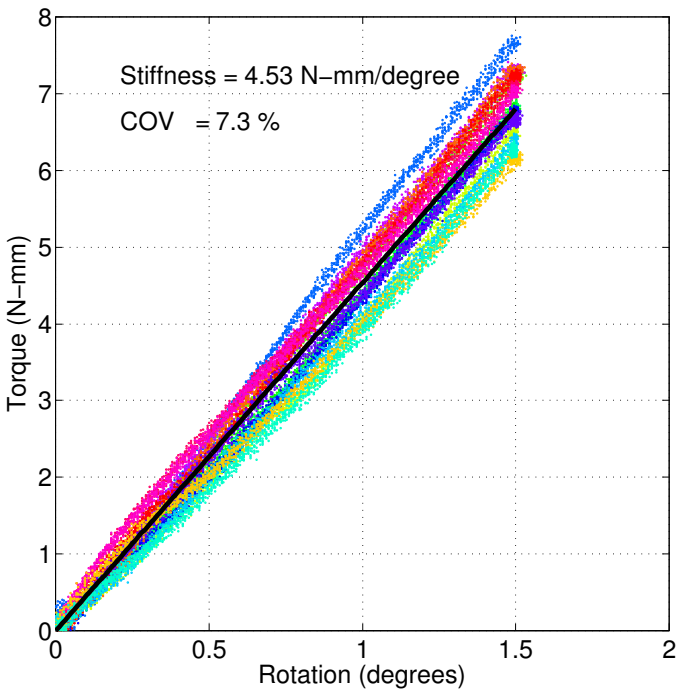

(b)

Figure 3.4: Torsional load (N-mm/degree) vs. internal rotation (deg). (a) Neat. (b) Defect.

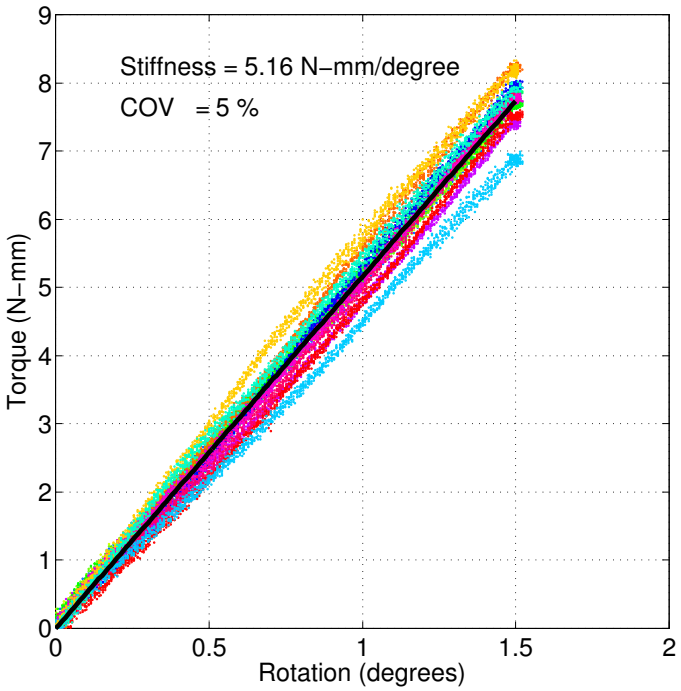

(a)

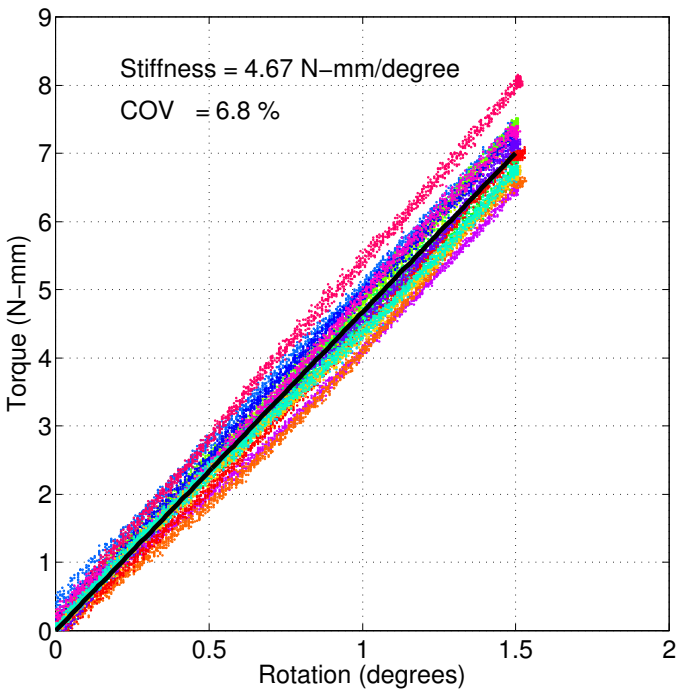

(b)

Figure 3.5: Torsional load (N-mm/deg) vs. external rotation (deg). (a) Neat. (b) Defect.

3.5.3 Load to Failure

No specimens were failed or permanently damaged during preliminary stiffness testing. Figure 3.6 shows the load to failure torque-displacement plots for all ten specimens. Load to failure analysis was conducted to determine the maximum load, denoted as ultimate load (τ_U), that the specimen can withstand prior to catastrophic failure. The values of τ_U, mean τ_U per group, final rotation at τ_U (δ_R), and the statistical difference between groups can be found in Table 3.2. The load to failure tests also reveal the failure locations for each group, which in addition to τ_U, provides important clinical information about the significance of introducing the defect.

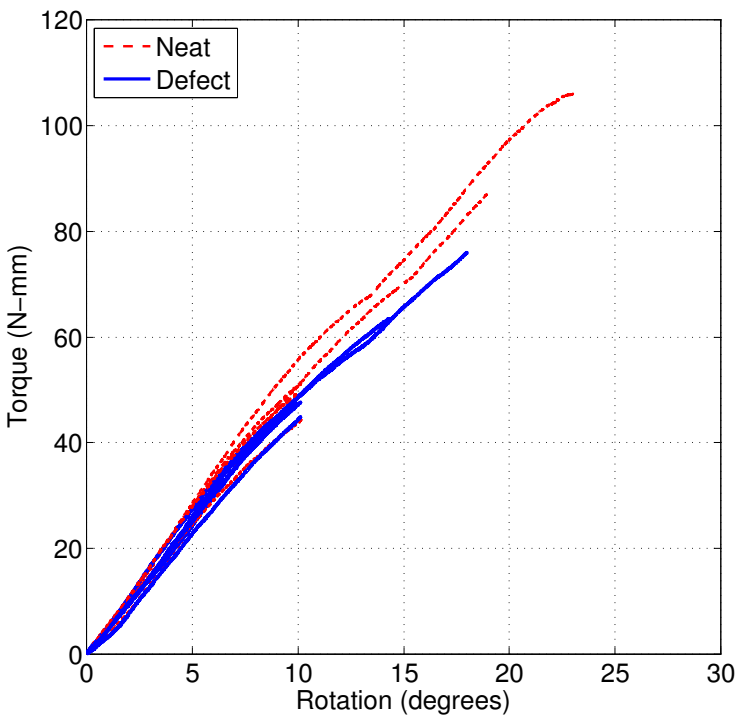

Figure 3.6: Internal torsional load to failure (N-mm/deg) versus rotation (deg) of neat and defect specimens.

All neat specimens failed through catastrophic fracture of the femoral neck. Four of the five defect specimens failed through a spiral fracture propagating from the

anterior cortex, through the center of the defect, and ending approximately 250 mm proximal to the defect in the diaphysis. One defect specimen failed through the fracture of the femoral neck, however, the value of τ_U was not significantly affected. Figure 3.7 shows the two modes of failure observed.

Table 3.2: Load to failure results including ultimate loads, rotation at ultimate, mean per group, and statistical difference between ultimate loads.

Specimen	**#**	$\tau_{\mathbf{U}}$ **(N-mm/deg)**	$\delta_{\mathbf{R}}$**(deg)**	$<\tau_{\mathbf{U}}>$ **(N-mm/deg)**	**P-value**
Neat	1	87.9	19.1	67.8 ± 27.5	0.42
	2	106.0	23.0		
	3	51.2	10.2		
	4	44.3	10.2		
	5	49.5	10.0		
Defect	1	63.6	14.3	56.0 ± 13.4	
	2	76.0	18.0		
	3	47.8	10.0		
	4	44.9	10.2		
	5	47.8	10.2		

3.5.4 Power Analysis

A sample-size selection power analysis was conducted with the preliminary results for ultimate load. The power analysis is used to predict the minimum number of specimens needed to observe a statistically significant difference between both groups. The analysis was completed using two different methods: *a*) a student t-test for the two groups tested *b*) a one-way analysis of variance (ANOVA) for the two groups tested plus a third estimated group. A statistical hypothesis was developed using a

t-test for the neat and defect groups, which assumes

$$\begin{aligned} &\mathrm{H}_o : \mu_1 = \mu_2 \\ &\mathrm{H}_a : \mu_1 \neq \mu_2 \\ &\alpha = 0.05 \end{aligned} \tag{3.5}$$

where the subscripts o and a denote the null and alternative hypotheses, respectively. Since we do not know the variances of the groups to be tested, assumptions of both equal and unequal variances were tested using the t-test. By testing both conditions, a more thorough prediction of sample size can be made, that accounts for both possible statistical circumstances. A similar hypothesis was developed for the ANOVA:

$$\begin{aligned} &\mathrm{H}_o : \mu_1 = \mu_2 = \mu_3 \\ &\mathrm{H}_a : \mu_1 \neq \mu_2 \neq \mu_3 \\ &\alpha = 0.05 \end{aligned} \tag{3.6}$$

where the neat, defect, and treatment group are all being considered. This analysis assumes a standard deviation of unity, $\sigma = 1$, for all groups. An analysis was conducted for both tests in which the minimum detectable difference was varied along an array of sample sizes $n = 3 : 10$. The minimum effect size, or minimum detectable difference, is the difference in the measured variable that is detectable between groups using the chosen statistical methods. An analysis was iterated through each value of n at each effect size. A power ≥ 0.80 (i.e., the probability of not making a β error, or wrongfully accepting H_o) was considered for sample size selection. This allows for a confident choice of sample size that provides a high probability of detecting a statistical difference between groups. A sample size of N = 3–10 was considered so that a statistical analysis could be conducted for the experiments. The results of the power analysis for each test are shown in Figures 3.8, 3.9, and 3.10. The regions above the black lines indicate a statistical power ≥ 0.80.

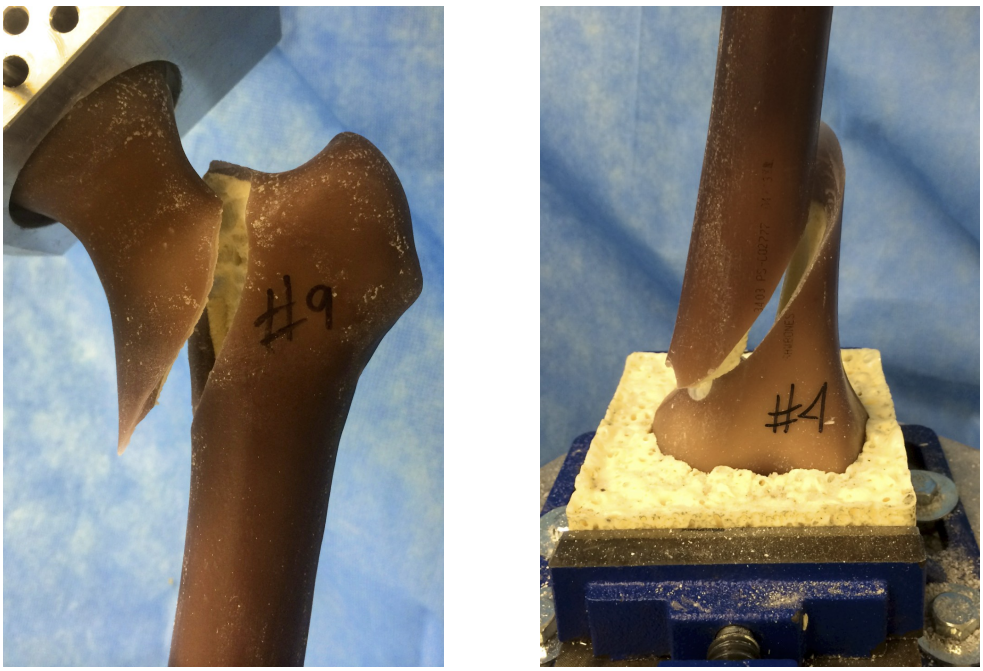

(a) (b)

Figure 3.7: Neck and spiral fracture failure modes. (a) Neck fracture in absence of defect. (b) Spiral fracture through defect.

3.6 Fatigue Analysis Methods

3.6.1 Sample Preparation

A total of 16 specimens were divided into two groups of 8 femurs. All 16 specimens were subjected to the 1.5-cm cortical defect as described in Section 3.4.1. 8 of the specimens were not treated with any method of stabilization. The remaining 8 specimens were treated with a 3-hole 1/3 tubular plate (Stryker®, Kalamazoo, MI). After the creation of the defect, the curettage bit was removed and replaced with a 0.098-inch (2.5-mm) drill bit, according the manufacturer's recommendations for

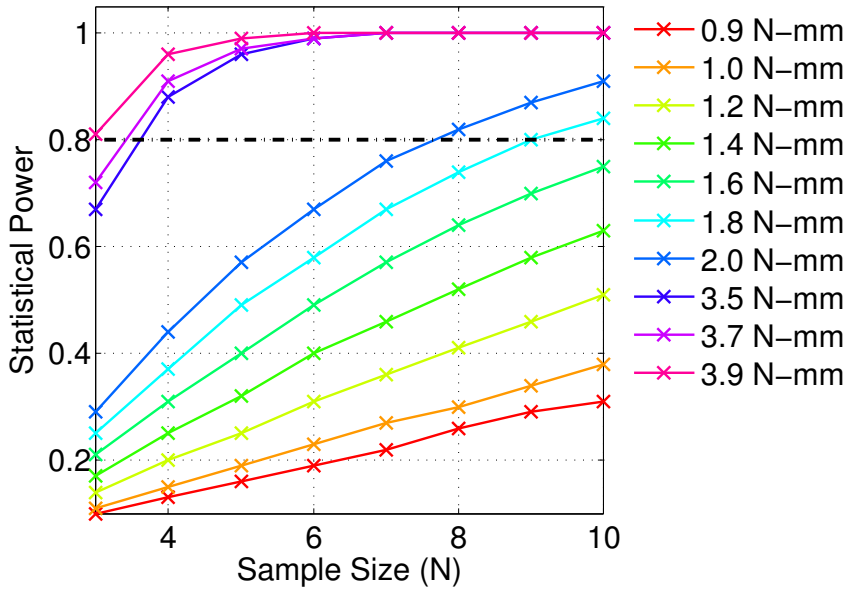

Figure 3.8: Statistical power $(1 - \beta)$ versus sample size for varying minimum detectable differences for T-Test: $\sigma_1 \neq \sigma_2$.

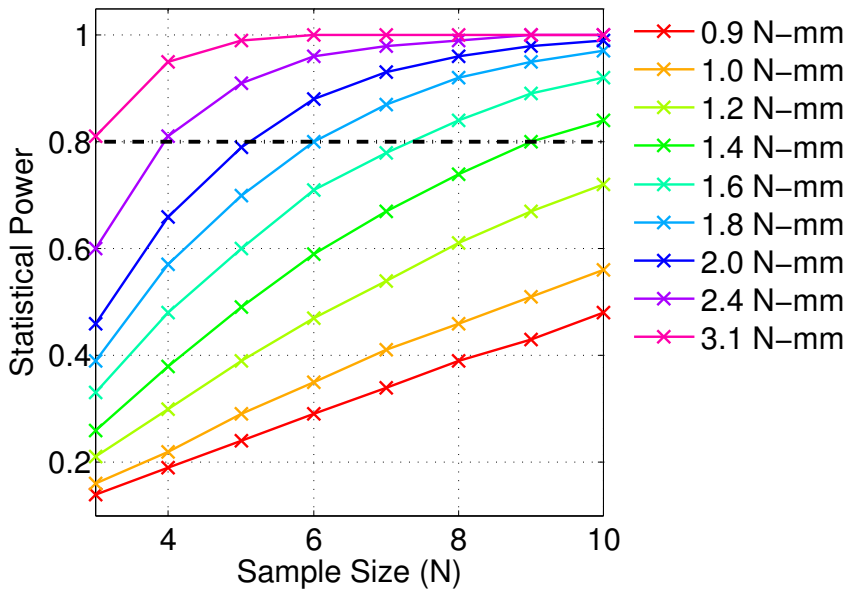

Figure 3.9: Statistical power $(1 - \beta)$ versus sample size for varying minimum detectable differences for T-Test: $\sigma_1 = \sigma_2$.

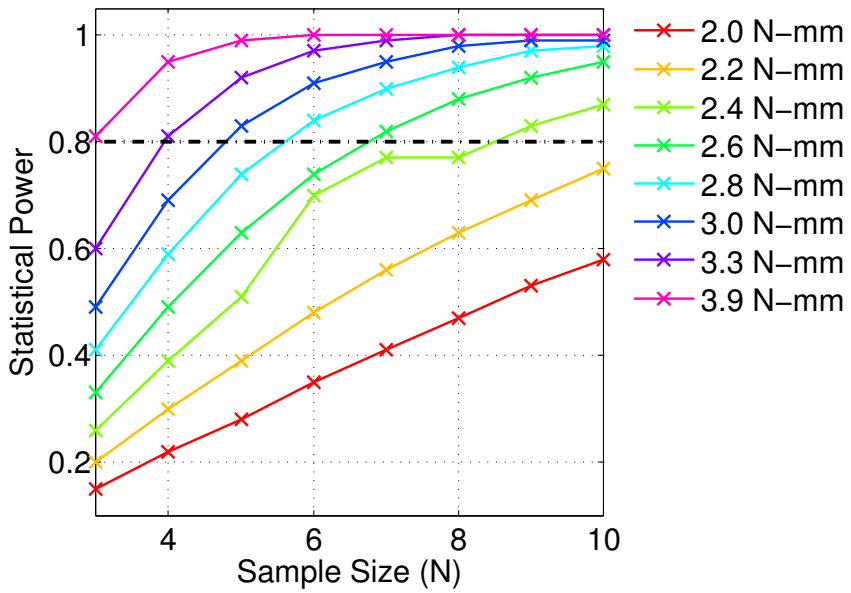

Figure 3.10: Statistical power $(1 - \beta)$ versus sample size for varying minimum detectable differences for ANOVA: $\sigma_1 = \sigma_2$.

screw pilot holes. The bone remained in place while the pilot hole was drilled through the center of the defect. The bone was removed from the vice and one 3.5-mm non-locking cortical screw was placed through central hole of the plate and into the pilot hole in the far cortex. The holes on the proximal and distal sides of the defect were measured and aligned directly through the anatomical axis of the femur. The plate was left loose while the two pilot holes were drilled with the drill press. The remaining two non-locking screws were hand-tightened with a torque limiting screw driver up to the manufacturers specifications. Finally, the central screw was tightened down until the contour of the plate followed the natural curvature along the distal-medial cortex of the specimen. The recommended torque value was not achieved for the central screw since the near cortex was not in place to provide resistance for the head of the screw. The test was repeated for a total of eight specimens.

3.6.2 Loading Protocol

The specimens were loaded under combined axial-torsional loads for up to 10,000 cycles, or until catastrophic failure occurred. 10,000 cycles is the approximate number of cycles in a 6 month period of use—if healing has not occurred by this time, revision surgery may be required to achieve proper outcomes. Each specimen was pre-loaded with 15-N in compression and no torsional pre-load. The specimens were cycled between 50–500-N in axial compression and between $\pm 6^{\circ}$ for torsion at a rate of 2-Hz for both. [85] The running time, axial force, axial displacement, torque, and rotation were recorded during the duration of the cyclic test at a rate of 1000-Hz ($\approx$ 500 data points per cycle). In order to separate the data more easily, the same output variables were recorded at cycles 10, 100, and every 100th cycle thereafter until the completion of the test.

3.6.3 Data Analysis

The stiffness was evaluated as the linear portion of the loading region of the fatigue curves. For consistency, the initial stiffness was determined as the slope, calculated between 75 data points on the loading curve, of the 10th cycle of all the force-displacement curves. The internal and external torsional stiffnesses were determined independently on the loading curves of the torque-rotation curves in each direction. Ordinary least squares linear regression, as described in Section 3.4.3, was used to fit the two vectors. For the fatigue analysis, a two-sample student t-test was utilized to determine the statistical difference between time to failure (in cycles) between the treated and un-treated groups.

3.6.4 Damage Accumulation

The effects of fatigue loading prior to catastrophic failure of a material are challenging to observe, and therefore must be characterized separately. Fatigue loading of a material induces local stresses and strains of the individual elements within the volume. In metals, this takes the form of dislocations, resulting in microcracks and voids. In organic materials, this process occurs as the alteration of intermolecular bonds. Regardless of the form, the resulting irreversibility in microstructural characteristics after the fatigue process is the fundamental phenomenon of damage. According to Lemaitre and Chaboche, *A material is said to be free of damage if it is devoid of cracks and cavities at the microscopic scale, or from a more pragmatic point of view, if its deformation behaviour is that of the material formed under the best conditions.* [87] The theory of damage provides us with the ability to characterize the evolution of material from the initial state to the state at which crack initiation has occurred. This principle can be extended into the characterization of bones and bone-implant assemblies over a period of cyclic loading. We will utilize the damage principles described herein, adapted from Lemaitre and Chaboche [87], to characterize the evolution of damage in the femoral specimens after being subject to cyclic loading. According to the uniaxial elastic damage law, we describe an initial stress state as σ' and a damaged stress state as σ , where

$$\sigma' = \frac{\sigma}{1-D} = E\epsilon_0 \tag{3.7}$$

or

$$\sigma = E(1-D)\epsilon_0 \tag{3.8}$$

where E is the modulus of elasticity in the absence of any damage, then

$$D = 1 - \frac{\sigma}{E\epsilon_0} \tag{3.9}$$

If we consider a damaged state, then

$$\sigma = E'\epsilon_0 \tag{3.10}$$

Therefore, damage can be represented by

$$D = 1 - \left(\frac{E'}{E}\right) \tag{3.11}$$

and torsional damage

$$D = 1 - \left(\frac{G'}{G}\right) \tag{3.12}$$

where G is the modulus of rigidity. The subsequent solutions for axial and torsional damage have been adapted from Lemaitre and Chaboche. [87]

Axial Damage

We begin with a relationship for displacement:

$$\Delta = \frac{PL}{AE} \tag{3.13}$$

where P is the load, L is the length of the specimen, A is the cross-sectional area, and E is Young's modulus. Recalling that the stiffness is the force divided by the displacement, we can define the initial Young's modulus in terms of the initial, or effective, stiffness.

$$E = \frac{k_{\text{eff}}L}{A} \tag{3.14}$$

The effective stiffness was calculated as the line connecting the displacements at the minimum and maximum forces on the force-displacement curve of the tenth cycle. The use of the tenth cycle permits pre-conditioning of the construct while retaining reasonable estimates for stiffness prior to the onset of permanent damage. We can then use the relationship in Equation 3.14 to calculate the Young's modulus for any

cycle thereafter, denoted as E'. Substituting the values of Young's modulus into Equation 3.11, we determine a relationship for the damage as a function of change in modulus.

$$D = 1 - \frac{\left(\frac{k_{\mathrm{n}}L}{A}\right)}{\left(\frac{k_{\mathrm{eff}}L}{A}\right)} \tag{3.15}$$

where $k_{\mathrm{eff}} = k_{\mathrm{cycle\ 10}}$ and k_{n} is the stiffness of any cycle thereafter. However, we observe from this equation that if we make the assumption that the length, L, and the area, A, remain constant throughout the duration of the fatigue analysis, the equation of damage reduces to a relationship involving only the stiffness of the construct:

$$D = 1 - \frac{k_{\mathrm{n}}}{k_{\mathrm{eff}}} \tag{3.16}$$

We see from this result that if the material stiffness changes, the value of damage approaches 1, indicating complete failure or loss of stiffness. If, however, the damage trends towards negative values of damage, the stiffness of the material is increasing, and thus the construct is likely undergoing hardening.

Torsional Damage

A similar argument can be made for the characterization of fatigue behavior after torsional loading. Instead of the linear displacement we consider the rotation, or angle of twist, defined as ϕ.

$$\phi = \frac{TL}{JG} \tag{3.17}$$

where T is the torque, L is the length, J is the polar moment of inertia, and G is the torsional rigidity. After algebraic manipulation, we find:

$$G = \frac{TL}{\phi J} \tag{3.18}$$

Similarly, we recall that the torsional stiffness can be evaluated as torque divided by the rotation, or

$$k_{\text{eff}} = \frac{T}{\phi} \tag{3.19}$$

Substituting this into Equation 3.18, we find an expression for the torsional rigidity at cycle 10:

$$G = \frac{k_{\text{eff}} L}{J} \tag{3.20}$$

and the damaged rigidity

$$G' = \frac{k_{\text{n}} L}{J} \tag{3.21}$$

at any cycle n thereafter. Substituting these relationships into Equation 3.12, we find that:

$$D = 1 - \frac{\left(\frac{k_{\text{n}} L}{J}\right)}{\left(\frac{k_{\text{eff}} L}{J}\right)} \tag{3.22}$$

Making the same assumption as for axial damage, the length and polar moment of inertia cancel, resulting in an equation for damage dependent only on the torsional stiffness:

$$D = 1 - \frac{k_{\text{n}}}{k_{\text{eff}}} \tag{3.23}$$

The torsional stiffness was calculated as the line connecting the minimum and maximum torque of the torque-rotation loading curve for each 100th cycle after cycle 10. The results of the damage analysis will reveal an increase in damage (approaching the value of 1) as the stiffness of the construct decreases over the fatigue period. In the same way as the axial damage analysis, if the stiffness increases, the damage will decrease below zero, indicating that the construct is hardening.

3.7 Fatigue Analysis Results

3.7.1 Patterns of Failure

A summary of the results of the fatigue analysis are shown in Table 3.3. Among the defect specimens, 5 of 8 specimens failed catastrophically by a spiral fracture through the cortical defect. Two specimens survived all 10,000 cycles without any crack formation or failure. Finally, one specimen failed along the k-wire through the femoral head. Among the treated specimens, three specimens survived all 10,000 cycles, however, cracking through the defect was observed in all three. Two specimens failed catastrophically by a spiral fracture through the defect, as shown in Figure 3.11. Finally, three specimens failed by fracture of the femoral neck, and two of the specimens had small cracks formed through the defect. The results of the two-sample student t-test revealed no statistical difference (P = 0.5087) in time to failure between the two groups.

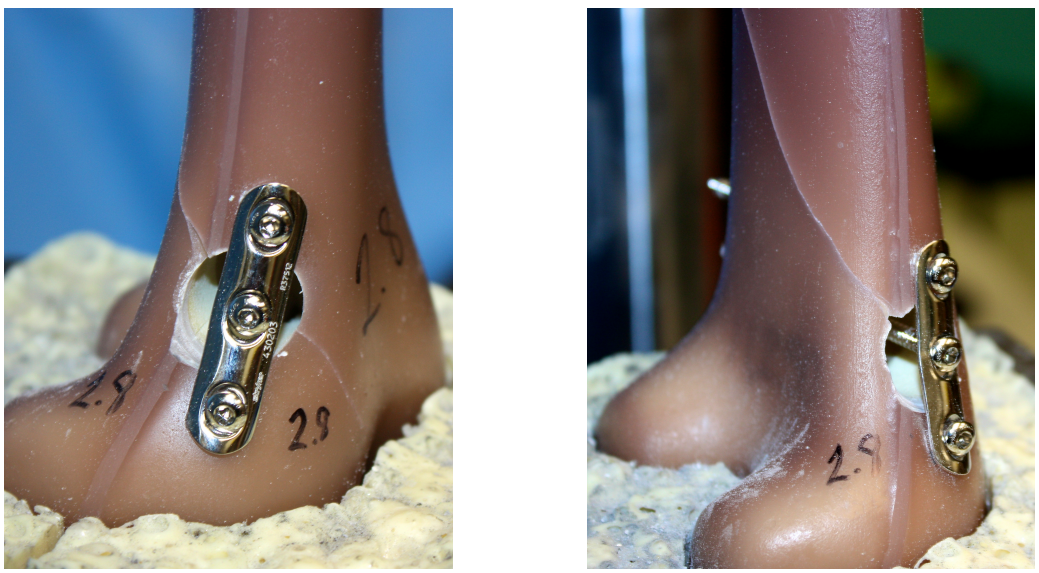

(a) (b)

Figure 3.11: Spiral fracture through treated defect. (a) Anterior oblique medial/lateral view. (b) Posterior oblique medial/lateral view.

Table 3.3: Summary of fatigue results including time and mode of failure.

Group	**Spec. #**	**Life**	**Mode of Failure**
Defect	1	1,311	Spiral fracture through defect
	2	10,000	No failure or cracking
	3	450	Spiral fracture through defect. Crack formed by 100 cycles
	4	6,750	Fracture through femoral head along k-wire
	5	1,205	Spiral fracture through defect
	6	4,500	Spiral fracture through defect
	7	10,000	No failure or cracking
	8	2,129	Spiral fracture through defect
Plate	1	10,000	No failure. Visible crack formed on anterior side of defect around 9,000 cycles
	2	3,006	Fracture through femoral neck. Crack formed through defect
	3	6,708	Fracture through femoral neck. Long crack formed through defect
	4	10,000	No failure. Small crack formed by 8000 cycles
	5	515	Spiral fracture through defect
	6	717	Fracture through femoral neck. No crack formed through defect
	7	10,000	No failure. Very long fracture line through defect
	8	6,250	Spiral fracture through defect

3.7.2 Fatigue Behavior

Axial Fatigue

Although axial and torsional cyclic tests were conducted simultaneously, the data for each test were isolated and analyzed separately. In this section, the axial data is analyzed to observe the behavior of the axial fatigue period. The initial stiffness was determined as the linear region of the loading curve of the 10th cycle. This permitted pre-conditioning of the construct yet the stiffness was determined prior to the onset of damage. Figure 3.12 shows plots of the axial compression versus displacement for defect and treatment specimens at the 10th cycles. The bold region is the area of the loading curve used to determine the initial, or effective, stiffness. The mean effective stiffness of the defect group was 1.27 kN/mm (SD: $\pm$ 0.43; range: 0.85–2.32 kN/mm) with a COV = 33.6 %. Interestingly, the treatment group had a lower mean effective stiffness of 1.07 kN/mm (SD: $\pm$ 0.16; range: 0.80–1.31 kN/mm) with a COV =15.1 %. A two-sample student t-test revealed no statistical significance between the average effective stiffnesses of the defect and treatment groups ($p = 0.27$). It is important to compare the initial stiffness results to the values of stiffness determined under quasi-static axial loading, in the absence of a torsional load. The neat specimens had an axial stiffness of 1.23 kN/mm while the defect specimens had a stiffness of 1.16 kN/mm. Although the values vary slightly, an analysis of variance revealed no statistical difference between any of the four groups ($p = 0.52$). The results of the axial fatigue experiments reveal a general trend towards change in the non-controlled variable, displacement. Figures 3.13a and 3.13b show the axial displacement over the course of the fatigue analysis for fractured and non-fractured specimens, respectively. Figure 3.13a shows the displacement behavior of a specimen that failed catastrophically by a spiral fracture through the defect site. The mean displacement increased slightly until $\approx$ 4500 cycles when the bone failed catastrophically.

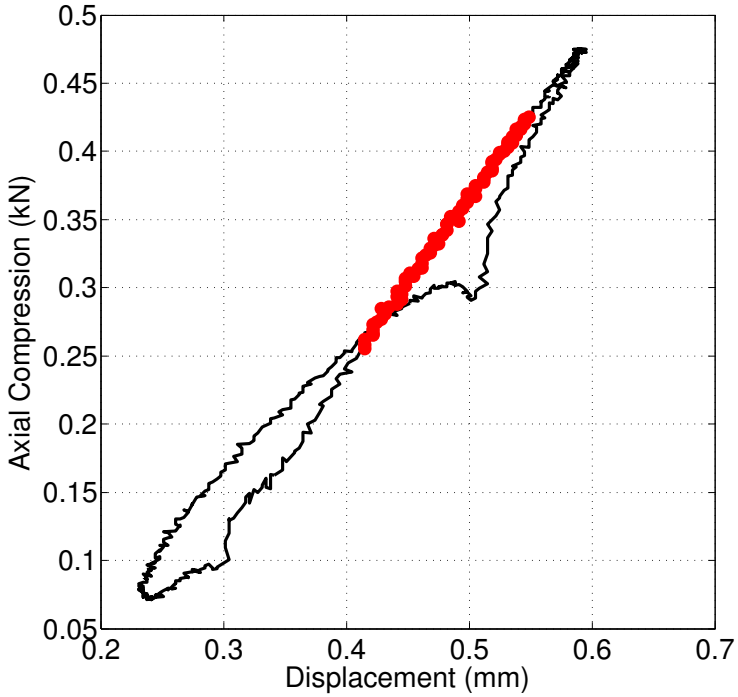

Figure 3.12: Axial force (kN) versus displacement (mm) at the 10th cycle for Specimen 2.7. The stiffness is emphasized by the bold region.

This is indicated by the large increase in displacement cycle amplitude from $\approx$ 0.5-mm to $\approx$ 0.65-mm. During failure, the specimen failed by a spiral fracture propagating proximally and posteriorly from the posterior edge of the medial defect in a clockwise direction. Generally, a small piece of the cortex remained intact on the anterior surface, which permitted the bone to still resist the axial load at the expense of a greater displacement. This can be observed in Figure 3.13a by the increase in displacement after cycle 4500. Figure 3.13b shows a specimen that survived the 10,000 cycle test. It can be observed that while the amplitude of each cycle remained constant throughout the test ($\approx$ 0.325 mm), the mean displacement increased by $\approx$ 0.1-mm. This indicates the onset of material change occurring within the construct over the course of the experimental life. The onset of change in the construct is further illustrated in the force-displacement plots of varying cycles over

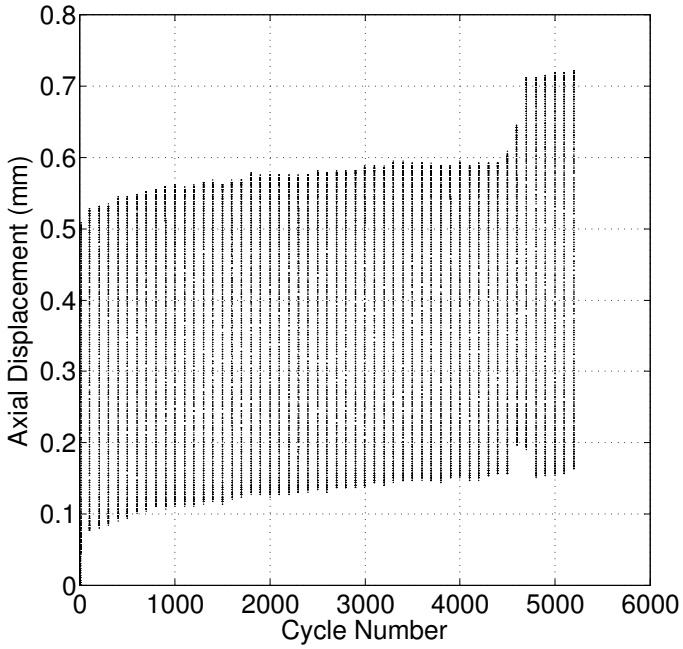

(a)

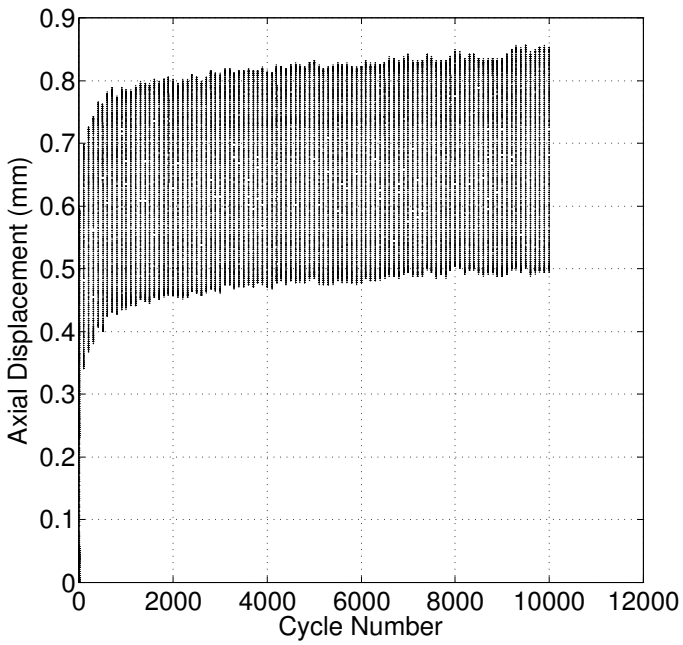

(b)

Figure 3.13: Axial force (kN) versus cycle number for survived and fractured specimens. (a) Specimen 1.6—Failed by a spiral fracture through the defect. (b) Specimen 2.7—Survived 10,000 cycles but large crack formed.

the period of the fatigue analysis, as shown in Figure 3.14. This change induces a shift in mean displacement for the same compression range, resulting in a lateral shift along the displacement axis of the force-displacement plots. These data can be compared to cycle versus displacement data for the same specimen shown in Figure 3.13b to observe the onset of material change.

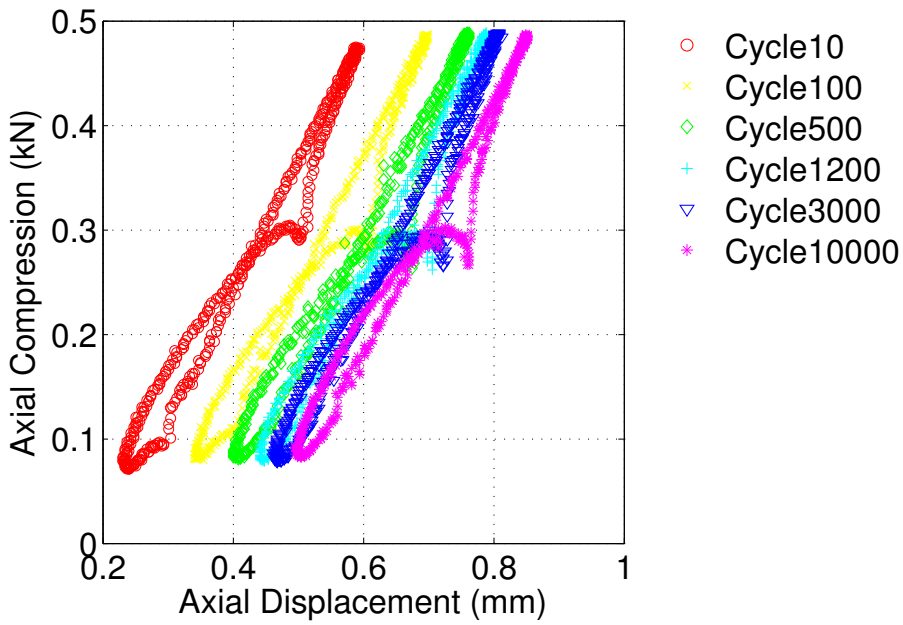

Figure 3.14: Axial force (kN) versus displacement (mm) for Specimen # 7 in the treatment group.

The methods described in Section 3.6.4 are employed to determine if the construct is undergoing damage or hardening. Figure 3.15 shows the damage plots of two specimens: a failed specimen (1.6—solid red) and an unfailed specimen (2.4—dashed blue), respectively. We see from this figure that the constructs in fact undergo hardening. The solid line shows the progressive hardening of the specimen until $\approx$ 4500 cycles, when the specimen failed completely through the defect. The dashed line shows the progressive hardening of specimen 2.4 over the course of all 10,000 cycles. The material hardens by $\approx$ 50%, but successfully survives the test period.

The described definition of damage considers the change in stiffness relative to the initial stiffness. Intuitively, it make sense that hardening is likely to occur. As the construct is loaded under compression, the small voids and spaces are likely filled with surrounding material. This leads to a more condensed material with fewer voids, and thus a higher stiffness. This may also explain the lateral shift in mean displacement under the same loading constraints. As the voids are filled, the material compresses and shortens, causing the mean displacement of the actuator head to increase relative to the starting position. Ultimately, the construct is likely to become brittle after significant hardening. This may explain why 3 of the 8 treated specimens failed through fracture of the femoral neck prior to failure through the defect. The phenomenon of hardening will be further investigated in Chapter 4 through a numerical stress analysis.

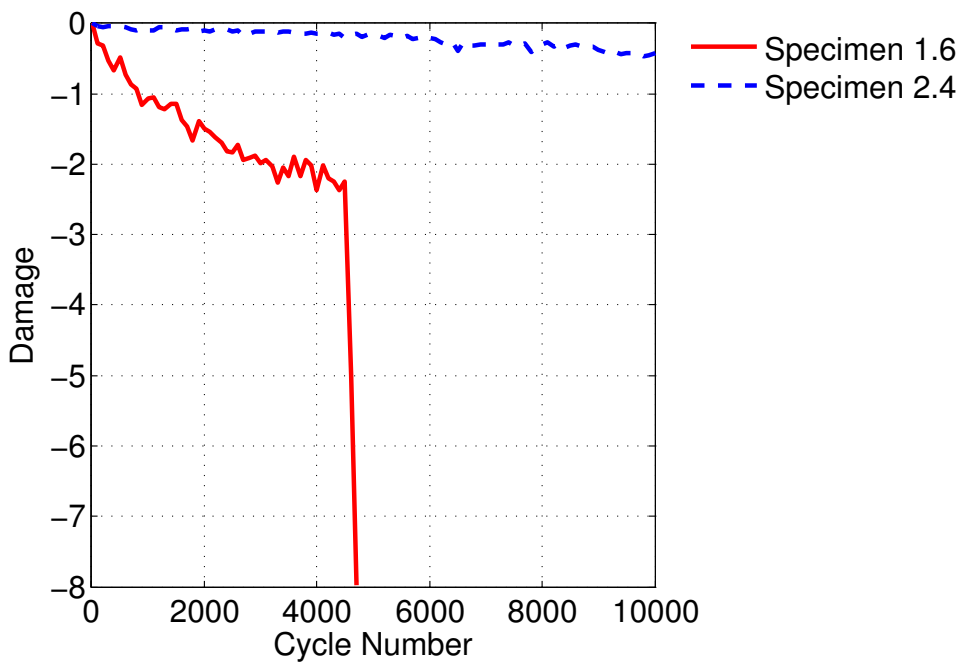

Figure 3.15: Axial hardening versus cycle number for a failed and unfailed specimen.

Torsional Fatigue

The defect and treatment specimens were exposed to rotations of ±6° to simulate the internal and external rotations of the femoral head during the gait cycle. The torsional effective stiffnesses of the constructs were determined as the linear region of the loading curves in both the internal and external rotational directions. Figure 3.16 shows a representative torque-rotation curve for a one of the specimens in the untreated defect group. The bold region was used to determine the construct's effective stiffness in each direction.

The mean torsional stiffness of the defect specimen in the +6° direction was 6.67 ± 0.48 N-mm/degree (COV = 7.25 %) and the mean stiffness in the −6° direction was 5.88 ± 1.98 N-mm/degree (COV = 33.8 %). The treatment group had a mean stiffness of 6.58 ± 0.35 N-mm/degree in the +6° direction (COV = 5.37 %) with a mean stiffness of 5.90 ± 2.01 N-mm/degree in the −6° direction (COV = 34.1 %). Recalling the stiffness results from quasi-static testing, one can observe that the stiffness of the neat specimens in the (+) direction (external rotation) was 5.16 N-mm/degree. The stiffness of the defect specimen in external rotation was 9.5% less than the neat specimen with a value of 4.67 N-mm/degree. In internal rotation, the neat specimens had a stiffness of 4.92 N-mm/degree, while the defect specimens had a stiffness of 4.53 N-mm/degree (-7.9%). Analysis of variance of the external rotation results revealed a statistical difference between all four groups of $p < 0.001$. A pair-wise comparison revealed statistical differences between multiple groups: the mean stiffness of the fatigue defect group was statistically higher than the neat specimens and the defect preliminary group; the mean stiffness of the treatment fatigue group was statistically higher than both the neat and defect specimens from the preliminary tests.

Following the stiffness analysis, we analyze the torsional behavior of the con-

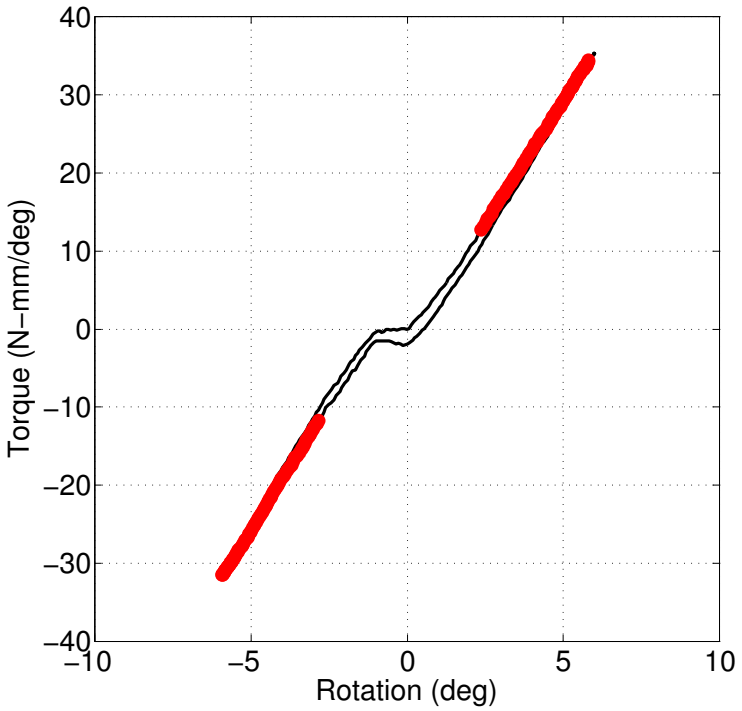

Figure 3.16: Torsional moment (N-mm/deg) versus rotation (deg) at the 10th cycle for specimen 1.3. The stiffness region is emphasized by the bold markers.

structs over their fatigue life. Figure 3.17 shows the torsional moment versus cycle number for failed and unfailed specimens from the defect and the treatment groups, respectively. Figure 3.17a shows the data for a specimen that failed at $\approx 4,500$ cycles. It can be observed that the torsional moment is mostly constant leading up to this point of catastrophic failure. Leading up to the point of failure, the specimen seemed to undergo minimal damage accumulation. At the failure point, the specimen underwent brittle failure by a spiral fracture through the defect. Figure 3.17b shows the torsional moment of a treatment specimen that survived all 10,000 cycles. It can be observed that the amplitude of the torque output reduces slightly until approximately 9,000 cycles. At this time, a visible crack formed on the anterior cortex of the defect. This dramatically reduced the torsional moment, however, failure did not occur by the end of the 10,000 cycle test.

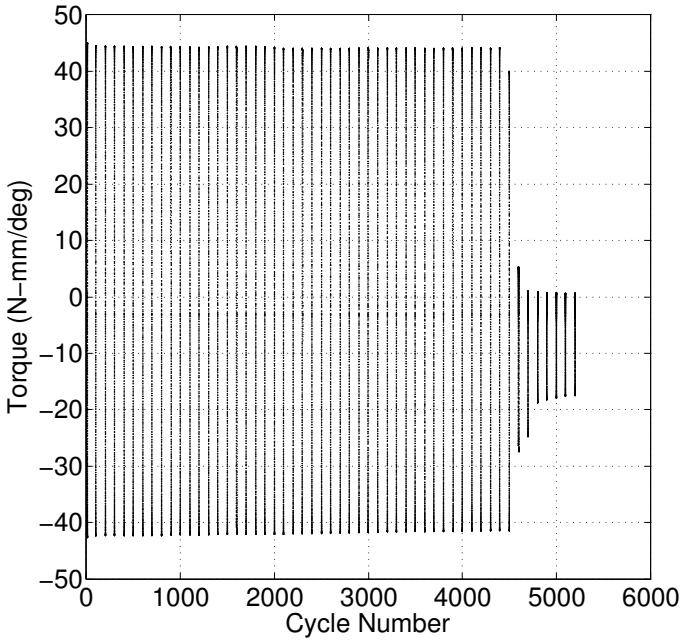

(a)

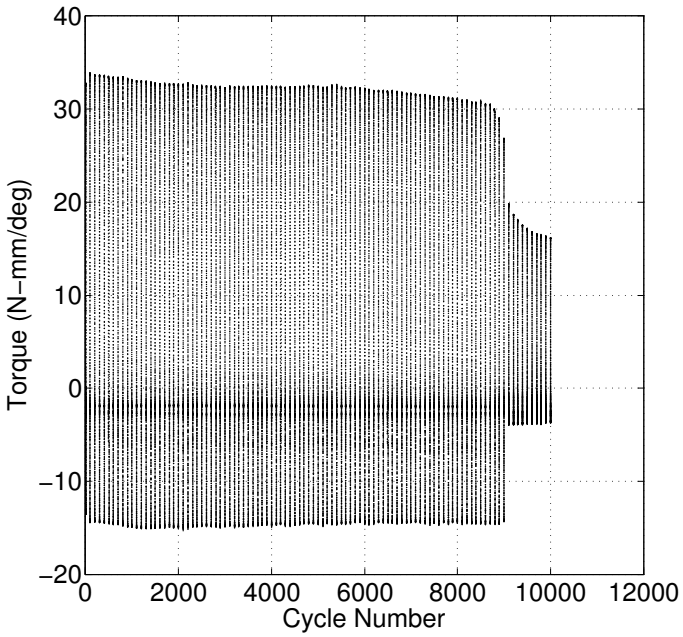

(b)

Figure 3.17: Torsional moment (N-mm/deg) versus cycle number for a defect and treatment specimen. (a) Specimen 1.6. (b) Specimen 2.1.

The change in torsional load in damaged specimens is further illustrated by observing the torsional moment versus rotation plot for varying cycles across the fatigue life. Figure 3.19a shows the torsional moment versus rotation for the same specimen in Figure 3.17a. It can be observed that very little damage, or change in the hysteresis loop, has occurred leading up to the point of failure. Since failure occurred between cycles 4500–4600, there is a dramatic reduction in torsional moment between these two loops. In contrast, a specimen such as that represented in Figure 3.17b undergoes visible damage over the course of the test. In the torsional moment versus rotation plot, shown in Figure 3.19b, in can be observed that there is very little change in the behavior up until the 9,000 cycle. After this point, a rapid onset of damage occurring over the next 1,000 cycles can be observed by the dramatic decrease in the torsional moment required to achieve the desired rotation.

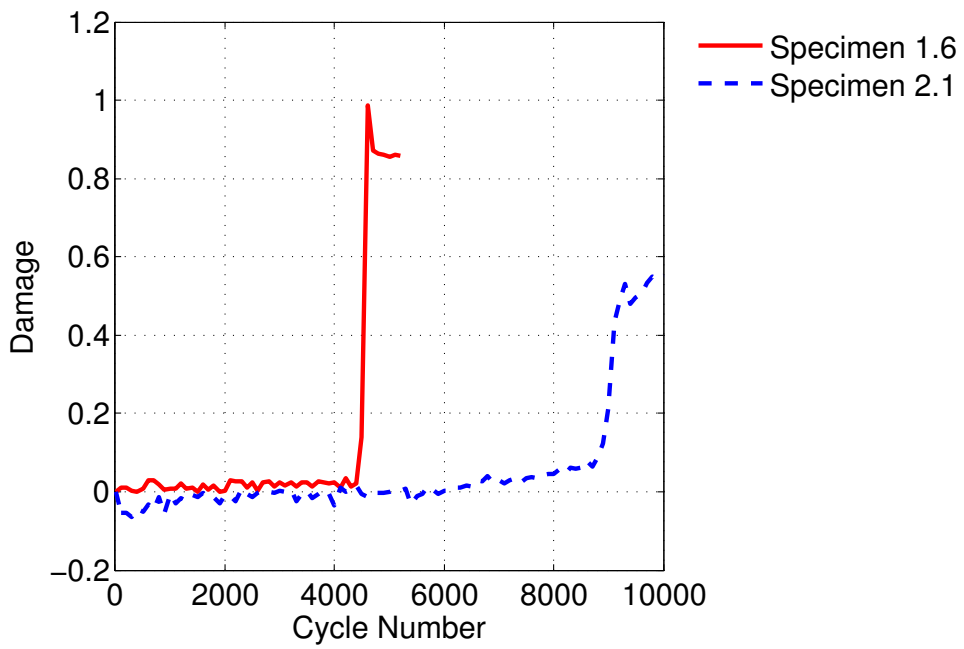

Figure 3.18: Torsional damage versus cycle number for a failed and unfailed specimen.

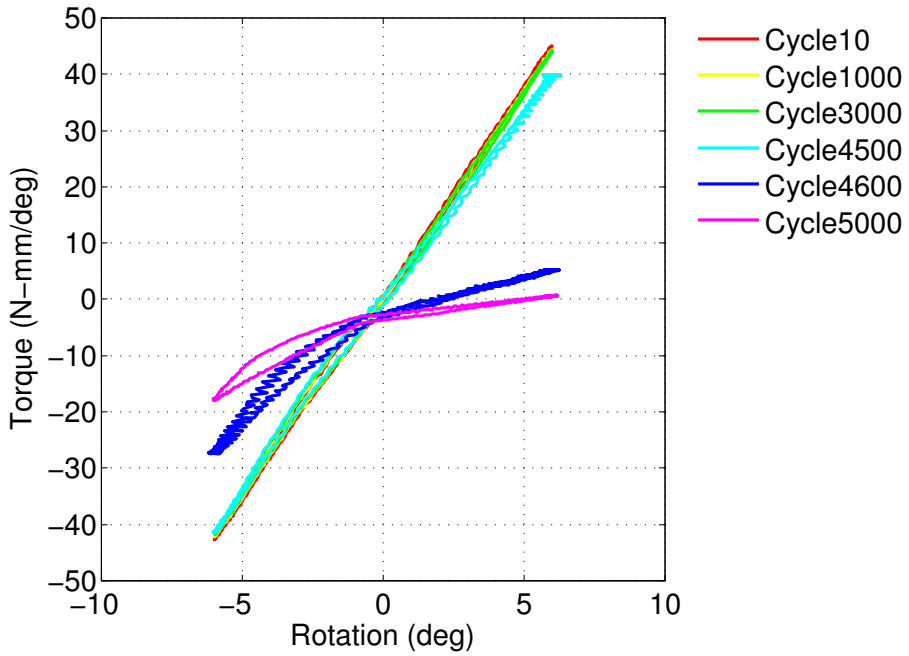

(a)

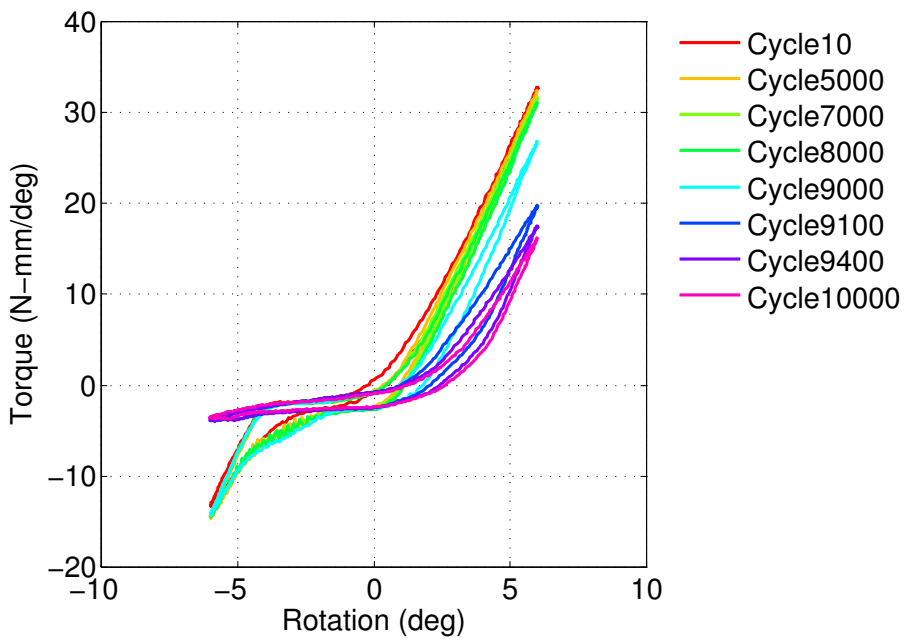

(b)

Figure 3.19: Torsional moment (N-mm/deg) versus rotation (deg) at varying cycles for a defect and treatment specimen. (a) Specimen 6.1. (b) Specimen 2.1. The higher slopes represent the earlier cycles, while the lower slopes represent later cycles.

The onset of damage is best illustrated by plotting the calculated construct damage versus number of cycles, as determined by the methods described in Section 3.6.4. We previously observed that the specimens actually undergo the phenomenon of hardening as a result of axial cyclic testing. Since many specimens failed, we predict that some damage must occur as a consequence of torsional loading. Figure 3.18 illustrates the calculated damage over the cyclic test period. It can be observed in Figure 3.18 that very little damage occurred up to the point of failure for the specimen represented by the solid line. After this point, the damage spontaneously approached a value of 1, indicating that complete damage has occurred. Similar behavior is observed for the specimen represented by the dashed line. However, it is evident that some damage has gradually accumulated up to the point of visible crack formation. Around 9,000 cycles a small crack formed in the proximal-posterior edge of the defect. This is illustrated by the sharp increase in damage around this point. Complete failure did not occur by 10,000 cycles. This is illustrated by the relatively high damage that has accumulated at the completion of the test.

The mean maximum damage value for the defect specimens was 66.5% (standard deviation: 40.3%; range: -5.4–98.8%). Among these specimens, one specimen actually hardened to a value of 5.4%. If the hardened specimen is excluded, the mean maximum damage was 76.8% (standard deviation: 30.1%; range: 11.1–98.78%). The mean maximum damage value for the treatment group was 34.2% (standard deviation: 43.6%; range: -6.5–99.6%). Among the treatment specimens, two specimens were observed to harden up to 1.7% and 6.5% (-1.7% and -6.5% damage, respectively). If these two specimens are excluded from the mean maximum damage, the treatment group achieved an mean maximum damage of 46.9% (standard deviation: 43.3%; range: 8.72–99.6%). It can be observed that there is a trend towards lower construct damage in the treatment group, however, the difference of means with and without the hardened specimens were not statistically different ($P > 0.05$). A number of the data sets exhibited clear damage behavior with easily determined

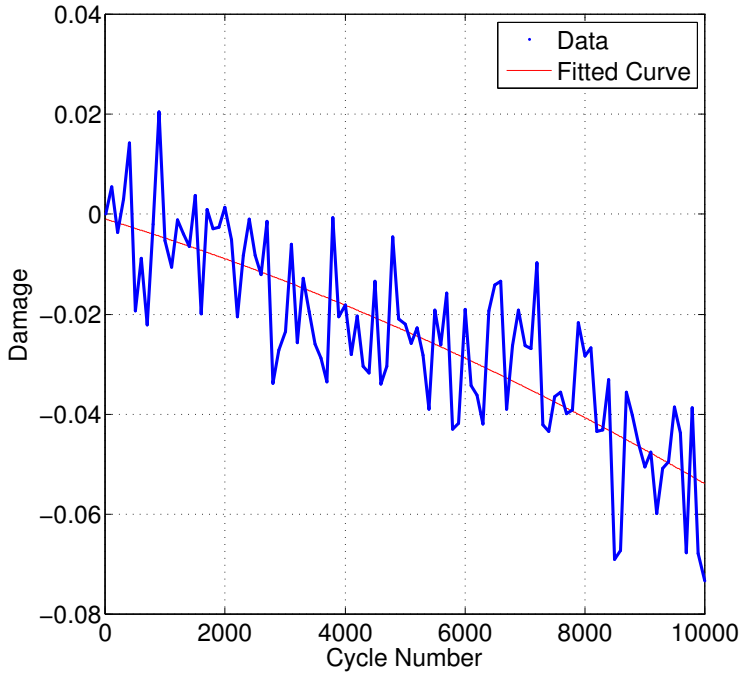

(a)

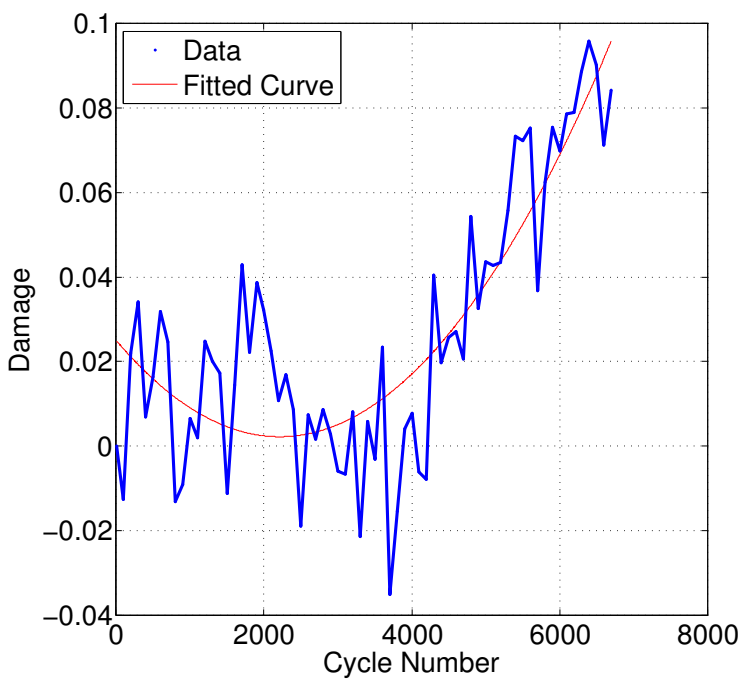

(b)

Figure 3.20: Torsional damage versus cycle number with second order fit for (a) hardened—Specimen 1.7 and (b) damaged—Specimen 2.3 specimens.

maximum damage values, such as those shown in Figure 3.18. Some of the data sets, however, were very noisy and much more difficult to interpret. A second order polynomial was used to fit the noisy data sets to elucidate a more clear behavioral trend. An example of the curve fitting is shown in Figure 3.20 for a hardened and damaged specimen.

3.8 Discussion

The results of the experimental work provide evidence that the introduction of the defect may comprise the structural stability of the femur in both axial and torsional loads. The quasi-static loading revealed that there is a trend towards a reduction in both axial and torsional stiffness, although these were generally not statistically different. Similarly, there was no statistically significant difference in ultimate torsional moment between the neat and defect groups, however, there was also a trend towards weakening in the defect group. There was good agreement on the slope of the load-displacement curves during the load-to-failure experiments for both the defect and the neat group. The ultimate torsional moment, however, has highly variable, and provided very little conclusive evidence that the defect has significant weakening effects.

The results of the fatigue analysis revealed no statistically significant differences for time of failure between groups in either axial compression or torsion. During the axial fatigue testing, it was observed that the constructs underwent hardening over the fatigue period. There is no evidence that the human femur undergoes this phenomenon in cadaveric form. Similarly, there is no evidence that this particular geometry contributes to construct hardening. Therefore, it is possible to conclude that the synthetic femurs themselves are undergoing hardening as a consequence of their material properties. Work hardening is the process of material strengthening

by plastic deformation. In this case, the synthetic femurs are hardening, likely due to the onset of plastic deformation. The cortical layer of the 4th generation composite femurs is made of glass-fiber reinforced epoxy resin. A number of materials studies have revealed that epoxy will undergo work hardening under certain strain conditions. [88–90] Tao et al. [88] concluded that the uni-axial fatigue behavior of epoxy is directly related to the strain-rate of loading. They found that at high strain-rates, the materials will soften over time. However, under low strain-rates, epoxy will undergo the phenomenon of hardening. Song et al. [90] and Jordan and Spowart [89] observed the same behavior for multi-phase particulate epoxy composites. The composite femurs in this study are loaded under a low strain-rate protocol, therefore, it is likely that epoxy hardening is occurring.

The results of the torsional fatigue analysis revealed the occurrence of true damage accumulation in all but three specimens. Among the three that exhibited hardening behavior, the maximum that occurred was only 6.5%. The hardening observed in axial compression far exceeded the hardening of the torsional experiments. Therefore, it is not possible to conclude that torsional hardening is a predicted mode of behavior. This observation of torsional damage accumulation is in agreement with the mode of failure (spiral fracture through the defect) observed in the failed specimens. Qualitative observations revealed large deformation in the proximal, posterior edge of the defects prior to crack initiation through this region. Overall, the torsional load was the primary initiator of crack formation and propagation.

Previous studies have reported the use of the fourth-generation composite femurs for fatigue analysis of orthopaedic constructs. Chong et al. reported far superior fracture toughness [65] and fatigue performance [72] of the fourth-generations femurs over the third-generation femurs. They observed better agreement in the measured actuator displacement in the axial fatigue analysis among specimens, however, there still was variation observed among select specimens. Similarly, the report was only

a comparison of the third-generation to the fourth-generation specimens. This does not provide adequate insight to the use of the fourth-generation specimens to compare groups. Our study reveled large variation and overlap of data that resulted in no statistical difference between groups. The lack of statistical significance may indicate that the groups are very similar, however, the large variation within groups did not facilitate gathering concrete conclusions. This may be due to the inadequacy in the fatigue performance of composite femurs for a comparison of two very similar groups, where the majority of the load is distributed through the native bone material. Recent studies have reported good results for fatigue analysis of simulated fractures with orthopaedic construct augmentation in fourth-generation composite femurs. [91–93] Because the femurs were augmented with large metal constructs, a significant portion of the load was likely distributed through the implant, thus reducing the load on the femur. This distribution of stress may permit more consistent fatigue behavior within each of the construct groups.

Although the results were highly variable, significant clinical conclusions can be drawn from both the isolated and combined loading results. The primary mode of failure under both loading conditions was either a vertical fracture through the femoral neck or a spiral fracture through the defect. Both fracture patterns are frequently observed in the clinic. The fracture through the defect propagated clockwise and proximally, initiating from the proximal-posterior edge of the defect. This revealed that large shear stresses were occurring due to the torsional loading. The shear causes large diagonal tension forces (pulling proximally and distally at an angle), resulting in an upward and posteriorly propagating fracture. This reveals that although the defect exists on the medial cortex, adequate tension resistance must be applied to the posterior cortex to prevent cracking (fracture). Due to complex neurovascular anatomy on the anterior and posterior aspects of the femur, tension resistance on these cortices must be applied through the medial and lateral aspects. In the load to failure analysis, it was observed that the crack would form and propagate

to the point of failure almost simultaneously. This brittle fracture occurs when the shear stresses (resulting in diagonal tension through the elements on the posterior cortex) exceeds the ultimate shear stresses of the material. In the fatigue analysis, it can observed that the crack formed and propagated slowly until complete failure occurred. During physiological loading (i.e., gait), compression, tension, and torsional are applied to the femur. The torsion introduces large tension forces in the bone, however, these are mitigated by the compression applied during weight-bearing. This results in reduced tension on the cortex, thus slowing crack growth. Without the ability to predict healing, it is difficult to make conclusions on the efficacy of this treatment method. A large locking plate would likely reduce the shear forces on the posterior cortex and prevent crack formation on the defect. This treatment, however, is large and invasive and may be reserved for more unstable fractures. Therefore, it is important to find a construct that will reduce these forces while reducing the cost and incision required for prophylactic stabilization. Future work may consider the locking equivalent of a one-third tubular plate with both fixed and variable angle screw trajectories.

The experimental work revealed that the defect acts as a stress concentration that increases the local stresses and strains, thus facilitating failure. The time to failure was not significantly altered by the addition of the plate, however, qualitatively, we see a trend towards longer time to failure. Based on the experimental analysis, the addition of the plate does not negatively nor positively affect the structural stability of the defect bone. Based on the results, immediate full weight-bearing may not be feasible until some bone regrowth has occurred. The effects of the defect and the addition of the plate will be further investigated in Chapter 4 using the finite element method.

Chapter 4

Numerical Methods

4.1 Introduction

The finite element method (FEM) was used to accomplish two main objectives: 1) To observe the stresses and strains in the system and explain phenomena observed in the experiments, and 2) to develop predictions for the consequences of a cortical window with an increasing diameter. The model was developed using a three-dimensional (3D) rendering of the femur, experimental fixture, and the implant that was modeled using the computer-aided drawing (CAD) software, SolidWorks (Dassault Systémes SolidWorks Corporation, Waltham, MA, USA). After the experimental conditions were fully rendered, the model was imported into the commercial FE software package, ANSYS Workbench (ANSYS, Inc., Canonsburg, PA, USA). Each of the model components was assigned their respective material properties, and the appropriate boundary conditions were applied to the system. The model was subjected to simulated loads representative of the experimental test conditions. The model was first validated to confirm its ability to accurately simulate the construct behavior. The model was then used to conduct a parametric analysis of the cortical defect diameter.

As described in Sections 2.3 and 2.6, a number of studies have sought to characterize the structural consequences of cortical defects experimentally and computationally. Most of the models that used a FE analysis utilized simplified models, such as cylinders to model the diaphysis, and few of these were experimentally validated. This study is the first to use a fully validated, full bone model to test varying sized defects in the distal femur. Additionally, this model provides insightful information regarding the proposed treatment method for a 15 mm distal metaphyseal defect.

4.2 Numerical Methods

4.2.1 Three-Dimensional Femur Model

The numerical component of this study utilizes the finite element (FE) method to analyze behavior of three-dimensional femur models representative of the groups tested in the experimental work. This study utilizes the "standardized femur" model developed for the third and fourth generation composite femurs by Papini et al. (described in Section 2.6). [84] The surface geometry and cortical thickness match the fourth generation composite bones used in this study. The cancellous region is modeled as an isolated region that completely fills the cortical shell.

The 3D "standardized femur" model was obtained from the Biomechanics European Laboratory (BEL) Repository from biomedtown.org. [83] The cancellous and the cortical regions, shown in Figure 4.1, were assembled to form the full femur.

A medullary canal with a diameter of 13-mm (according to the dimensions provided by the manufacturer [64]) was created in the bone, originating from the proximal metaphysis and ending below the condyles. This left a hole in the distal end of the specimen identical to the physical specimens. The experimental loading fixture was modeled using computer aided drawing (CAD) software. The acetabulum was

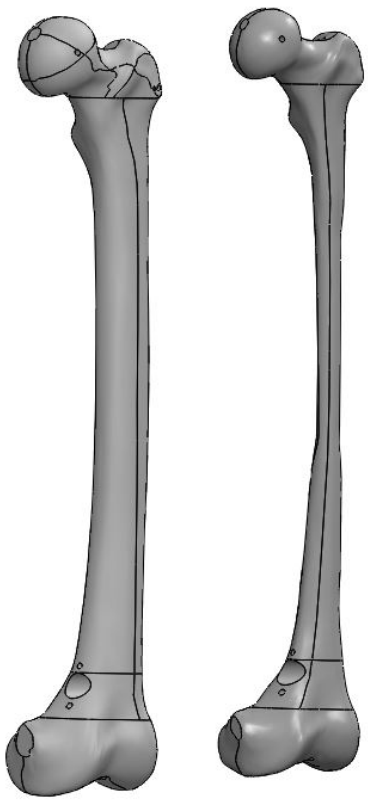

Figure 4.1: Cortical (left) and cancellous (right) bone models with defect in place.

modeled using the original CAD drawings. [94] The stainless steel pin was modeled as a long cylinder with a diameter of 4 mm and a length of 200 mm—for simplicity the threaded tip was excluded from the model. The distal cast was modeled as a rectangular block that encapsulated the region 5 mm below the condyles up the center of the epicondyles. A boolean subtraction was used to remove the cortical geometry from the block to create the cast of the distal region. The defect was created 55 mm from distal articular surface with a diameter of 15 mm. Due to proprietary regulations, the implant was reverse engineered and modeled after plate contouring occurred. The plate was modeled as a 1 mm thick rectangular protrusion along the contour of the cortex directly over the cortical window. A boolean subtraction was used to remove geometry of the bone from the plate, thus allowing the plate to per-

fectly contour with the bone, as was done experimentally. Three model assemblies were developed: 1) The intact model, 2) the defect model with no treatment, and 3) the defect model with the 1/3 tubular plate. Figure 4.2 shows the complete assembly of the defect specimen with the implant in place.

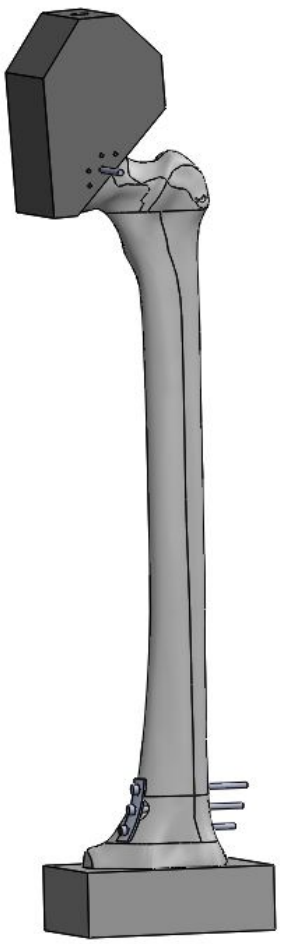

Figure 4.2: Complete experimental fixture model including defect, plate, and screws.

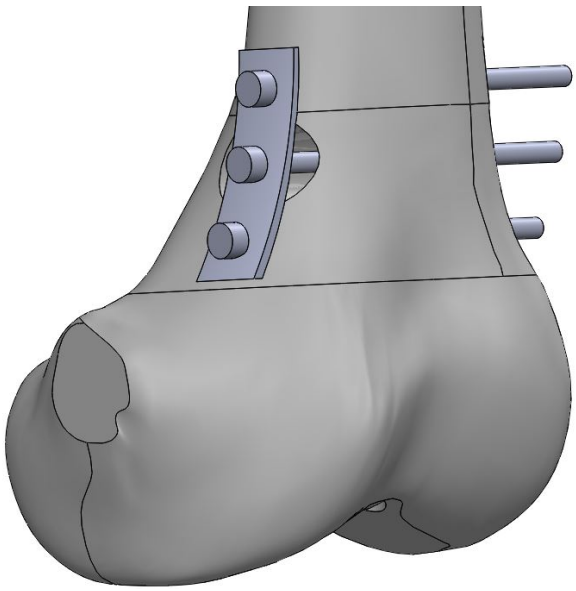

Figure 4.3: Distal femur with 15mm cortical defect and 1/3 tubular plate model.

4.2.2 Boundary Conditions and Material Assignment

The femur and loading fixture were modeled to replicate the experimental loading conditions as closely as possible. The femur was oriented with the anatomical axis 6° off the mechanical axis and the femoral head 15° in anteversion, as described in Section 3.3. The acetabulum was oriented with the loading axis directly along the mechanical axis of the femur. The pin was placed concentrically through the hole in the acetabulum, directly into the femoral head, and out of opposite hole in the acetabulum. The bottom surface of the cast material was fixed to replicate the cast within the vice.

The cortical and cancellous regions of the femur were assigned the material properties provided by the manufacturer. [64]. The acetabulum was assigned the material properties for aluminum alloy and the pin was assigned stainless steel properties. Both were found in the FE package's material library. Finally, the cast material was assigned properties based on the manufacturer's technical specifications. [95] The

material properties used for the system are summarized in Table 4.1.

Table 4.1: Summary of material property assignments in FE model. ρ = Density; $E_{Tensile}$ = Modulus in tension; $E_{Compress}$ = Modulus in compression; "S" and "C" represent solid and cellular, respectively. "—" = Information not used or not provided by manufacturer.

Property		Cortical	Cancellous	Stainless	Aluminum	PMMA
ρ	(kg/m^3)	1640	S: 270 C: 320	7750	2770	—
$E_{Tensile}$	(GPa)	16	—	160	71	0.3
$E_{Compress}$	(GPa)	16.7	S: .155 C: .137	—	—	—
$\sigma_{Tensile}$	(MPa)	106	—	207	280	21
$\sigma_{Compress}$	(MPa)	157	S: 6.4 C: 5.4	207	280	25

The cancellous and cortical regions were bonded together with asymmetric contact and solved using the multi-point constraint (MPC) formulation. The remainder of the contact interfaces were governed by symmetric frictional contact and solved using an augmented Lagrange formulation. The frictional contacts were based on published frictional coefficients between the two materials in contact. Small adjustments were made to the coefficients to facilitate convergence and model accuracy. The coefficient of friction between the distal cast and the epoxy cortex in the model was much higher than published data for contact between the two materials. In the

experimental fixture, the distal cast was compressed around the distal region of the femur with a vice. However, because the cast only potted the region below middle of the epicondyles, small motions were likely to occur as a consequence of the bending moment applied during compression. Therefore, bonded contact was not an appropriate contact assignment. Thus, a large coefficient of friction was used to make the contact more rigid, while still permitting some motion between the two surfaces. A summary of the contacts and the coefficients of friction used are listed in Table 4.2.

Table 4.2: Summary of FE contacts for neat, defect, and plate models.

Contact	**Target**	**Type**	**Friction Coefficient**	**Formulation**
Cancellous	Cortical	Bonded	—	Multi-point constraint
Cortical	Acetabulum	Frictional	0.05	Augmented Lagrange
Distal Cast	Cortical		0.8	
Cortical	Pin		0.2	
Cancellous	Pin		0.2	
Acetabulum	Pin		0.05	
Cortical	Screw	Frictional	0.3	Augmented Lagrange
Cancellous	Screw		0.2	
Cortical	Plate		0.3	
Plate	Screw		0.3	

4.2.3 Finite Element Mesh

The FE mesh is the result of discretizing the model into finite elements. The initial FE mesh was automatically generated using 10 noded tetrahedral structural solid

elements, a fine relevance center with default element size, and medium smoothing. Additional mesh refinement using 20 noded hexahedral elements was applied to the contact interfaces. The mesh and model quality were assessed using the mesh metrics and the Newton-Raphson residual force results. The mesh metric results provide information regarding the overall distribution of element quality. The Newton-Raphson residual force results reveal areas of force–reaction force imbalance.

4.2.4 Loading Conditions

The finite element loading conditions were simulated to replicate the experimental loads. The preliminary stiffness results were evaluated under quasi-static loading, with axial and torsional stiffnesses evaluated independently. For axial compression, the top surface of the acetabulum was displaced up to 2 mm in a total of 8 steps along the mechanical axis of the femur. In torsion, the acetabulum was rotated about the mechanical axis up to $\pm 1.5^{\circ}$ in 8 steps for each direction. The force and moment reaction forces were determined at the bottom surface of the distal cast to replicate the location of the axial-torsional load cell used in the experiments.

4.2.5 Parameterization of Defect Size

The quasi-static loading models were used to develop predictions for the structural consequences of larger defects in axial and torsional loads. The FE simulation was conducted with no defect, and with defects ranging from 15 to 40 mm in diameter. The specimens were loaded under the aforementioned loading conditions. Normal stresses and strains, shear stresses, overall deformation, reaction force at the fixed surface, and the reaction moment at the fixed surface were collected for analysis.

4.3 Numerical Results

4.3.1 Model Validation

The final mesh of the neat specimens consisted of 9,854 element. The final mesh for the femurs with the defect and the plate resulted in a final element count of 12,458. The final mesh metrics revealed a good distribution of quality 10-noded tetahedral and 20-noded hexahedral elements. Figure 4.4 shows the mesh refinement at the pin/acetabulum and the pin/bone interfaces.

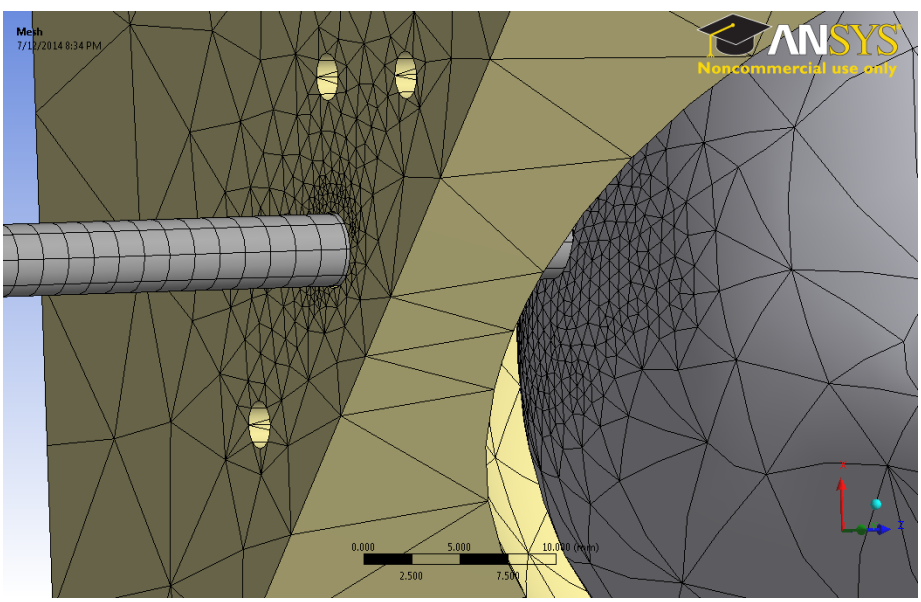

Figure 4.4: Mesh refinement at the pin/acetabulum and the pin/bone interfaces.

This mesh refinement was required in the plate specimens, however additional refinement was required around the defect site and on the plate. Figure 4.5 shows the refinement on the plate/bone interfaces.

The results of the intact model correlated well with the experimental results. The results of the neat model validation are shown in Figures 4.6a, 4.7a, and 4.8a for axial compression, external torsion, and internal torsion, respectively. The femurs

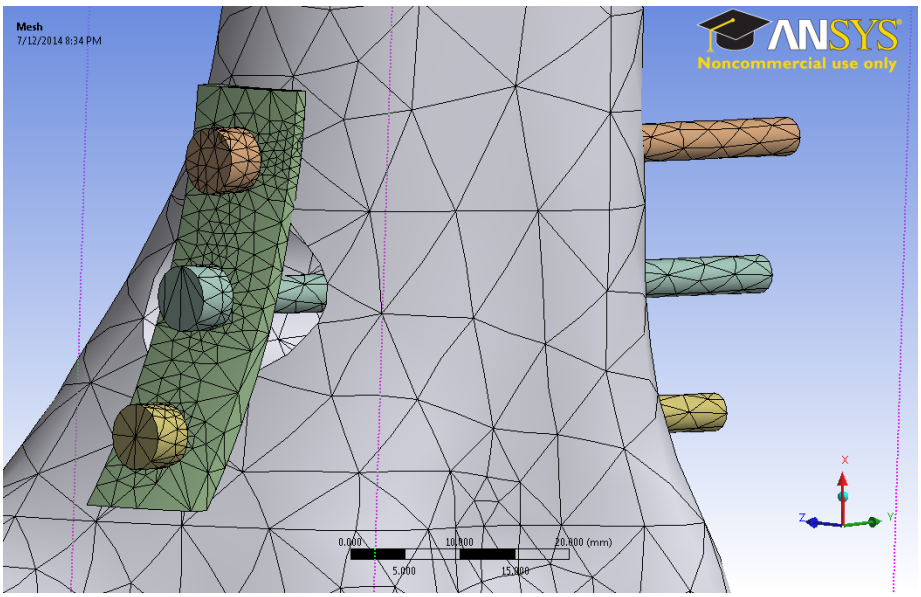

Figure 4.5: Mesh refinement at the pin/acetabulum and the pin/bone interfaces.

were subjected to the 15 mm defect without any further changes to the model, such as boundary conditions and material properties. The 15 mm defect model predicted results within the the experimental COVs under axial and torsional loads. The results of the 15 mm defect model validation are shown in Figures 4.6b, 4.7b, and 4.8b for axial compression, external torsion, and internal torsion, respectively.

The highest normal stresses and strains and shear stresses were observed at both the bone/pin and acetabular/pin interfaces. Similarly, the highest deformation was observed at the pin edges due to a large bending moment within the pins. In axial compression, it was observed that the pin would cut through the cancellous region upon reaching the maximum displacement.

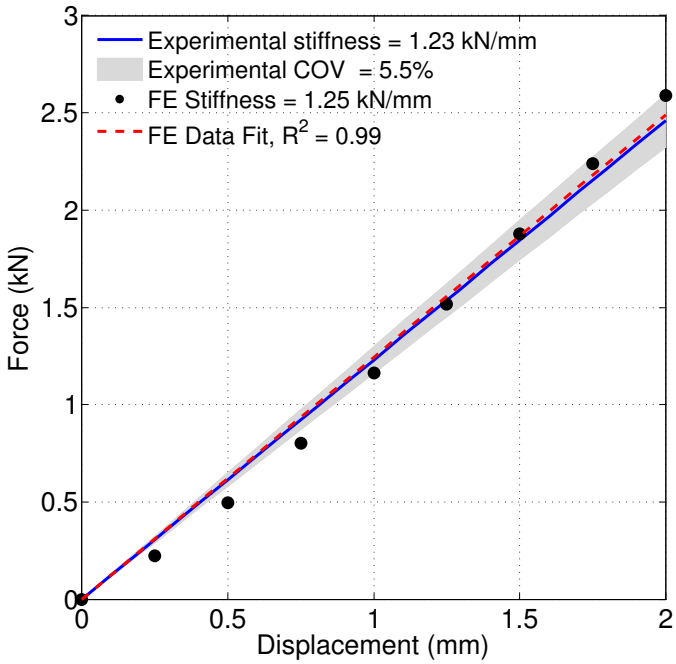

(a)

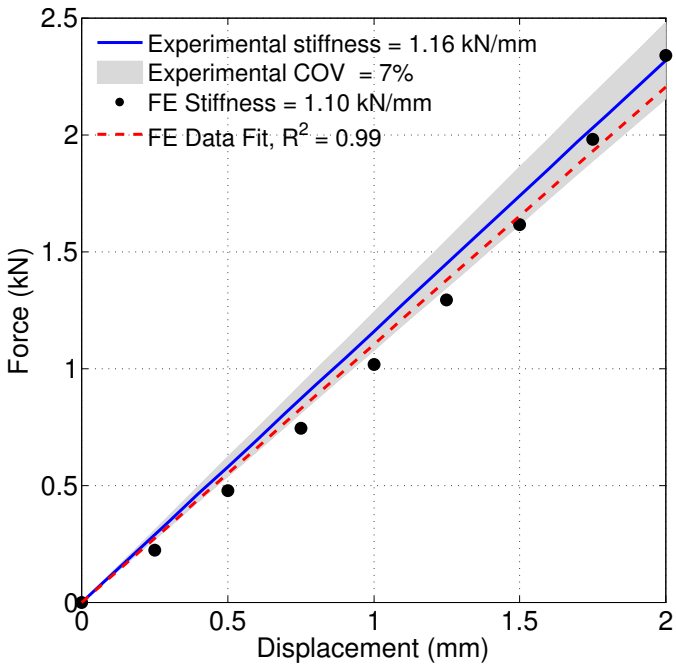

(b)

Figure 4.6: Finite element model validation under axial loading. (a) Neat (b) 15 mm Defect.

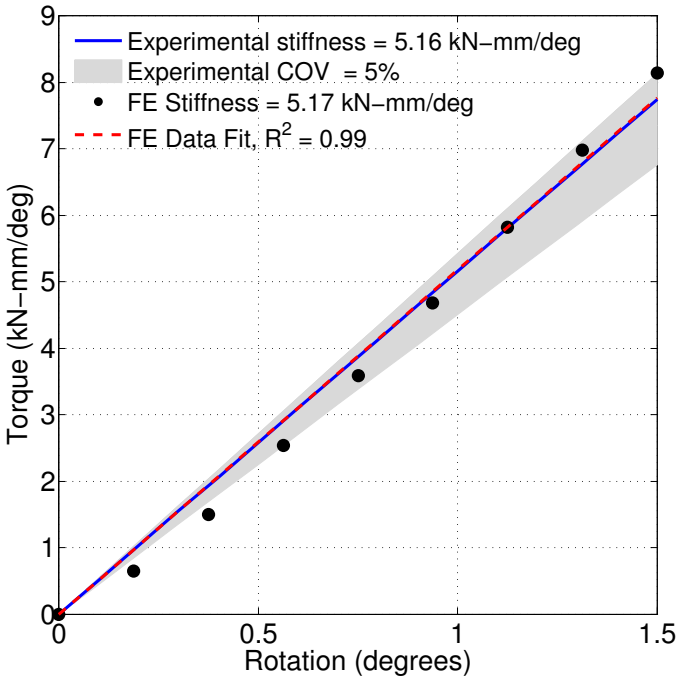

(a)

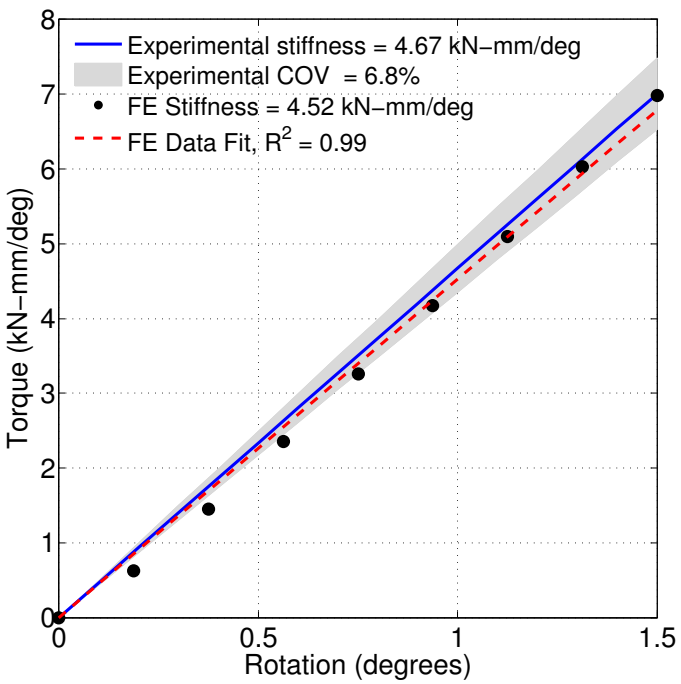

(b)

Figure 4.7: Finite element model validation under external rotation. (a) Neat (b) 15 mm Defect.

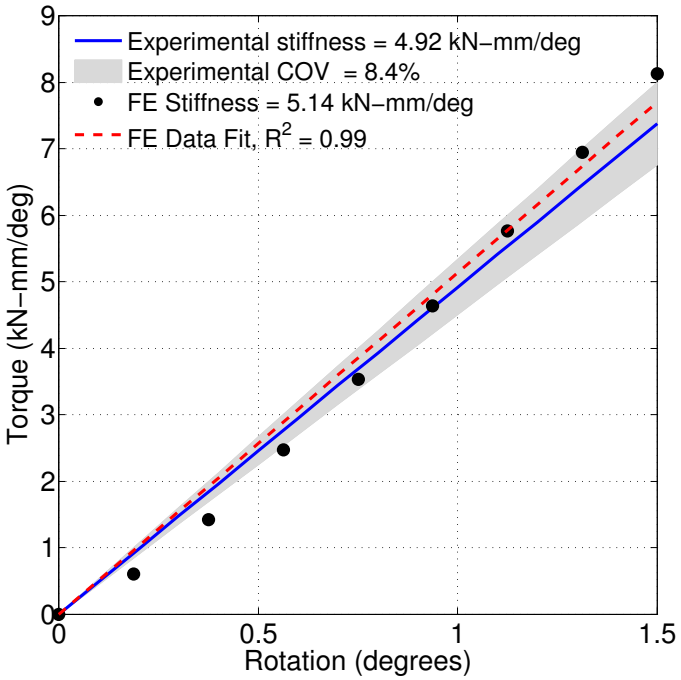

(a)

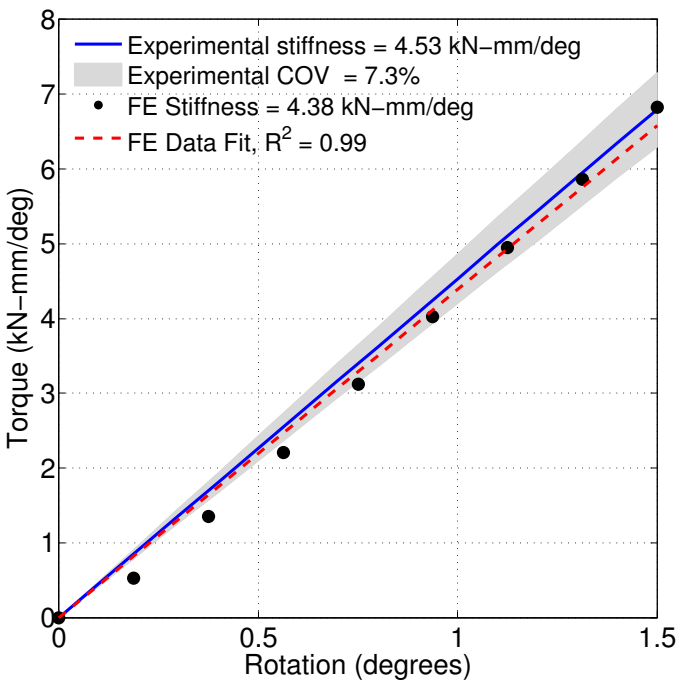

(b)

Figure 4.8: Finite element model validation under internal rotation. (a) Neat (b) 15 mm Defect.

4.3.2 Parameterization of Defect Size

The results of the defect size parameterization revealed a progressive decrease in axial stiffness of 27% for up to a 40 mm diameter defect. Similarly, there was also a 22% decrease in external torsional stiffness and 24% in internal torsional stiffness for a 40 mm diameter defect. These results are shown in Figure 4.9

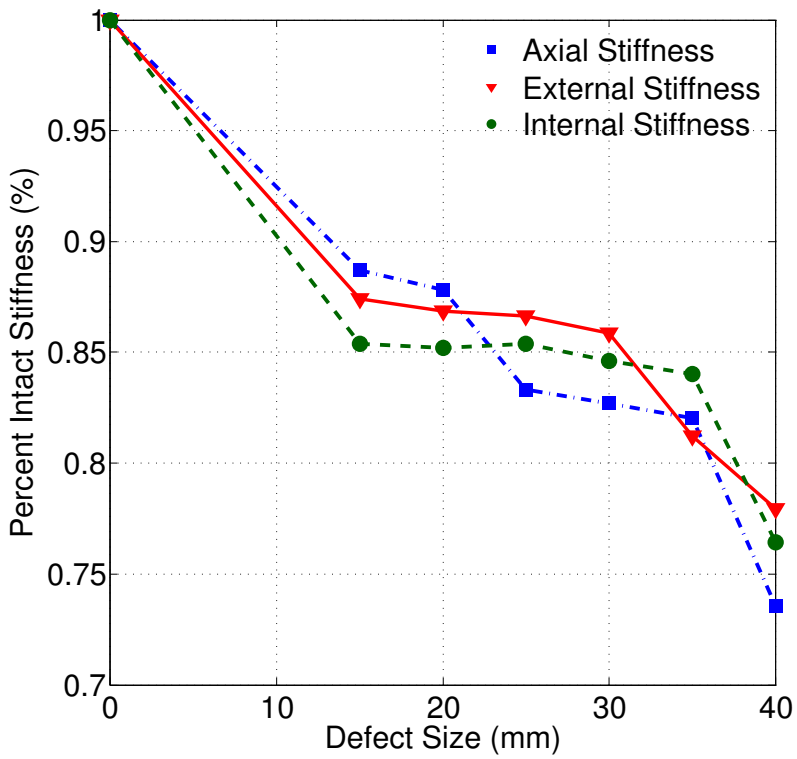

Figure 4.9: Percent reduction in stiffness versus defect size.

The consequences of varying sized defects were investigated under combined axial/torsional loading. The stiffness of the 15mm defect specimens was used to validate the accuracy of the model. The model predicted an axial stiffness of 1.38 kN/mm. The experiments revealed a stiffness of 1.27 N/mm with a COV of 33.6%. In torsion, the model was yielded a stiffness of 6.43 N-mm/deg in the +6° while the experiments revealed a stiffness of 6.67 N-mm/deg (COV = 7.25%). In the -6° direction,

the model yielded a stiffness of 6.17 N-mm/deg while the experiments revealed a stiffness of 5.88 N-mm/deg (COV = 33.8%). All the predicted values were within the COVs of the experimental results. The combined axial torsional results revealed a more drastic reduction in stiffness as a consequence of the defect. Increasing the defect size resulted in a linear decrease in stiffness in axial compression, internal rotation, and external rotation. The combined imposed a larger stress due to higher rotation and combined with axial compression. At a diameter of 45 mm, there was a loss in stiffness of approximately 45–50% in all three loading modes.

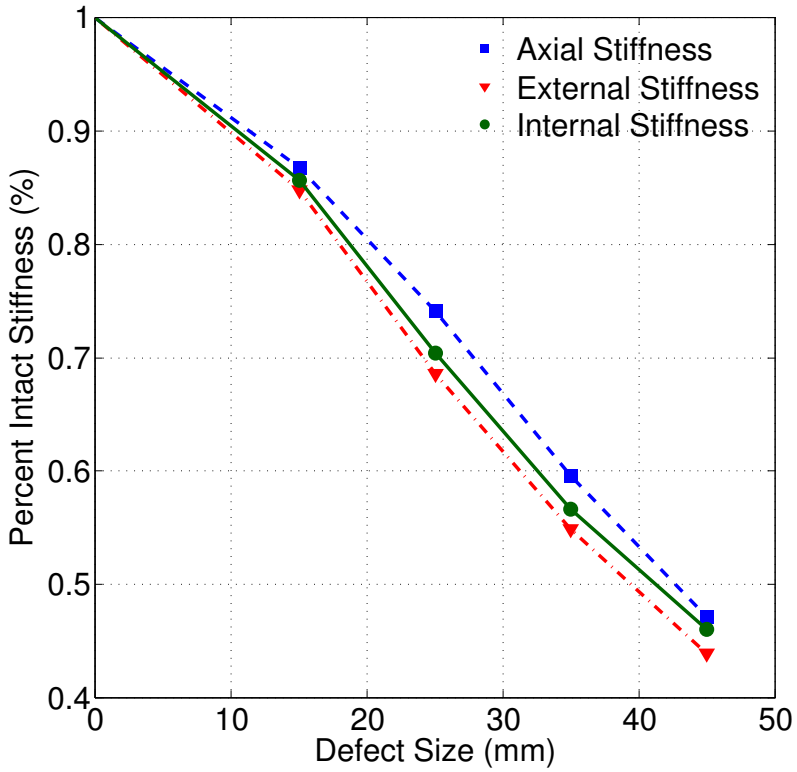

Figure 4.10: Percent reduction in stiffness versus defect size.

4.3.3 Plate Model

Next, the significance of adding a plate to the defect location was investigated using the fully assembled FE model. The specimens with the defect and plate were experimentally investigated under quasi-static loads. However, using the fully validated model, the femur/plate construct was tested in the FE simulations. The observed axial stiffness under combined axial/torsional loading was 1.07 kN/mm. The finite element model revealed

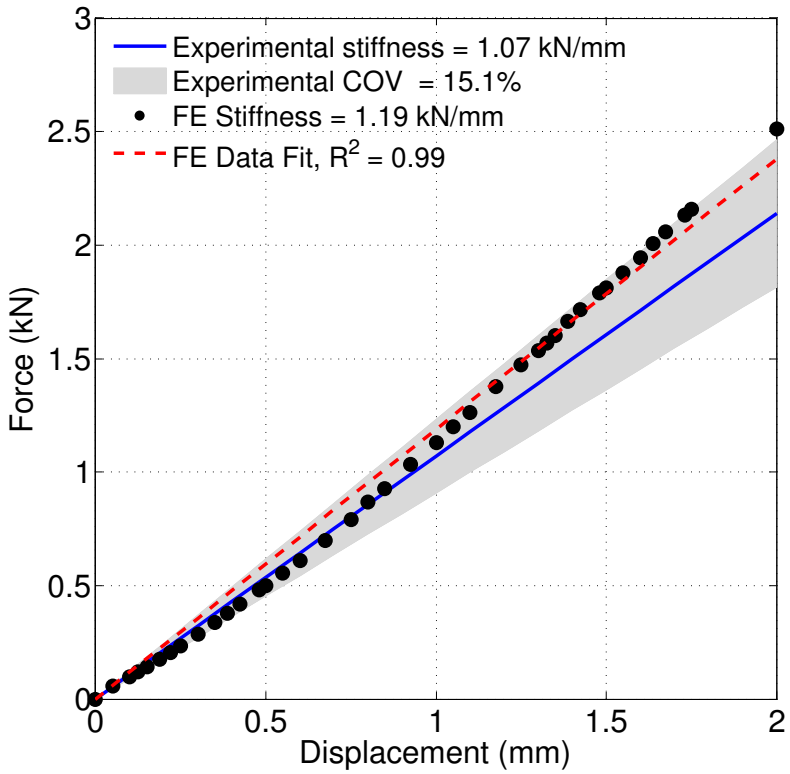

Figure 4.11: Results of FE plate model under axial compression.

an axial stiffness of 1.21 kN/mm, which was still within the experimental COV. Slight over-estimations of assembly stiffness of the FE model were observed when compared with experimental observations. This might be attributed to linear elastic assumptions of the system and to negligence of minor frictional effects between

components of the assembly. In the model, the plate restores the axial stiffness of the femur to within 3% of the fully intact stiffness. The torsional models revealed stiffnesses of 6.77 kN-mm/deg in external rotation and 6.07 kN-mm/deg in internal rotation. Both of these were within the experimental COV. The internal FE results varied by 8%, however, because of such a high experimental COV, the results fell within the range for observed experimental values. The results of the bone/plate construct FE model validation are shown in Figures 4.11, 4.12, and 4.13. The highest stresses for the plate model were also observed at the pin-bone interfaces, however, high stresses were observed at the screws. Figure 4.14 shows normal stresses of 10–12 MPa at the screw/bone interface. Similarly, Figure 4.15 shows shear stresses of 5–6 MPa at the bone/screw interface.

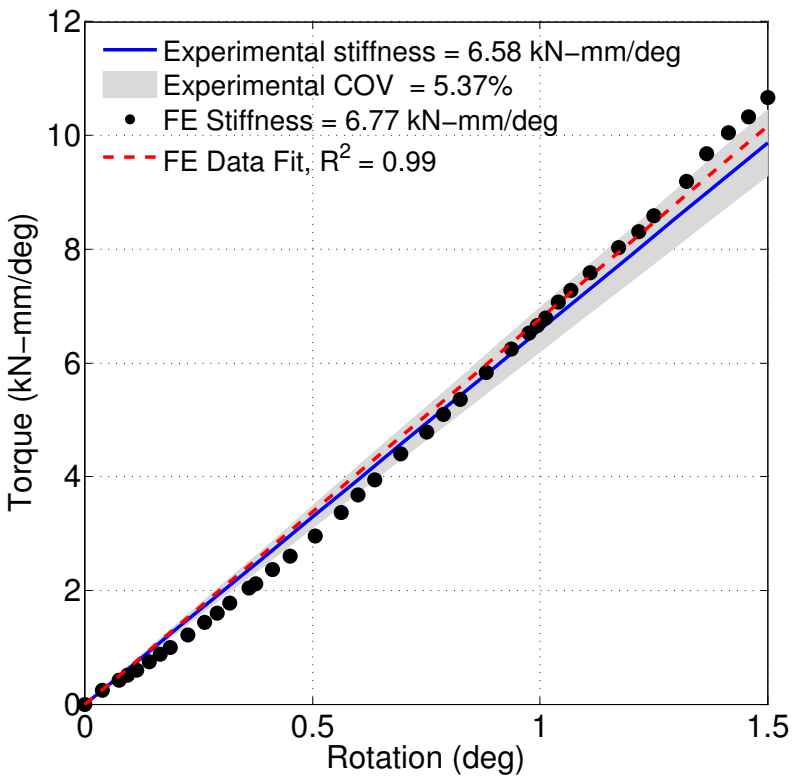

Figure 4.12: Results of FE Plate model under external torsional loading.

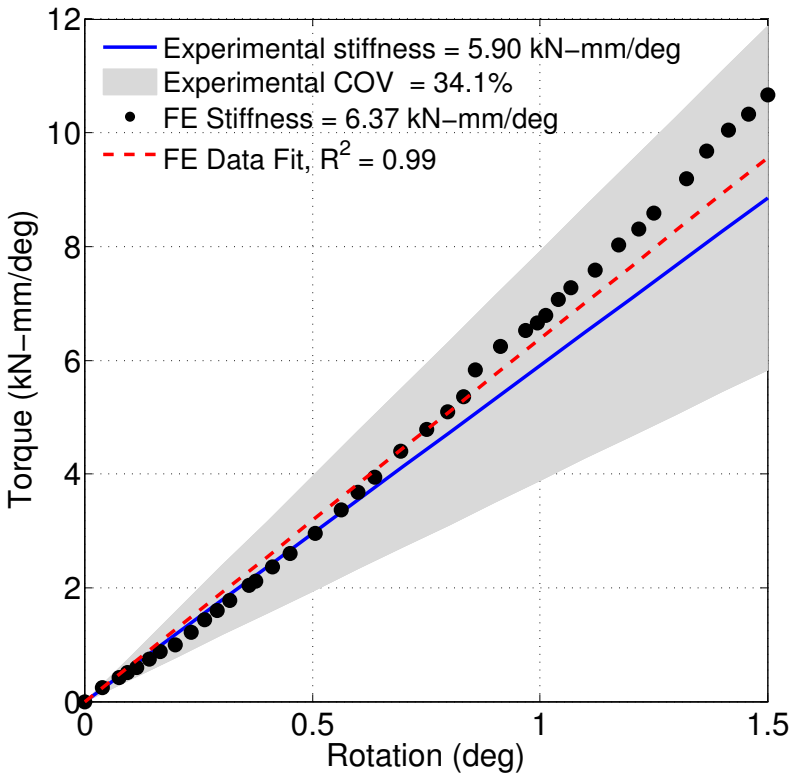

Figure 4.13: Results of FE Plate model under internal torsional loading.

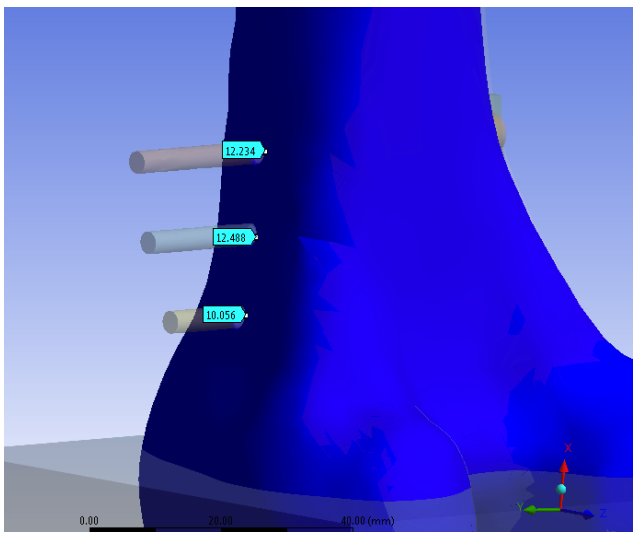

Figure 4.14: Normal stresses at screw/bone interface.

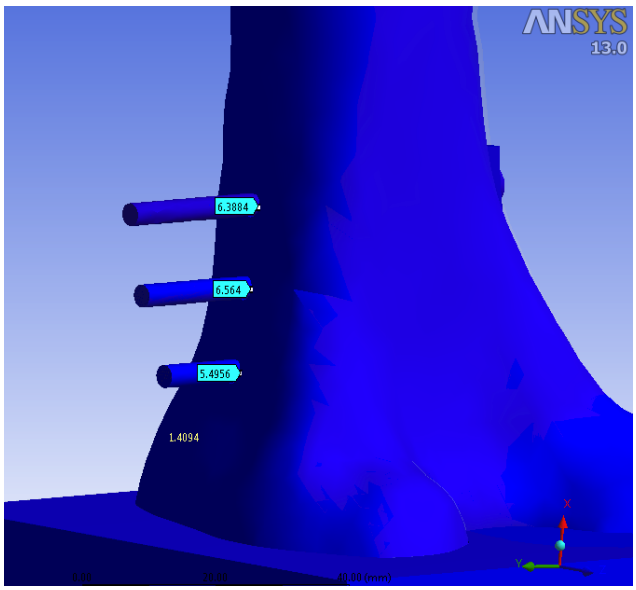

Figure 4.15: Shear stresses at screw/bone interface.

4.4 Discussion

The results of the quasi-static isolated axial and torsional models reveal that the defect size gradually decreased the axial and torsional stiffnesses. At a size of 40 mm in diameter, there was approximately a 25% decrease in stiffness in all modes of loading. Under combined axial/torsional loading, the defect caused a much greater reduction in stiffness. A defect with a diameter of 40 mm resulted in a 45% reduction in stiffness in all three loading modes. This is likely to the large torsional rotation ($\pm 6^{\circ}$) and high stresses at the defect edges. The combination of axial and torsional loading creates a combination of compression and tension, resulting in higher shear and normal stresses around the defect site. This analysis considered the effects of increasing the defect size under isolated quasi-static axial and torsional loads. Under isolated modes, the defect did not play a significant role in weakening the specimens ($\approx 25\%$). This study revealed that when the isolated loads imposed on the

femur are very low, the defect does not result in a significant reduction in individual stiffness. While these loads are within physiologically relevant loads, they generally do not occur under isolated conditions. Therefore, the combined axial/torsional loading provides more insightful results regarding the consequences of increasing sized defects. This study was the first to consider the effect of these defects under quasi-static aixal and torsional loads and conbined axial/torsional loading.

The addition of the plate restored the stiffnesses back to slightly greater than the original values. The addition of the plate revealed stress concentrations at each of the screws, however, the stresses at the pin were still much higher. The shear stresses at the screw/bone interface are of greatest concern when considering the risk of periprosthetic fracture. Maximum shear stresses of 5–6 MPa were at the bone/screw interface. According to Zdero et al. [96], shear stresses ranging from 24–35 MPa were observed at the bone/screw interface in 3rd generation composite femurs. Previous studies of stresses at bone/screw interfaces in cadaveric femurs reported maximum shear stress of 24–39 MPa. [97–99]. The values observed in this study were approximately 20–25% of the shear stresses observed at failure. Similarly, these stresses may be slightly higher than the actual values present. As observed before, the negligence or over-approximation of frictional contact between components of the assembly resulted in higher values of predicted stiffness. High frictional values at the screw/bone interface will certainly result in respectively higher shear stresses. Nonetheless, the shear stress are well below the reported values, and thus it unlikely that failure will occur through the bone/screw interface. This study reveals that the plate may be a feasible treatment option that restores the stiffness of the bone while not imposing high stress concentrations that are likely to result in fracture.

Previous studies have revealed a far greater reduction in stiffness under much larger isolated loads. Fidler et al. [17] revelaed that a hole encompassing 40% of the cortex resulted in a loss of strength of 70%. Similarly, Edgerton et al. found

a 60% reduction in torsional strength for the same sized defect. [23] McBroom et al. [22] found that a 50% defect results in a loss of torsional strength of 87%. These studies have all considered the effects of the defect under load-to-failure conditions. These will undoubtedly reveal a significantly greater loss in strength than quasi-static isolated stiffness testing. The results of the combined/axial torsional loading revealed a much greater loss in stiffness, however, it was still lower than values observed under load-to-failure conditions. This model did not investigate load-to-failure behavior. It will be useful to consider the defect under larger torsional moments to see the effects of the defect size. Finally, a Monte-Carlo simulation can be used to determine the risk of fracture at varying defect sizes and bone densities. This technique has been used by previous researchers to provide highly insightful results. [100]

Chapter 5

Conclusions

Benign cysts are a common occurrence in long bones, and are of concern in load-bearing bones, such as the tibia and femur. Numerous post-curettage management options have been described in the literature, which generally include filling the defect with either synthetic or biological materials. [29–38, 44, 45] These studies have reported successful healing of the defect, however, complications, such as infectious disease transmission from allogenic bone [30, 33], thermal injury from exothermic polymer reactions [39–41], and a robust inflammatory response to synthetic materials [46, 47] have all been reported. In reponse to these concerns, a number of studies reported successful healing of benign cortical defects in long bones with no augmentation after curettage. [49–51]. The additional concern associated with leaving the defect unfilled—or filled with structurally insignificant materials, such as grafts or synthetic bone substitutes—is the lack of structural support to the defect site. The risk of fracture increases as the defect size increases, especially for defects over 5 cm in diameter. [49] Therefore, it is advantageous to investigate a treatment option that adds structural support to the defect site and permits the use of osteoconductive and -inductive materials within the bone cavity. In combination, this may provide a faster time to healing with a reduced risk of post-operative fracture through the

defect site than currently employed method. The treatment of these defects with a 1/3 tubular plate was proposed to accomplish the aforementioned objectives.

The purpose of this thesis was threefold: First, a quasi-static experimental comparison of intact and cortical defect specimens was conducted to determine the structural consequences incurred by the introduction of a 15 mm cortical defect. Second, an experimental fatigue analysis was employed to further analyze the behavior of the defect specimens, and to determine the structural stiffness regained by the addition of a 1/3 tubular plate. Third, a numerical approach was used to consider the structural consequences of varying sized defects under quasi-static axial and torsional loads, combined axial/torsional loading, and to further analyze the results of adding the plate to the defect specimens.

The quasi-static axial and torsional loading revealed that the introduction of the 15 mm cortical defect does not result in a statistically significant reduction in stiffness in most loading modes. In axial compression, the defect resulted in a 6% loss in stiffness. In torsional loading there was an 8% loss in stiffness in external rotation, and a 10% loss in stiffness in internal rotation—only the reduction in stiffness in the internal direction was statistically significant. The use of the composite specimens resulted in good correlation among specimens within groups. The highest COV was 7% in axial loading and 8% in torsional loading. There was a trend towards higher variation among specimens under torsional loading. No plastic deformation was observed in any of the specimens. The load-to-failure analysis did not reveal a statistically significant difference between the neat and treatment groups. The neat group had an average ultimate torsional moment of 67.8 N-mm/deg (COV = 40.6%) while the defect group had an ultimate torsional moment of 56.0 N-mm/deg (COV = 23.9%).

Next, the addition of the plate was investigated under combined axial/torsional cyclic loading. No statistically significant difference was observed for number of

cycles to failure or for construct stiffnesses. However, there was a trend in the tests for the plate specimens to have higher stiffnesses and a longer time to failure. Among the failed specimens, cracks generally propagated from the proximal-posterior edge of the defect, resulting in clockwise rotating spiral fracture. The failed specimens exibited rapid failure upon the onset of cracking. The damage analysis revealed that many of the specimens underwent hardening in axial compression and damage under torsional loading. The onset of hardening was associated with material itself and not related the construct behavior. Epoxy has been shown to harden under low, repetitive strain-rates, and thus it is likely that the bones used in this study were following this behavior.

Both the isolated and combined loading experiments resulted in failure through the femoral neck or through the defect. This spiral fracture through the defect is associated with high shear stresses that results in large tension forces on the posterior cortex. Unfortunately, it is not clinically feasible to apply a tension-reducing construct directly to the posterior or anterior aspects of the femur. Therefore, it is important use a construct that will reduce the tension, yet allows enough load through the bone to promote new bone growth. The locking version of a one-third tubular plate may provide adequate tension reduction to prevent crack propagation on the posterior cortex of the bone.

The numerical analysis using the finite element method revealed that under quasi-static isolated loads, the defect gradually decreases the stiffness to 25% of the initial stiffness for a 45 mm ($\approx$ 45% cortex) diameter cortical window. Because the femur is not generally loaded under low, isolated quasi-static loads or isolated load-to-failure conditions, the axial/torsional behavior may provide the most insightful results. The combined axial/torsional results revealed that a 45 mm cortical window results in a 45% loss in stiffness. This is a far greater reduction in stiffness than observed under isolated quasi-static stiffness testing, and may be grounds for prophylactic

intervention. The FE model revealed that the plate restores the stiffness of the bone to approximately the stiffness of the intact state. No significant stress concentrations were observed at the screw holes that may result in high risk of fracture. Therefore, the use a 1/3 tubular plate may be a feasible option for structural support of a 15 mm cortical defect in the distal femur.

This study had limitations that may be addressed in future studies. First, the use of synthetic bones is a useful way to compare groups, however, they may not accurately represent the bones fracture and damage behavior. Similarly, because most of the load was carried through the femur, the behavior was largely governed by the behavior of the epoxy. It was observed that the epoxy material underwent hardening under repetitive load conditions when damage would be expected. It is predicted that hardening would not be observed in natural bone. The advantage of using synthetic bones was the ability to develop a validated FE model using the experimental data. This, however, only considers uniform material properties throughout the bone. Natural bone is highly heterogenous in material properties, and thus a CT based 3D model of cadaveric bones may provide more accurate results. The use of cadaveric specimens would likely yield more physiologically accurate results in the experiments. These cadaveric bones could be imaged using CT, then reconstructed with varying material property assignment throughout the volume of the bone based on a calibrated bone density measurements. This would facilitate the development of a higher quality mesh based on the CT reconstruction of the cadaveric bones. Using this method, FE models could be developed for each cadaveric specimen used, thus permitting the use of greater statistical tools for comparison of results. Furthermore, a FE model that predicts healing may provide better results when considering the efficacy of treatment options over a healing period.

Future work will consider varying defect sizes experimentally in cadaveric specimens under combined axial/torsional loading. Furthermore, specimen specific FE

models will be developed to create a sample group for computational analysis. Based on these results, a locking equivalent of a one-third tubular plate may provide the stability requirements for prophylactically stabilizing a small cortical defect on the distal femur. These plates, with both fixed and variable-angle screw trajectories, will be investigated in future work.

Appendices

Appendix A

Axial Load Versus Displacement Plots for Cycle 10

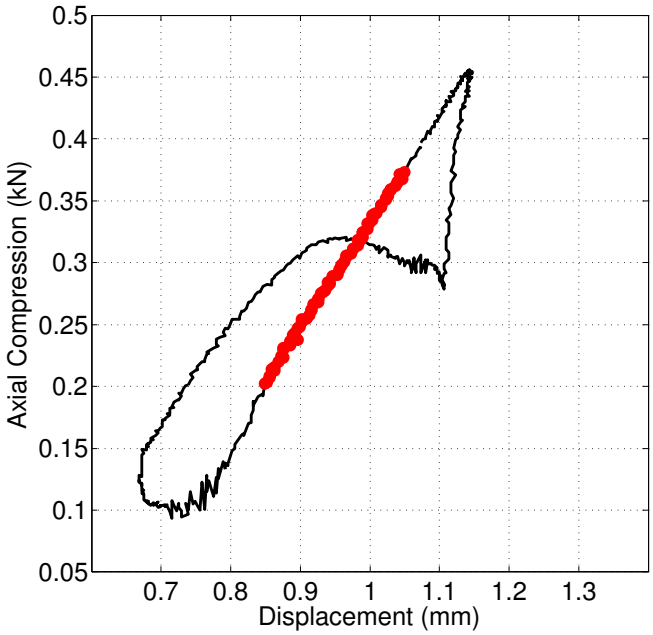

Figure A.1: Axial force versus displacement at the 10th cycle for specimen 1.1.

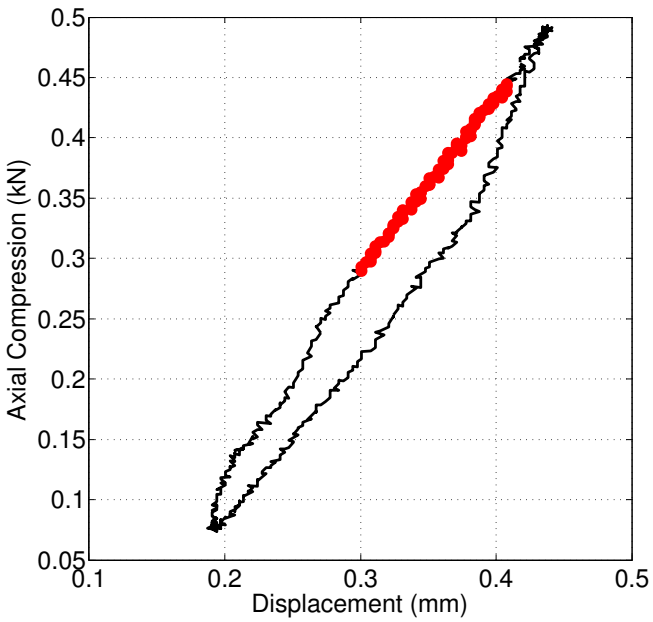

Figure A.2: Axial force versus displacement at the 10th cycle for specimen 1.2.

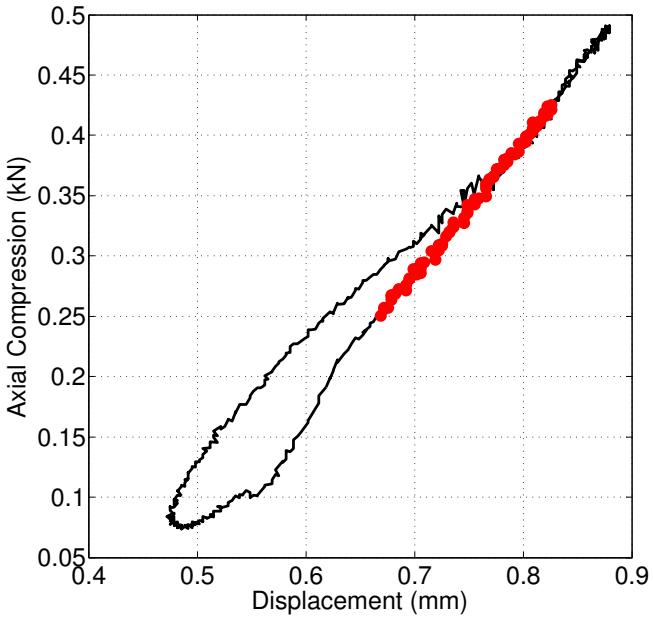

Figure A.3: Axial force versus displacement at the 10th cycle for specimen 1.3.

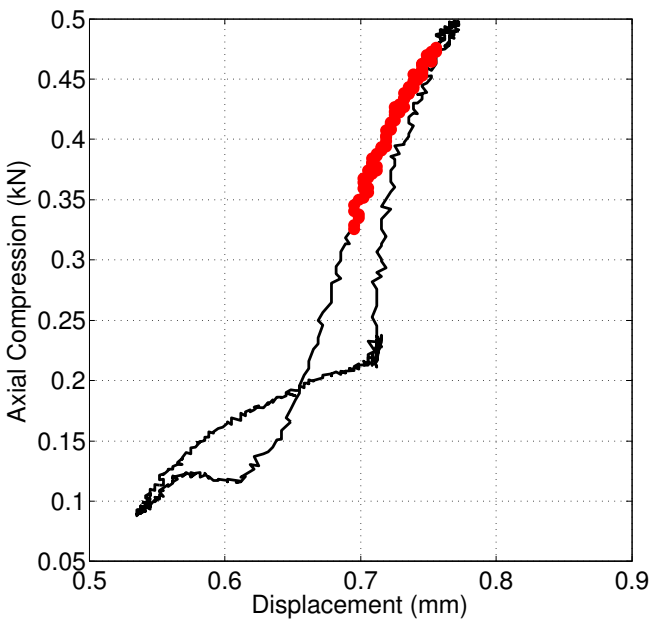

Figure A.4: Axial force versus displacement at the 10th cycle for specimen 1.4.

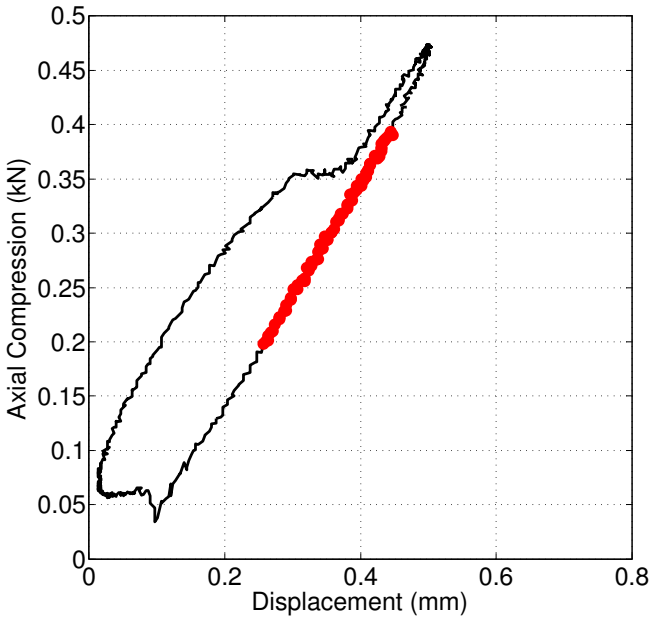

Figure A.5: Axial force versus displacement at the 10th cycle for specimen 1.5.

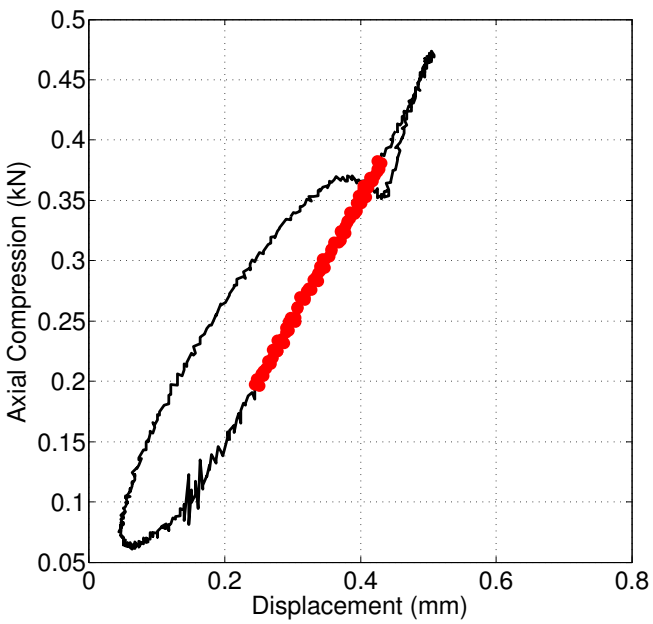

Figure A.6: Axial force versus displacement at the 10th cycle for specimen 1.6.

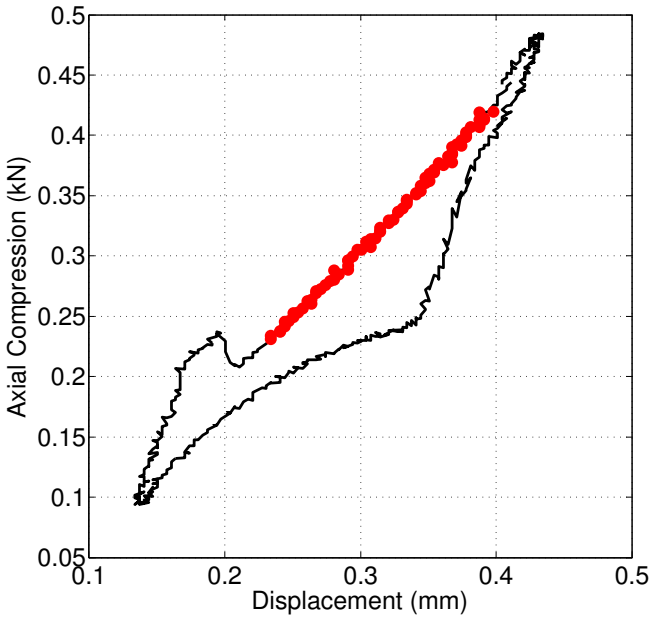

Figure A.7: Axial force versus displacement at the 10th cycle for specimen 1.7.

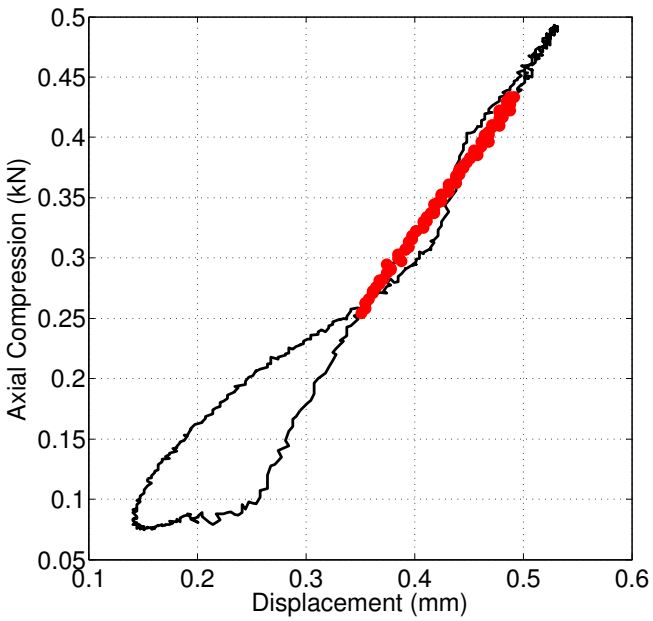

Figure A.8: Axial force versus displacement at the 10th cycle for specimen 1.8.

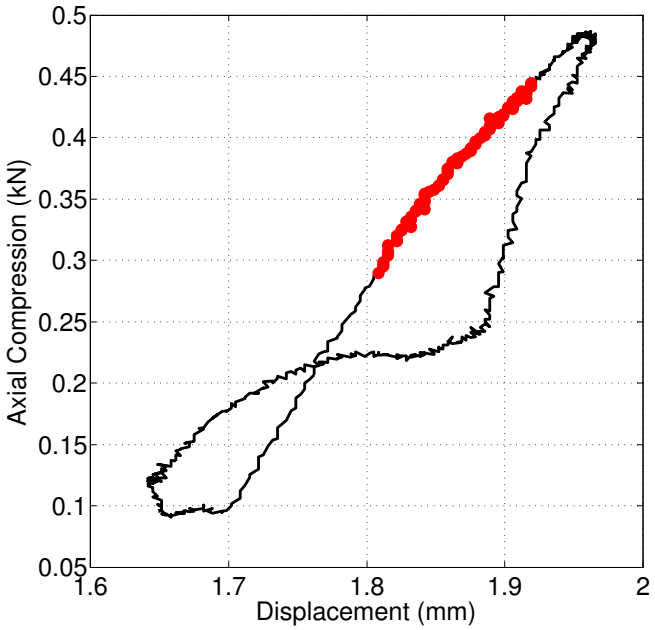

Figure A.9: Axial force versus displacement at the 10th cycle for specimen 2.1.

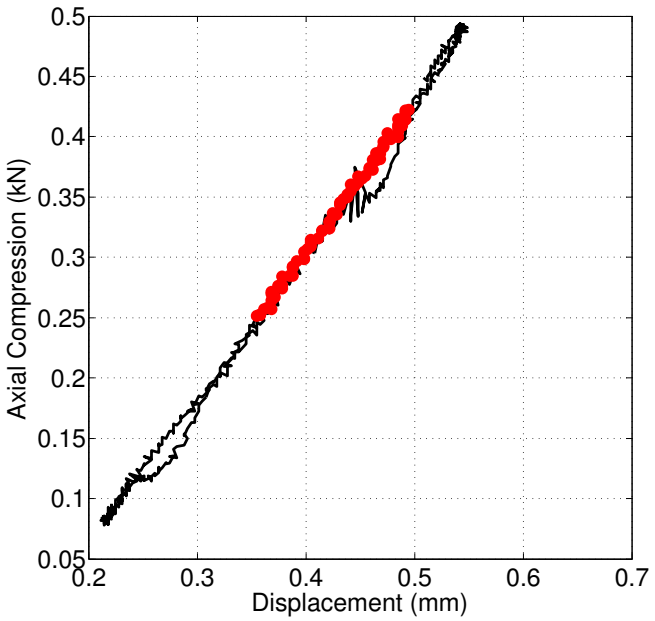

Figure A.10: Axial force versus displacement at the 10th cycle for specimen 2.2.

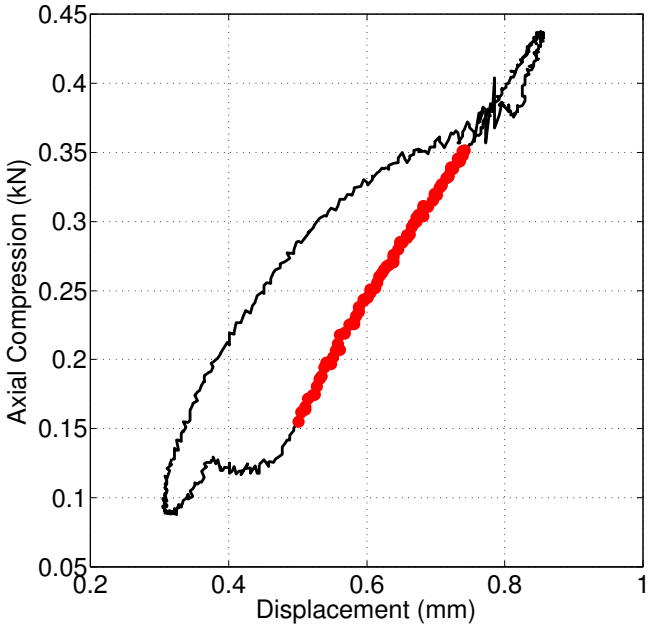

Figure A.11: Axial force versus displacement at the 10th cycle for specimen 2.3.

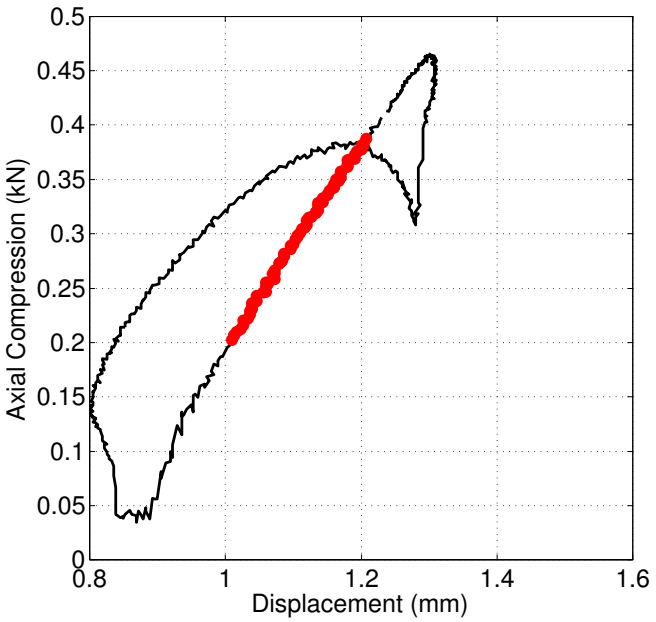

Figure A.12: Axial force versus displacement at the 10th cycle for specimen 2.4.

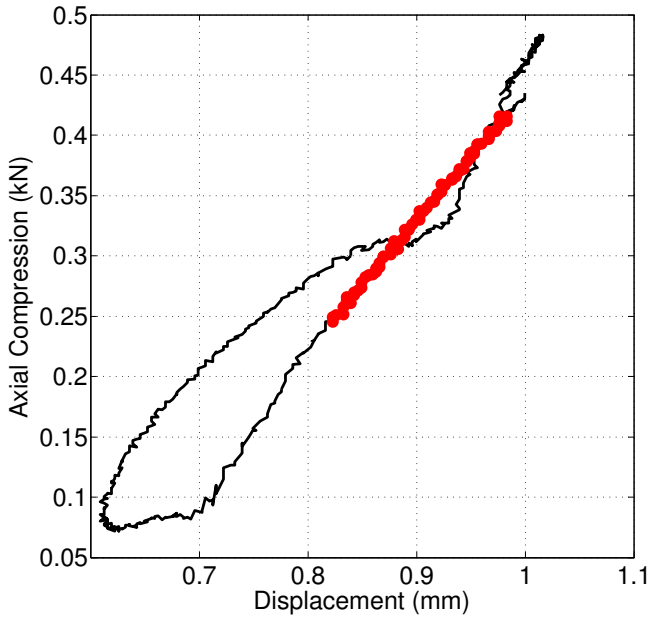

Figure A.13: Axial force versus displacement at the 10th cycle for specimen 2.5.

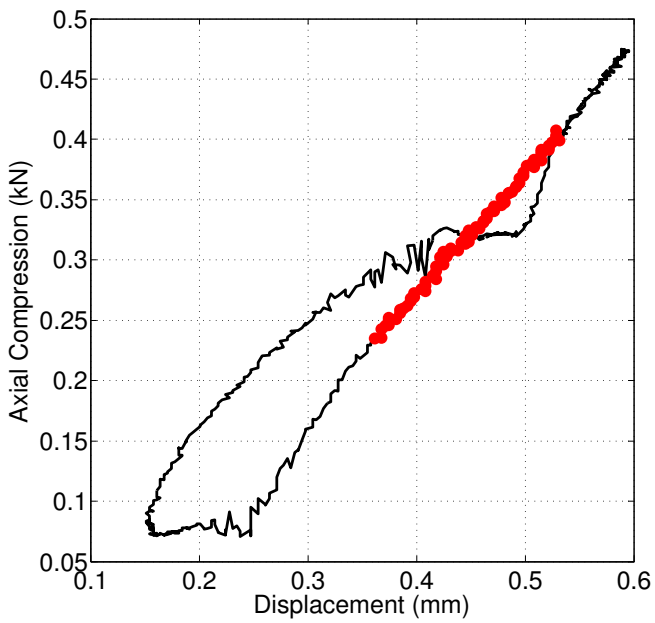

Figure A.14: Axial force versus displacement at the 10th cycle for specimen 2.6.

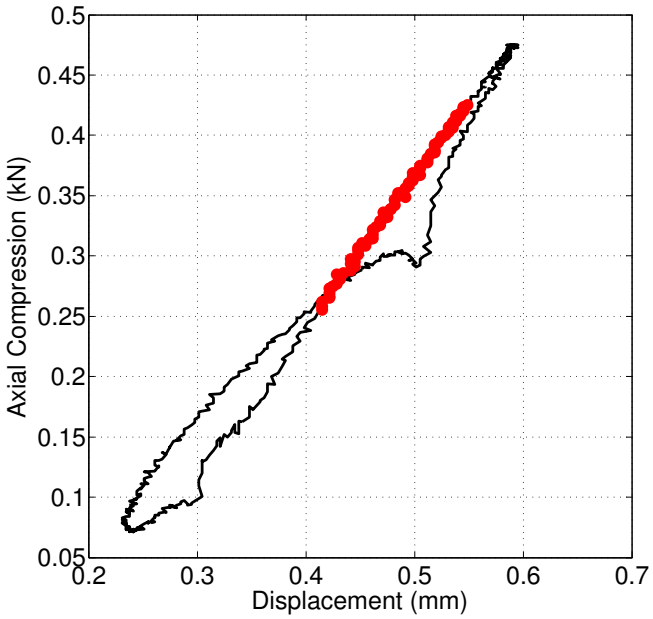

Figure A.15: Axial force versus displacement at the 10th cycle for specimen 2.7.

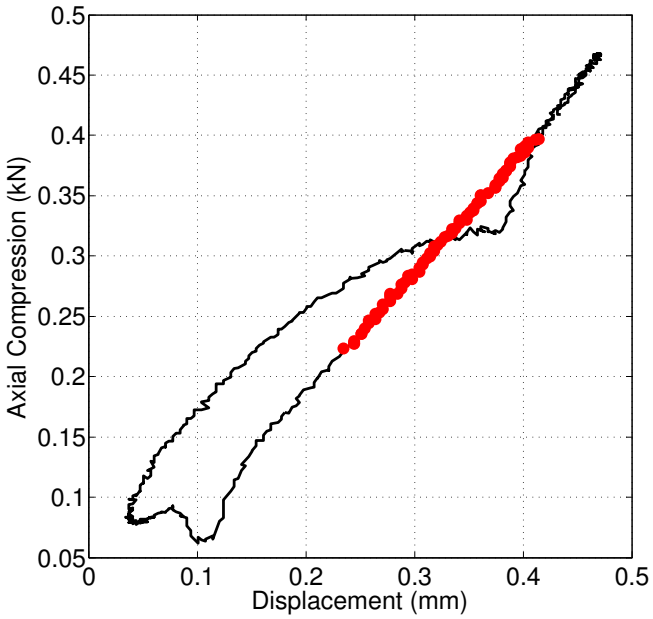

Figure A.16: Axial force versus displacement at the 10th cycle for specimen 2.8.

Appendix B

Torsional Load Versus Rotation Plots for Cycle 10

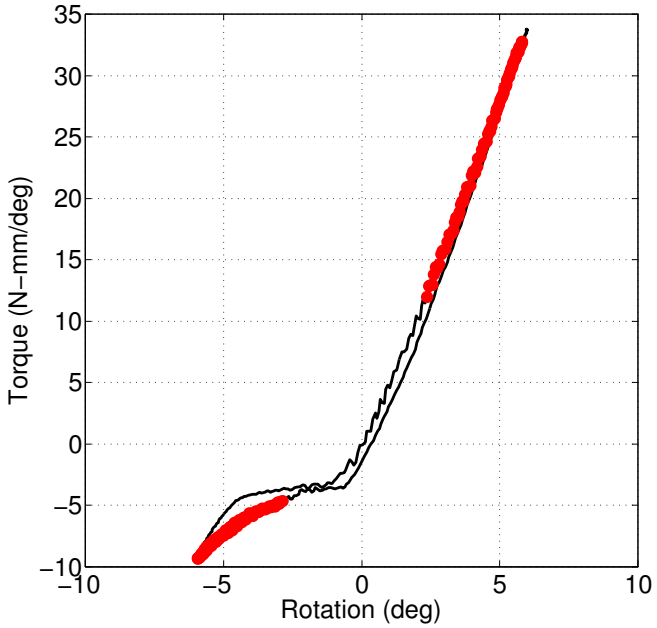

Figure B.1: Torsional moment versus rotation at the 10th cycle for specimen 1.1.

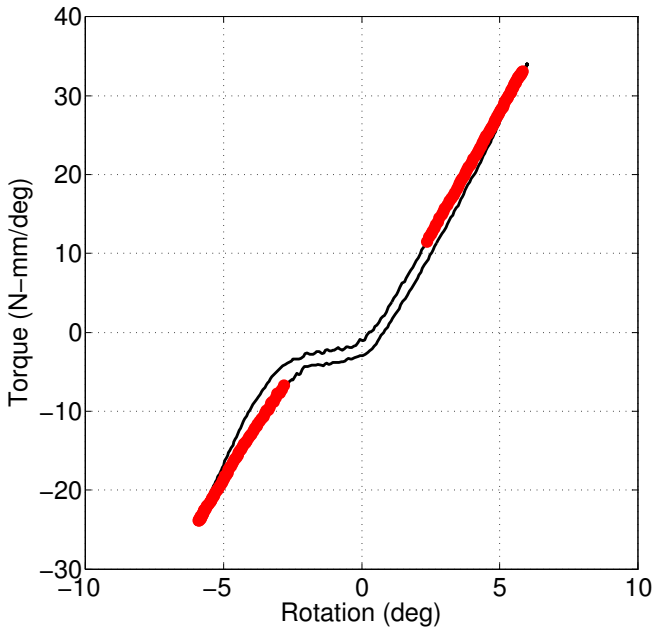

Figure B.2: Torsional moment versus rotation at the 10th cycle for specimen 1.2.

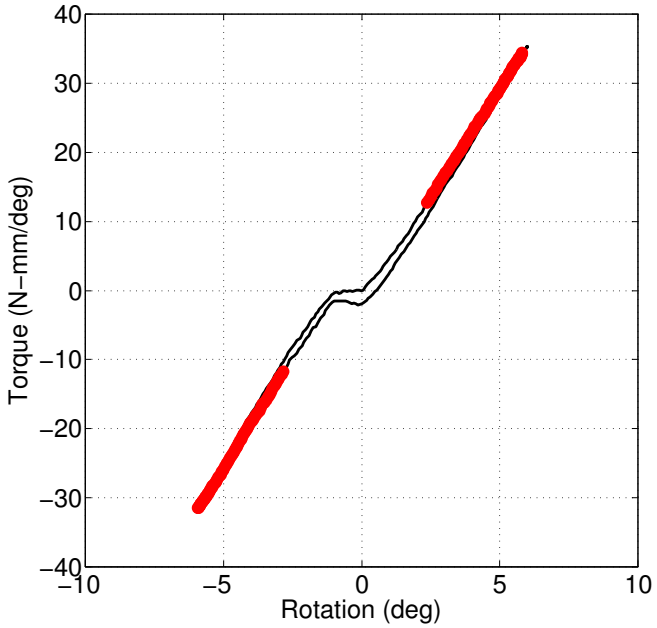

Figure B.3: Torsional moment versus rotation at the 10th cycle for specimen 1.3.

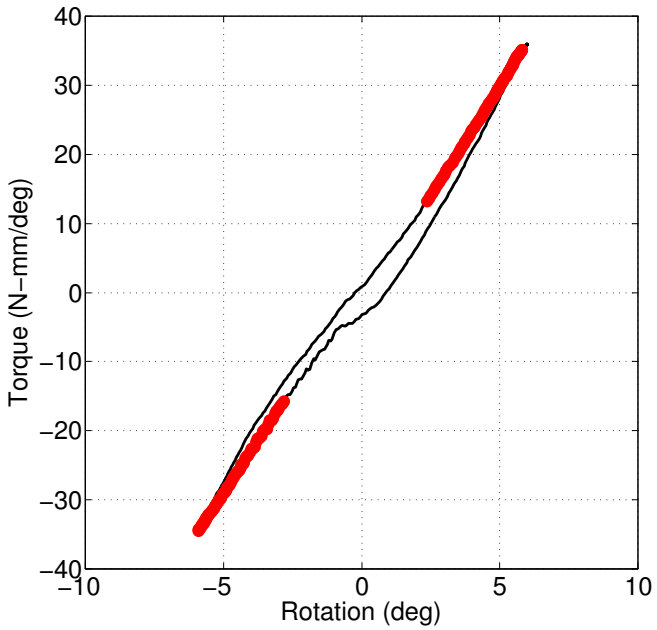

Figure B.4: Torsional moment versus rotation at the 10th cycle for specimen 1.4.

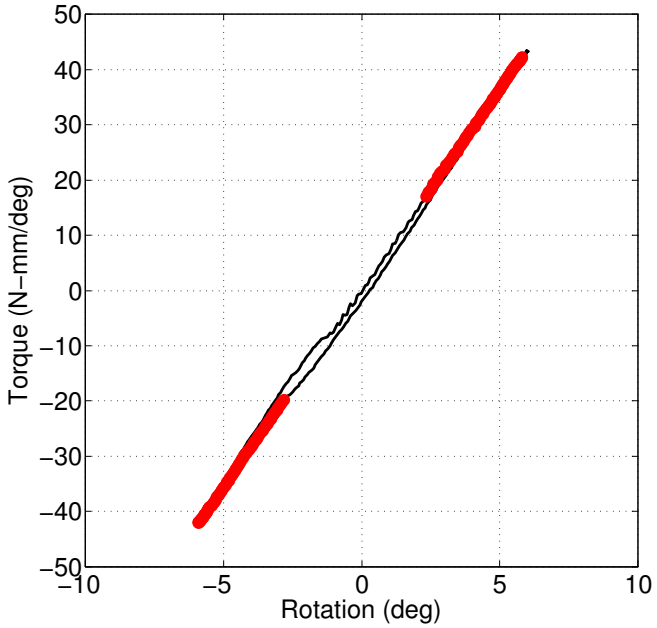

Figure B.5: Torsional moment versus rotation at the 10th cycle for specimen 1.5.

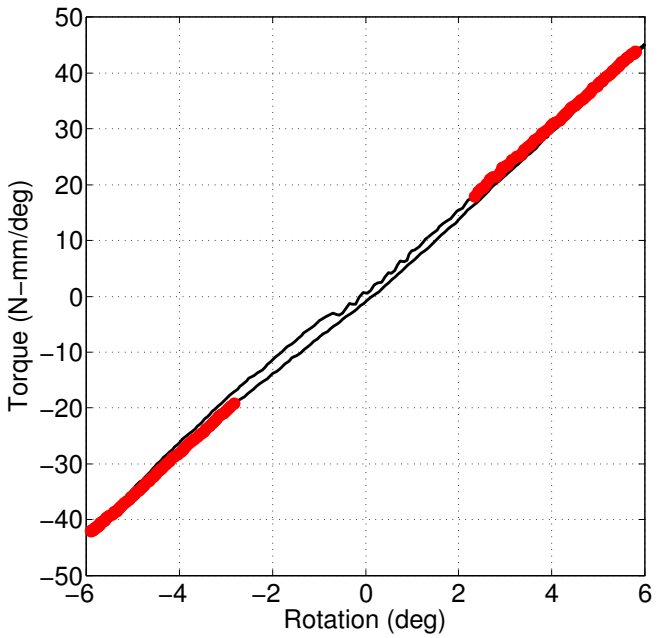

Figure B.6: Torsional moment versus rotation at the 10th cycle for specimen 1.6.

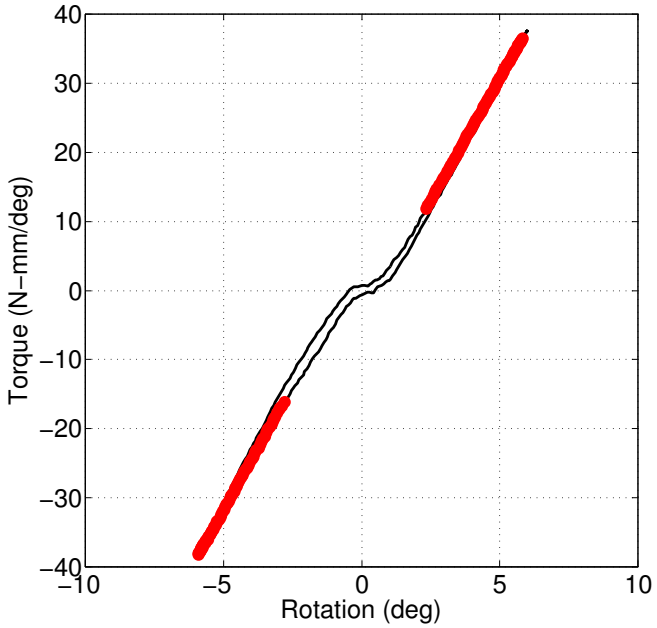

Figure B.7: Torsional moment versus rotation at the 10th cycle for specimen 1.7.

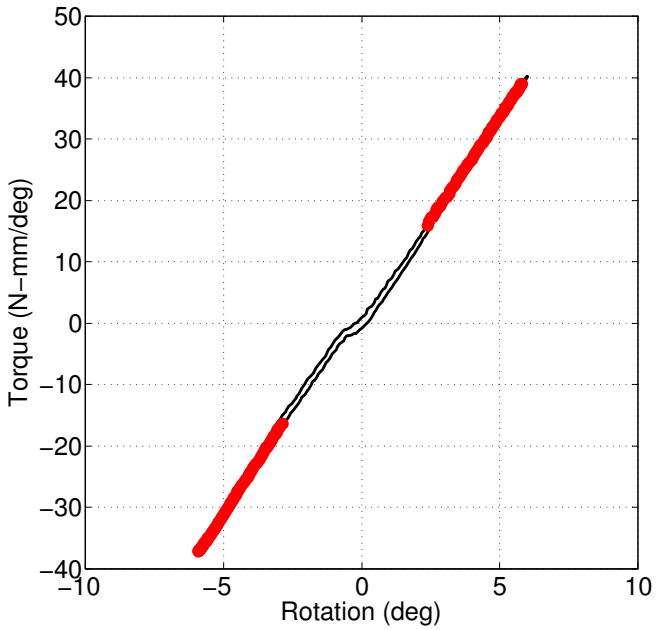

Figure B.8: Torsional momement versus rotation at the 10th cycle for specimen 1.8.

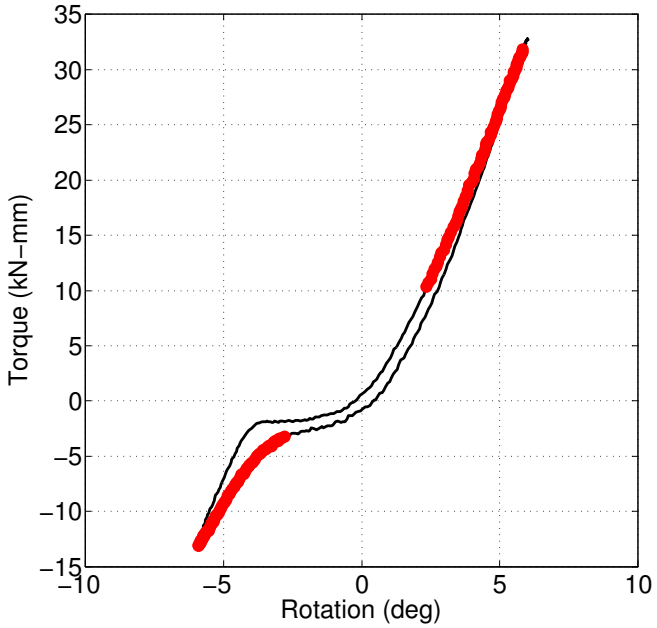

Figure B.9: Torsional moment versus rotation at the 10th cycle for specimen 2.1.

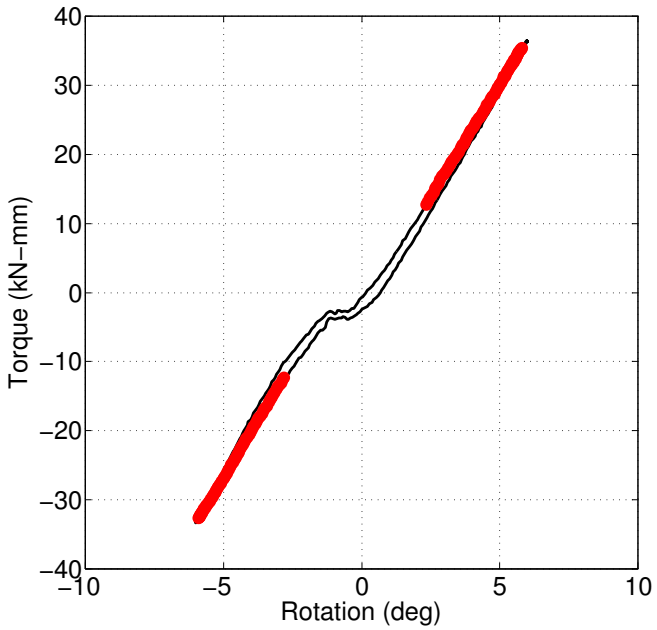

Figure B.10: Torsional moment versus rotation at the 10th cycle for specimen 2.2.

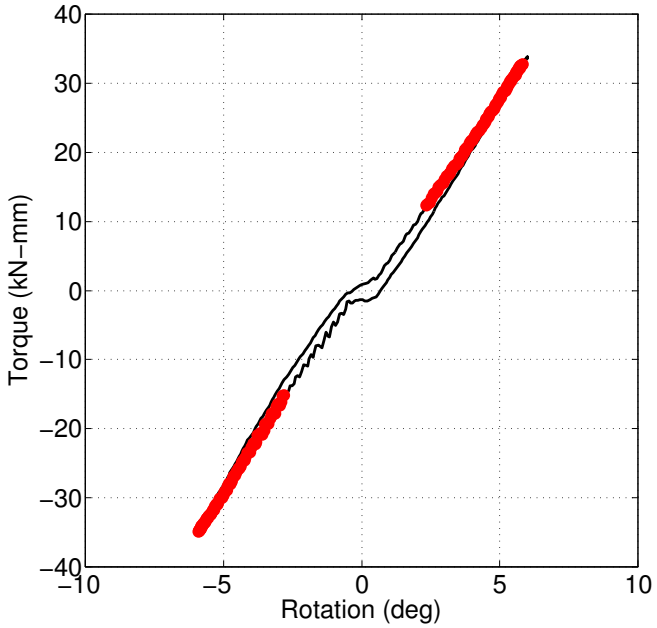

Figure B.11: Torsional moment versus rotation at the 10th cycle for specimen 2.3.

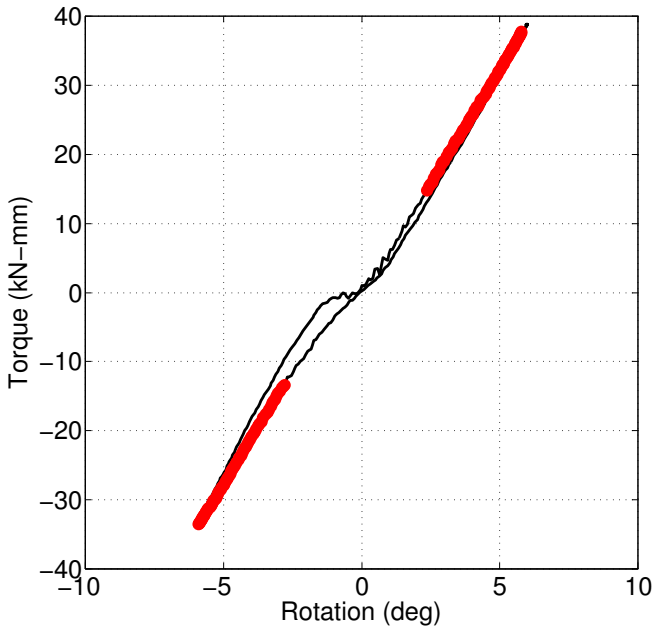

Figure B.12: Torsional moment versus rotation at the 10th cycle for specimen 2.4.

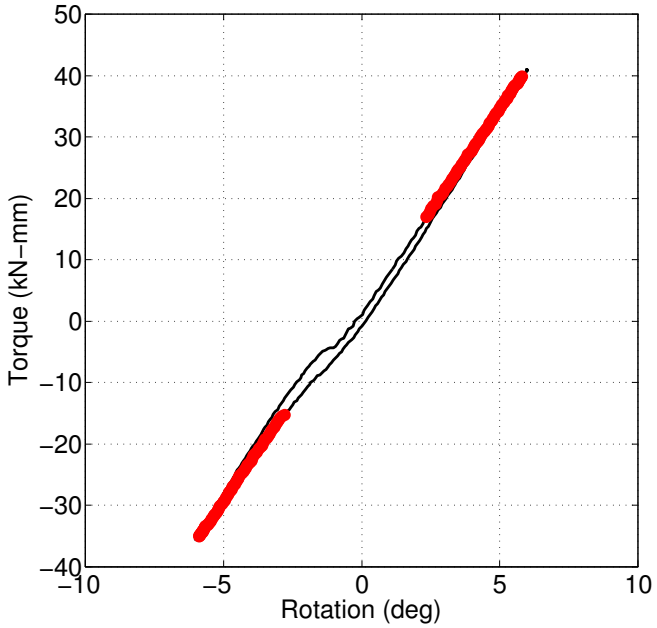

Figure B.13: Torsional moment versus rotation at the 10th cycle for specimen 2.5.

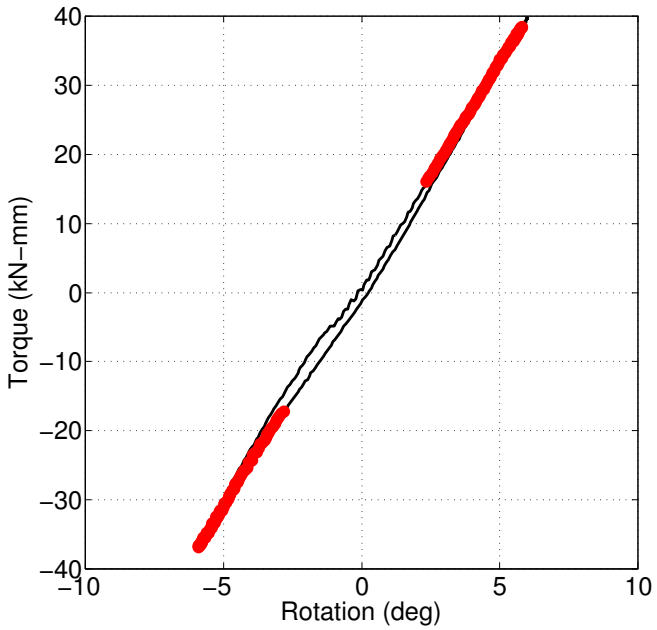

Figure B.14: Torsional moment versus rotation at the 10th cycle for specimen 2.6.

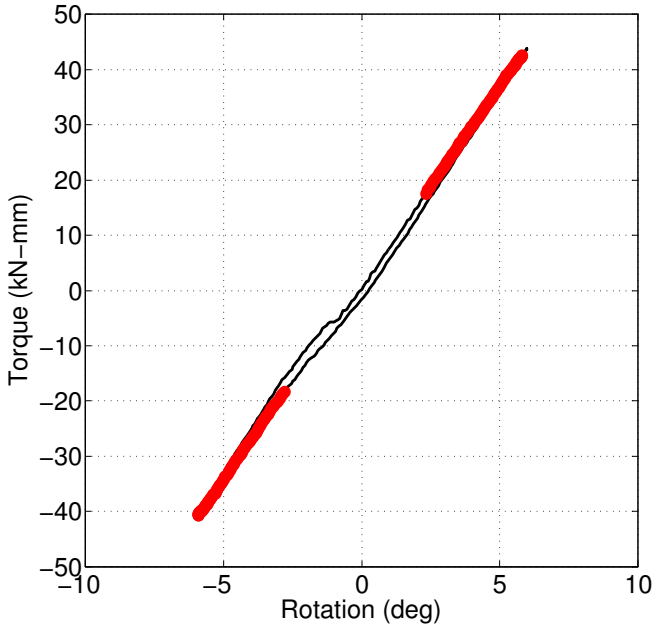

Figure B.15: Torsional moment versus rotation at the 10th cycle for specimen 2.7.

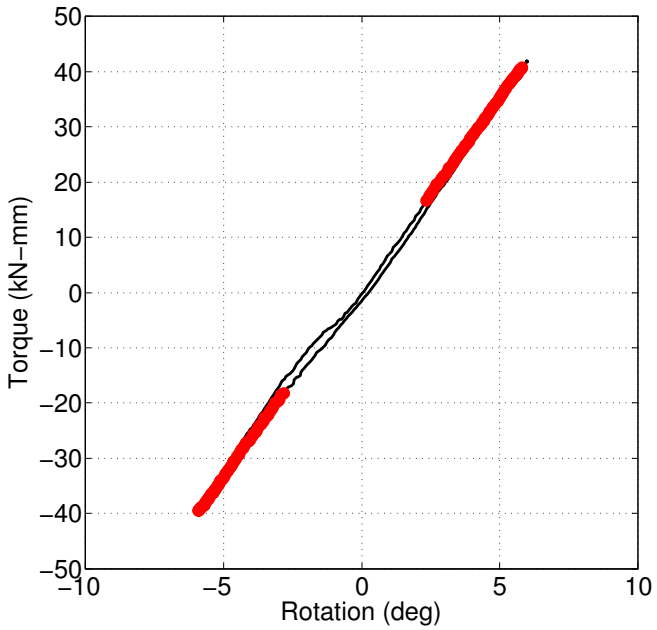

Figure B.16: Torsional moment versus rotation at the 10th cycle for specimen 2.8.

Appendix C

Axial Damage Versus Cycle Number

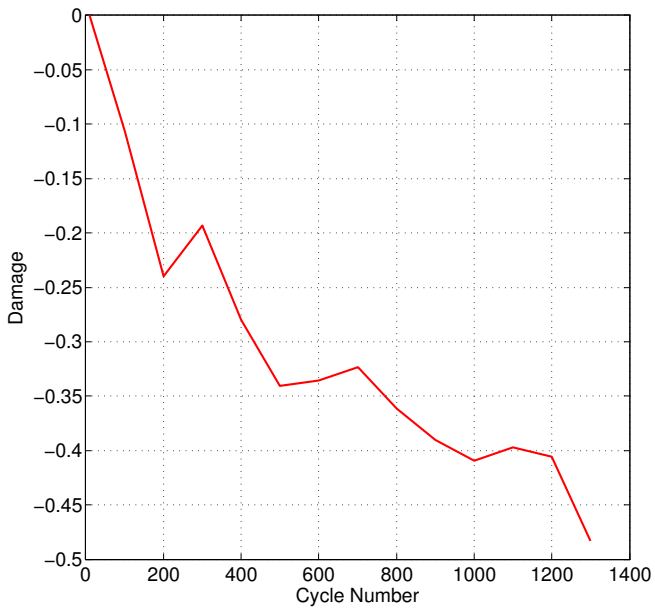

Figure C.1: Axial damage versus cycle number for specimen 1.1.

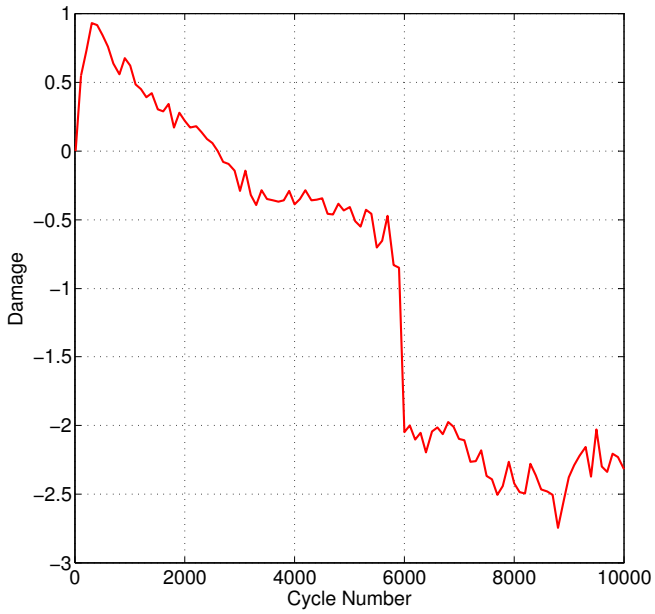

Figure C.2: Axial damage versus cycle number for specimen 1.2.

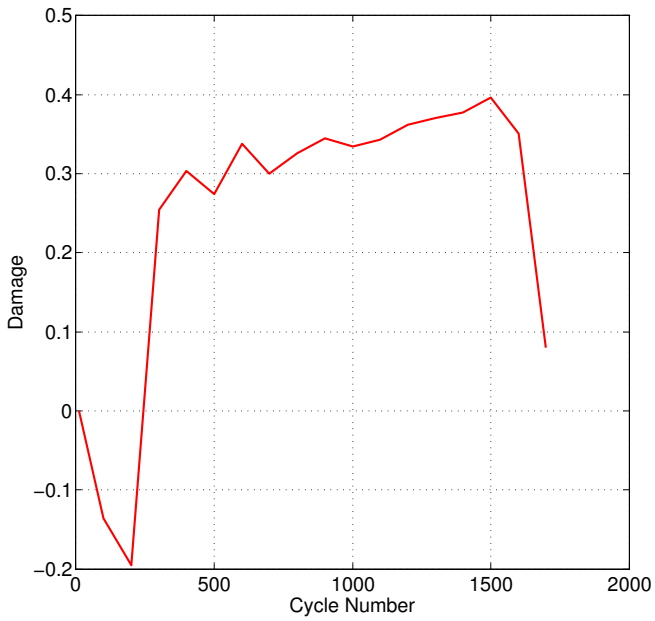

Figure C.3: Axial damage versus cycle number for specimen 1.3.

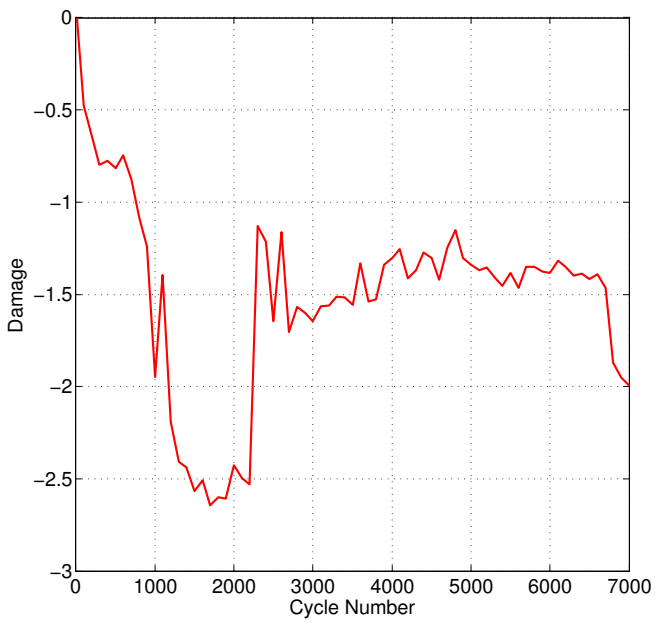

Figure C.4: Axial damage versus cycle number for specimen 1.4.

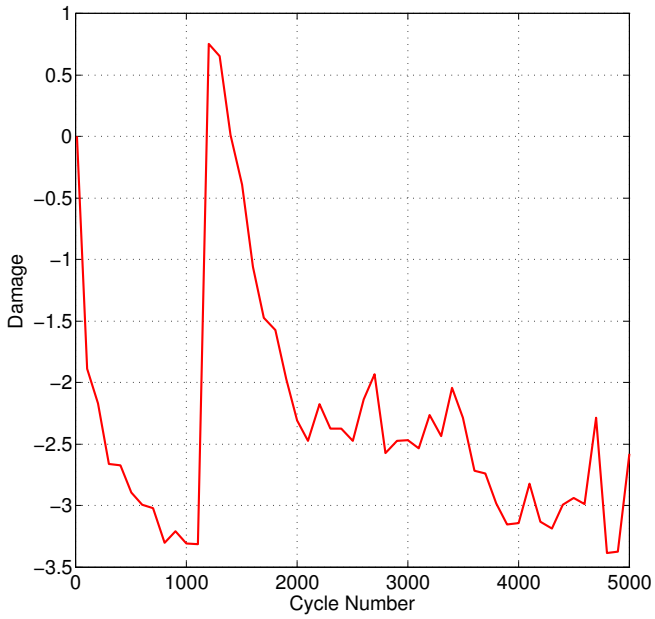

Figure C.5: Axial damage versus cycle number for specimen 1.5.

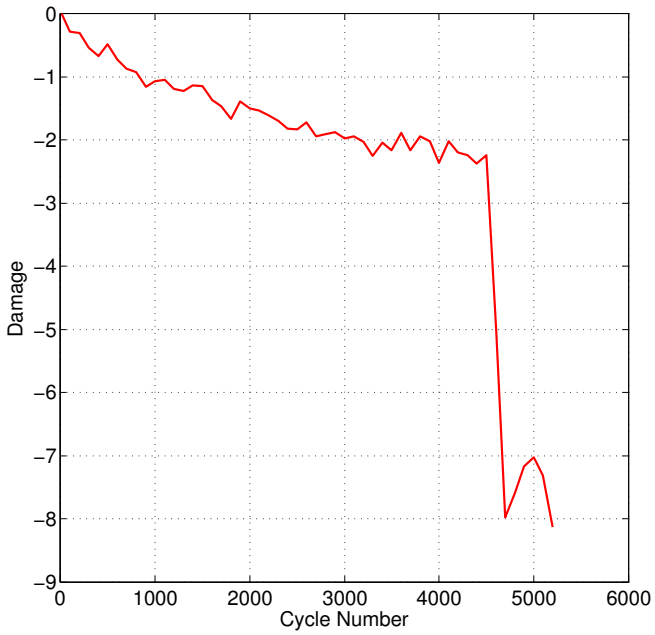

Figure C.6: Axial damage versus cycle number for specimen 1.6.

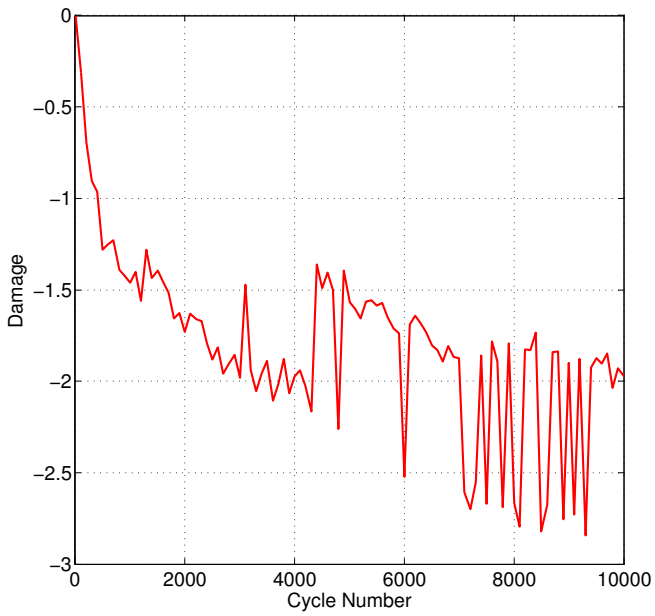

Figure C.7: Axial damage versus cycle number for specimen 1.7.

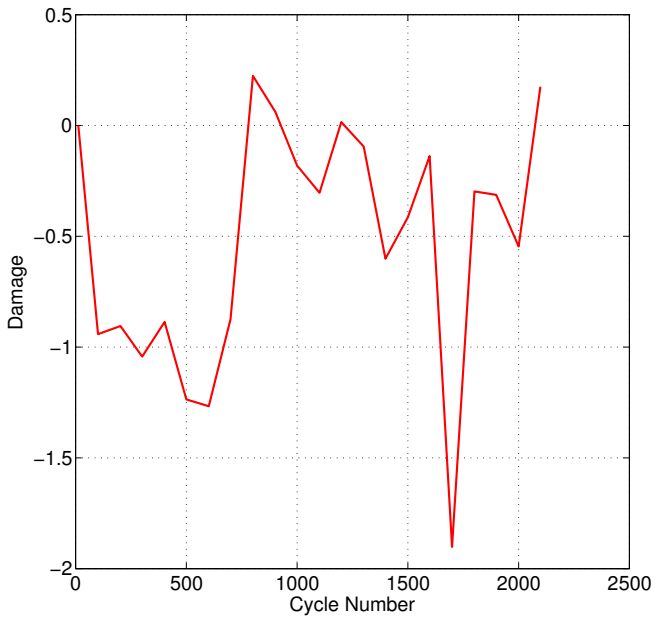

Figure C.8: Axial damage versus cycle number for specimen 1.8.

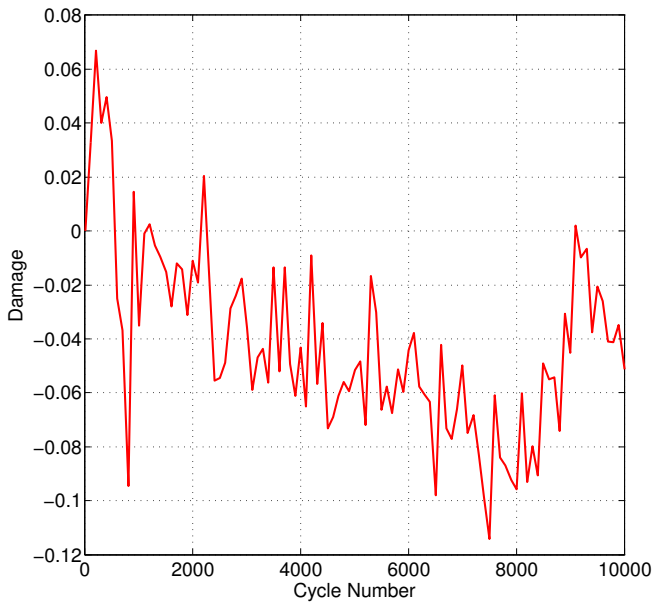

Figure C.9: Axial damage versus cycle number for specimen 2.1.

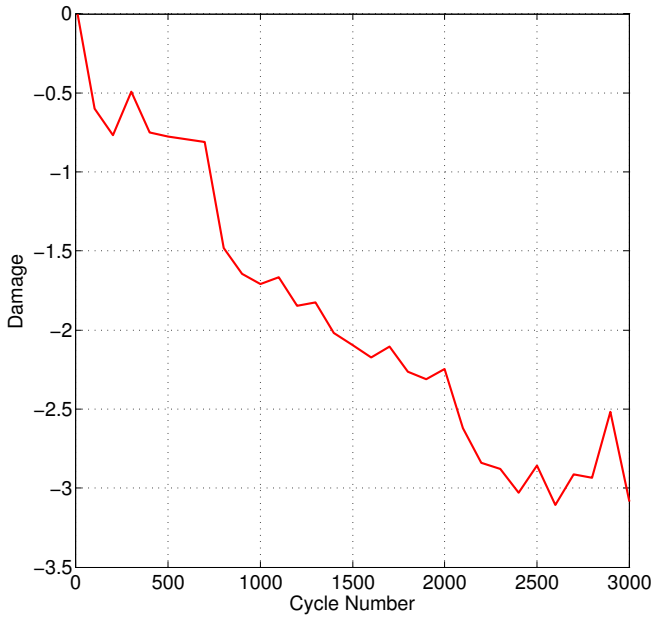

Figure C.10: Axial damage versus cycle number for specimen 2.2.

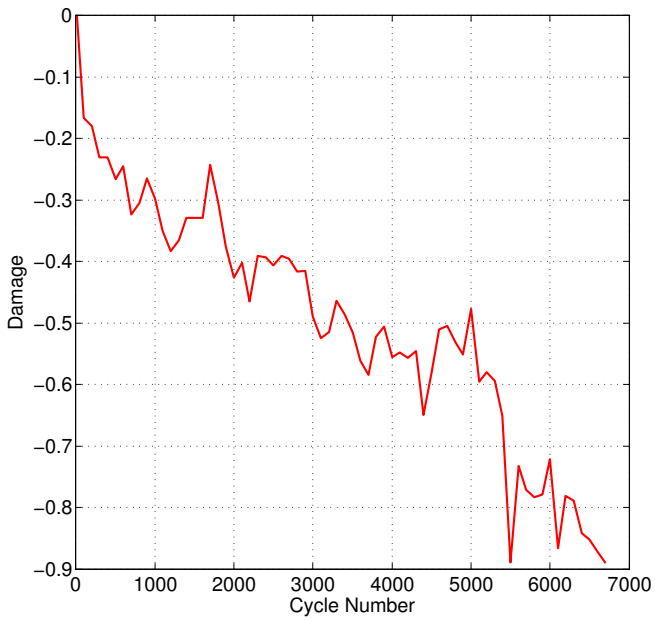

Figure C.11: Axial damage versus cycle number for specimen 2.3.

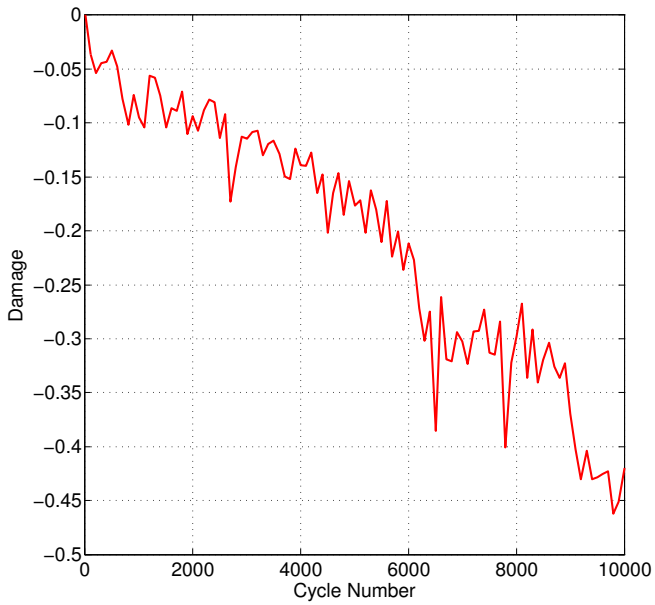

Figure C.12: Axial damage versus cycle number for specimen 2.4.

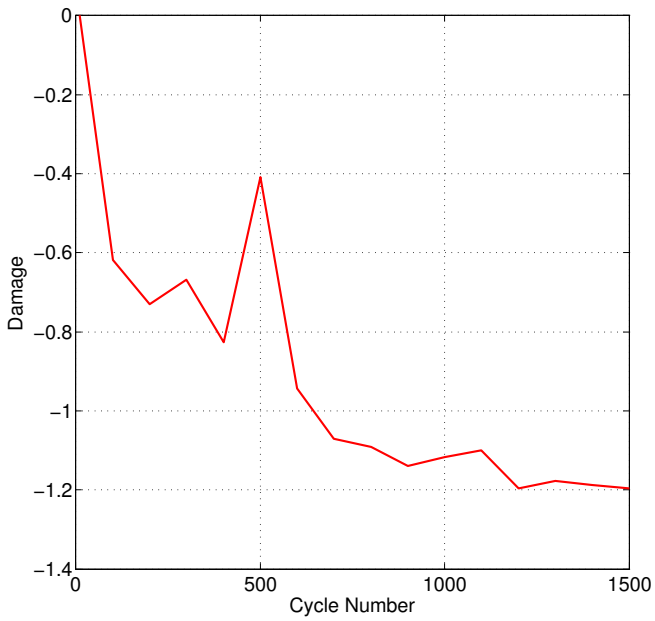

Figure C.13: Axial damage versus cycle number for specimen 2.5.

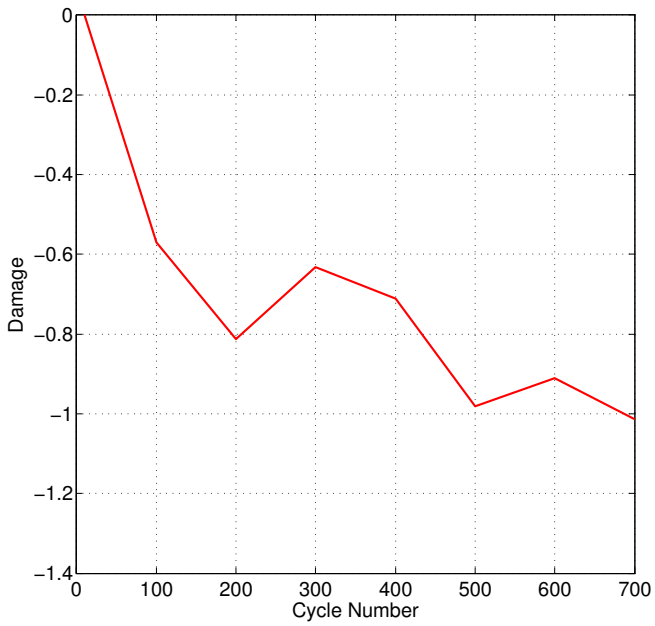

Figure C.14: Axial damage versus cycle number for specimen 2.6.

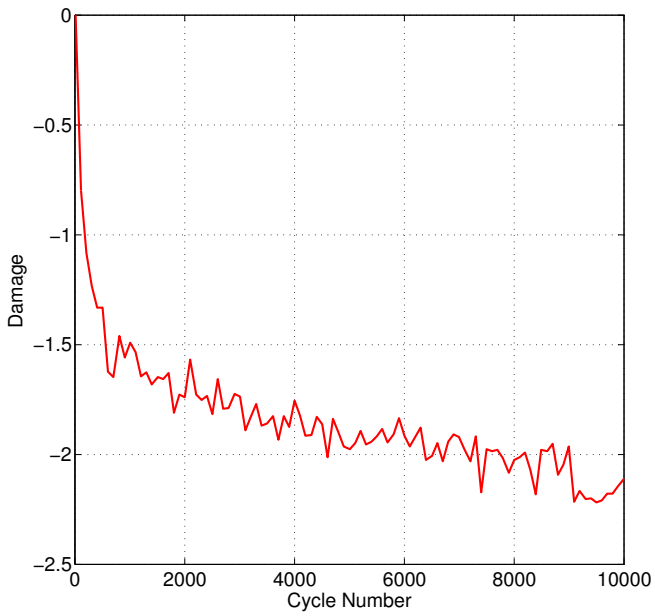

Figure C.15: Axial damage versus cycle number for specimen 2.7.

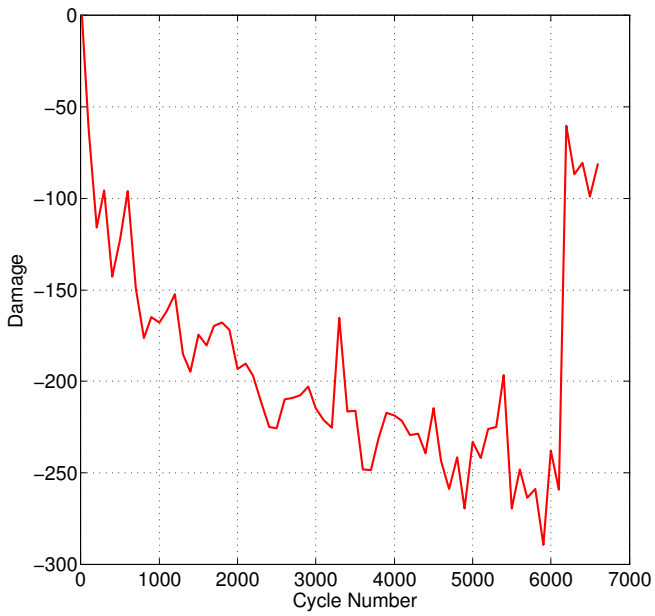

Figure C.16: Axial damage versus cycle number for specimen 2.8.

Appendix D

Torsional Damage Versus Cycle Number

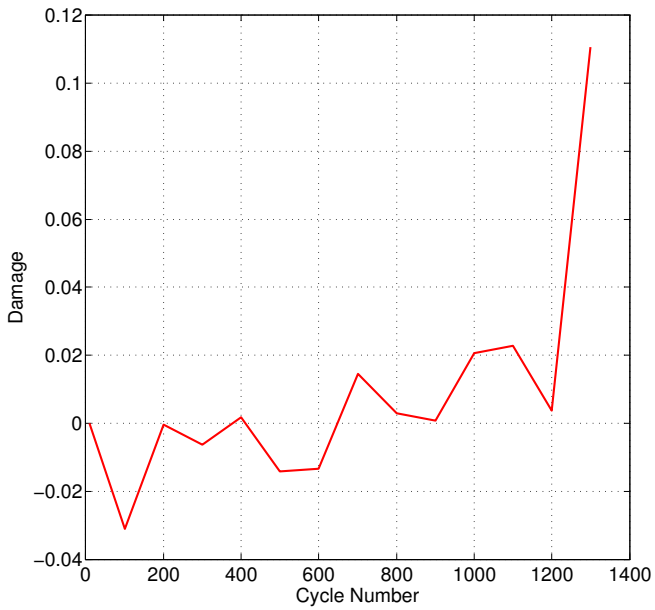

Figure D.1: Torsional damage versus cycle number for specimen 1.1.

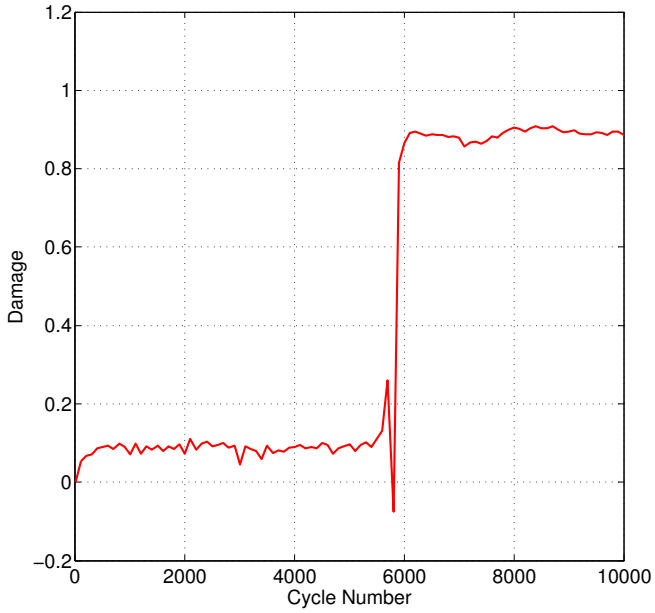

Figure D.2: Torsional damage versus cycle number for specimen 1.2.

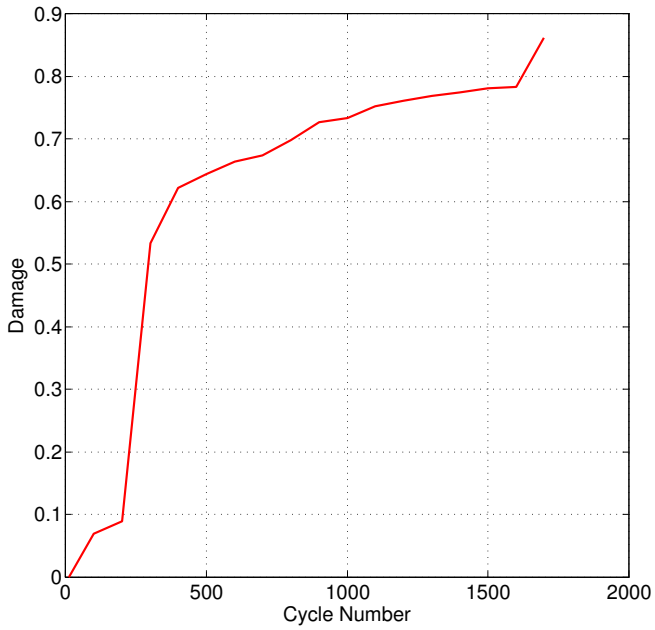

Figure D.3: Torsional damage versus cycle number for specimen 1.3.

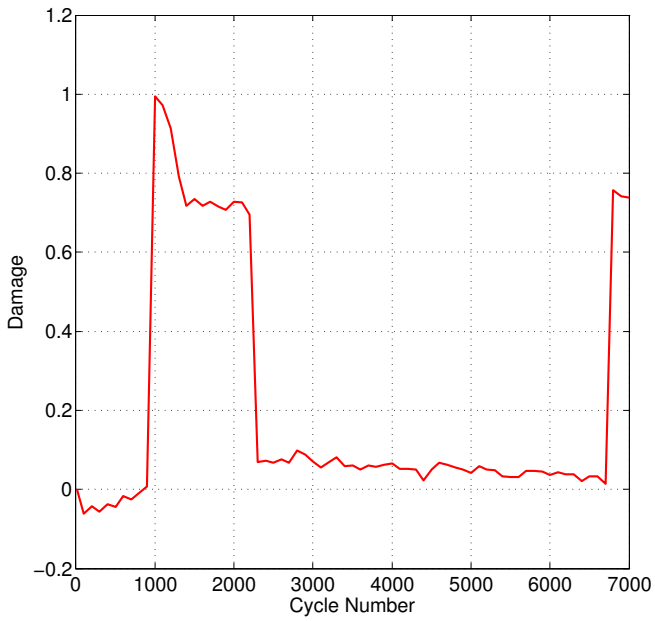

Figure D.4: Torsional damage versus cycle number for specimen 1.4.

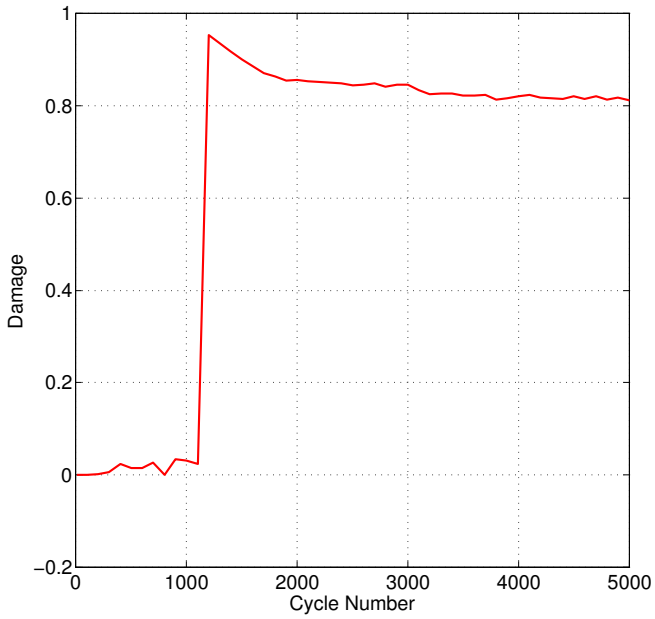

Figure D.5: Torsional damage versus cycle number for specimen 1.5.

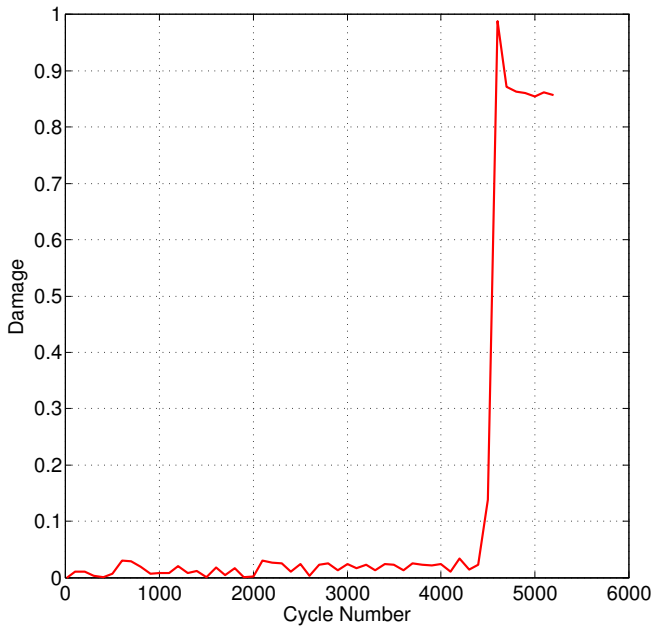

Figure D.6: Torsional damage versus cycle number for specimen 1.6.

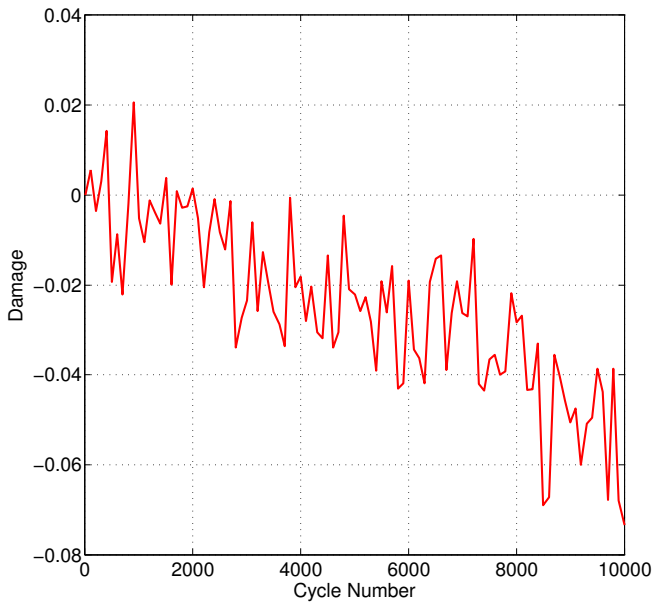

Figure D.7: Torsional damage versus cycle number for specimen 1.7.

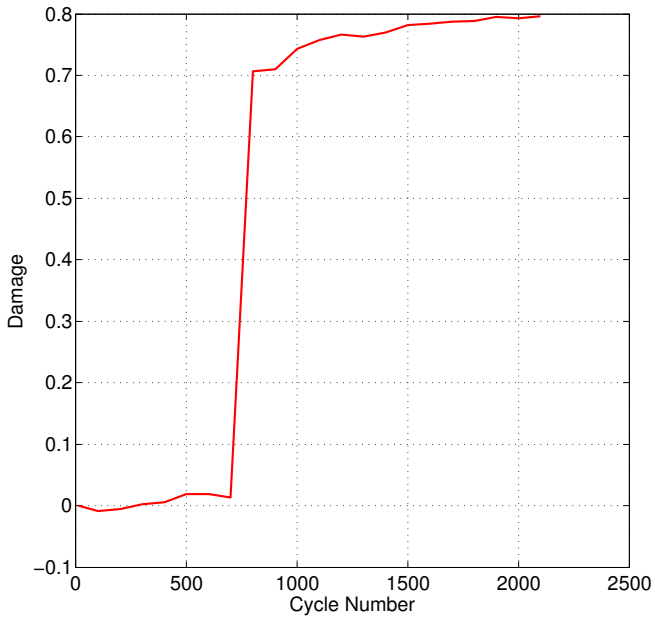

Figure D.8: Torsional damage versus cycle number for specimen 1.8.

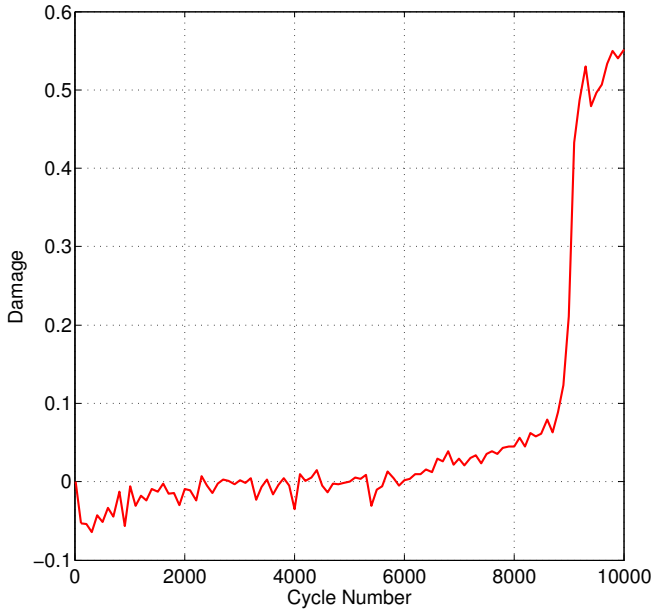

Figure D.9: Torsional damage versus cycle number for specimen 2.1.

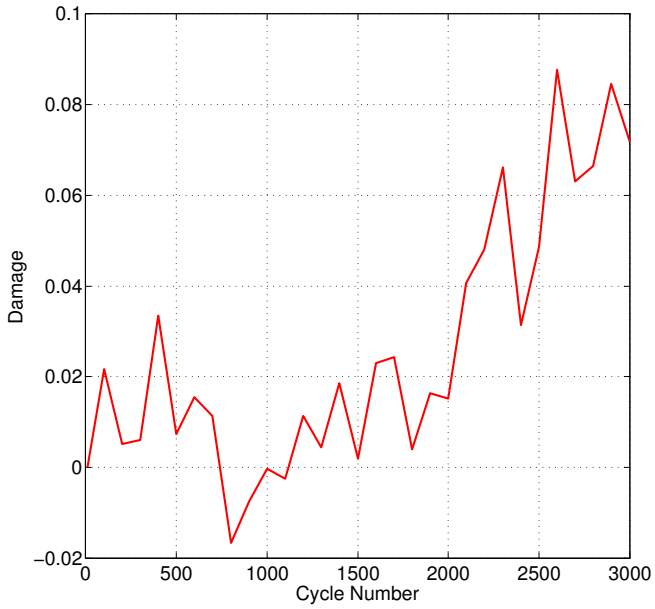

Figure D.10: Torsional damage versus cycle number for specimen 2.2.

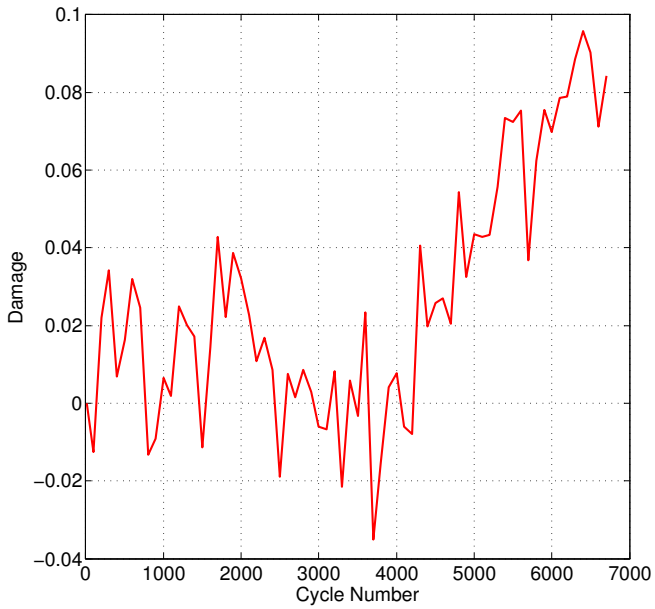

Figure D.11: Torsional damage versus cycle number for specimen 2.3.

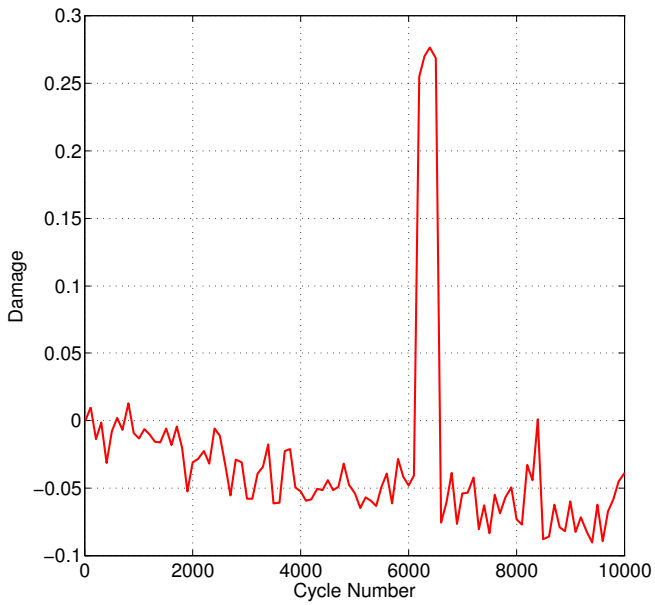

Figure D.12: Torsional damage versus cycle number for specimen 2.4.

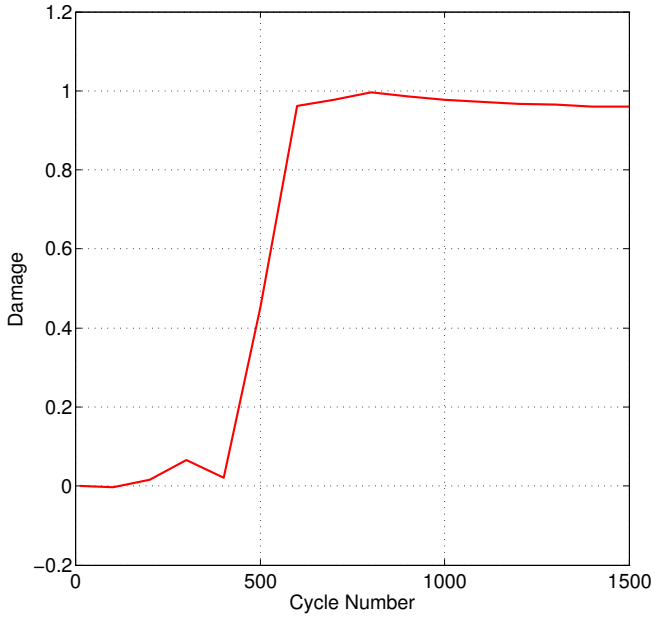

Figure D.13: Torsional damage versus cycle number for specimen 2.5.

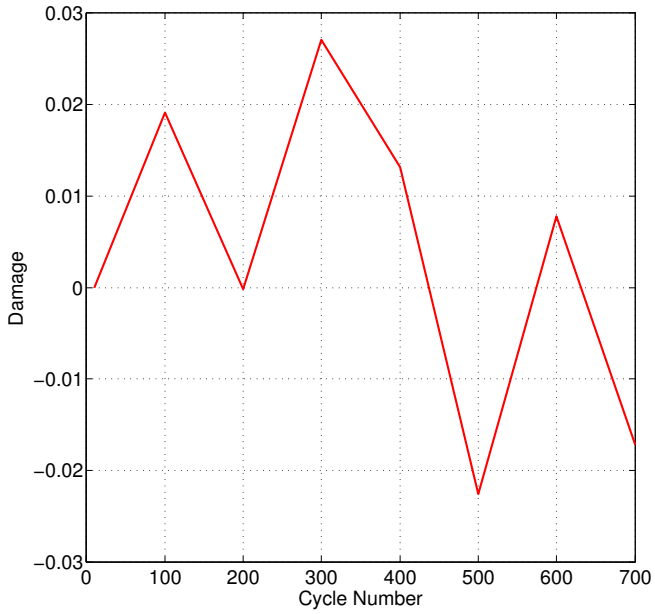

Figure D.14: Torsional damage versus cycle number for specimen 2.6.

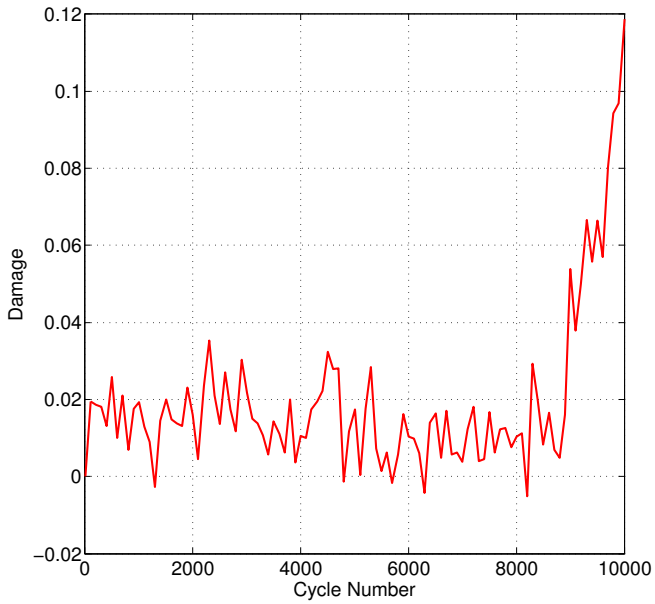

Figure D.15: Torsional damage versus cycle number for specimen 2.7.

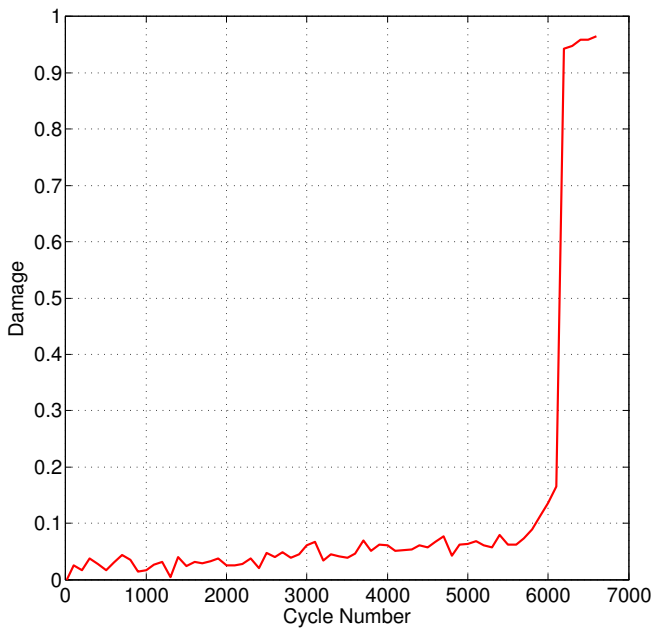

Figure D.16: Torsional damage versus cycle number for specimen 2.8.

References

[1] American Academy of Orthopaedic Surgeons. Bone tumor, June 2010. Available from: http://orthoinfo.aaos.org/topic.cfm?topic=a00074.

[2] American Academy of Orthopaedic Surgeons. Giant cell tumor of bone, June 2010. Available from: http://orthoinfo.aaos.org/topic.cfm?topic=a00080.

[3] E. N. Marieb and K. Hoehn. *Anatomy & Physiology*. Pearson Education, Inc., 4th edition, 2013.

[4] N. Palastanga, D. Field, and R. Soames. *Anatomy and Human Movement: Structure and Function*. Elsevier Ltd., 5th edition, 2006.

[5] The Database Center for Life Science. Bodyparts 3d/anatomography, c2008. Licensed under CC Attribution–Share Alike 2.1 Japan. Available from: http://www.cancer.org/acs/groups/content/@research/documents/webcontent/acspc-042151.pdf.

[6] Y. Yoshioka, D. Siu, and T. D. Cooke. The anatomy and functional axes of the femur. *J Bone Joint Surg Am*, 69(6):873–80, 1987.

[7] J. J. Gugenheim Jr. and M. R. Brinker. Bone realignment with use of temporary external fixation for distal femoral valgus and varus deformities. *J Bone Joint Surg Am*, 85(7):1229–37, 2003.

[8] L. Pecorino. *Molecular Biology of Cancer. Mechanisms, Targets, and Therapeutics*. Oxford University Press Inc., 198 Madison Avenue New York, NY 10016 USA, 2nd edition, 2008.

[9] Holland JF. *Holland-Frei Cancer Medicine*. Hamilton (ON): BC Decker, 6th edition, 2003. Available from http://www-ncbi-nlm-nih-gov.libproxy.unm.edu/books/NBK12489/.

[10] American Cancer Society. Cancer facts & figures 2014, 2014. Available from: http://www.cancer.org/acs/groups/content/@research/documents/webcontent/acspc-042151.pdf.

[11] National Cancer Institute at the National Institutes of Health. Bone cancer, 2008. Available from: http://www.cancer.gov/cancertopics/factsheet/Sites-Types/bone#r5.

[12] A. M. Davies, M. Sundaram, and S. L. J James. *Imaging of Bone Tumors and Tumor-like lesions. Techniques and Applications*. Medical Radiology. Springer, Berlin, Heidelberg, Germany, 2009.

[13] C.D.M. Fletcher, K.K. Unni, F. Mertens, World Health Organization, and International Academy of Pathology. *Pathology and Genetics of Tumours of Soft Tissue and Bone*. Iarc WHO Classification of Tumours Series. IARC Press, 2002.

[14] M. Ashby, H. Shercliff, and D. Cebon. *Materials. engineering science, processing and design*. Elsevier Ltd, 30 Corporate Drive, suite 400, Burlington, MA 01803, USA, 2nd edition, 2010.

[15] R. K. Beals, G. D. Lawton, and W. E. Snell. Prophylactic internal fixations of the femur in metastatic breast cancer. *Cancer*, 28:1350–1354, 1971.

[16] F. F. Parrish and J. A. Murray. Surgical treatment for secondary neoplastic fractures. a retrospective study of ninety-six patients. *J Bone Joint Surg Am*, 52A:665–686, 1970.

[17] M. Fidler. Incidence of fracture of metastases in long bones. *Acta Orthop Scand*, 52:623–627, 1973.

[18] C. O. Bechtol. Engineering principles applied to orthopaedic surgery. *In Instructional Course Lectures, The American Academy of Orthopaedic Surgeons*, 9:257–264, 1952.

[19] D. B. Brooks, Burstein A. H., and V. H. Frankel. The biomechanics of torsional fractures. the stress concentration effect of a drill hole. *J Bone Joint Surg Am*, 52-A(3):507–14, 1970.

[20] C. R. Clark, C. Morgan, D. A. Sonstegard, and L. S. Matthews. The effect of biopsy-hole shape and size on bone strength. *J Bone Joint Surg Am*, 59-A(2):213–17, 1977.

[21] A. H. Burstein and V. H. Frankel. A standard test for laboratory animal bone. *J Biomech*, 4(2):155–8, 1971.

[22] R. J. McBroom and W. C. Hayes. Strength reductions and fracture risk of cortical defects in the diaphysis of long bones. *Trans 30th ORS*, 9:330, 1984.

[23] B.C. Edgerton, K.N. An, and B.F. Morrey. Cortical defects in bone: an analysis of the "open-section" versus "stress-riser" effects under torsional load. *Trans 33rd ORS*, 12:191, 1987.

[24] R. E. Leggon, R. W. Lindsey, and M. M. Panjabi. Strength reduction and the effects of treatment of long bones with diaphyseal defects involving 50% of the cortex. *J Orthop Res*, 6(4):540–6, 1988.

[25] R. J. McBroom, E. J. Cheal, and W. C. Hayes. Strength reductions from metastatic cortical defects in long bones. *J Orthop Res*, 6(3):369–78, 1988.

[26] B. C. Edgerton, K. N. An, and B. F. Morrey. Torsional strength reduction due to cortical defects in bone. *J Orthop Res*, 8(6):851–5, 1990.

[27] J. A. Hipp, R. J. McBroom, E. J. Cheal, and W. C. Hayes. Structural consequences of endosteal metastatic lesions in long bones. *J Orthop Res*, 7(6):828–37, 1989.

[28] H. W. Smith, A. A. DeSmet, and E. Levine. Measurement of cortical thickness in a human cadaver femur. conventional roentgenography versus computed tomography. *Clin Orthop Rel Res*, 169:269–274, 1982.

[29] H. R. Blackley, J. S. Wunder, A. M. Davis, L. M. White, R. Kandel, and R. S. Bell. Treatment of giant-cell tumors of long-bones with curettage and bone-grafting. *J Bone Joint Surg Am*, 81:811–20, 1999.

[30] C. G. Finkemeier. Bone-grafting and bone-graft substitutes. *J Bone Joint Surg Am*, 84:454–64, 2002.

[31] H. N. Shih, Y. J. Chen, T. J. Huang, K. Y. Hsu, and R. W. Hsu. Semistructural allografting in bone defects after curettage. *J Surg Oncol*, 68(3):159–65, 1998.

[32] A. Sethi, K. Agarwal, S. Sethi, S. Kumar, S. K. Marya, and S. M. Tuli. Allograft in the treatment of benign cystic lesions of the bone. *Arch Orthop Trauma Surg*, 112:167–70, 1993.

[33] W. W. Tomford. Transmission of disease through transplantation of musculoskeletal alografts. *J Bone Joint Surg Am*, 77:1742–54, 1995.

[34] V. M. Moretti, R. L. Slotcavage, E. A. Crawford, R. D. Lackman, and C. M. Ogilvie. Curettage and graft alleviates athletic-limiting pain in benign lytic bone lesions. *Clin Orthop Relat Res*, 469:283–88, 2011.

[35] B. Mjöberg, H. Pettersson, R. Rosenqvist, and A. Rydholm. Bone cement, thermal injury and the radiolucent zone. *Acta Orthop Scand*, 6(3):369–78, 1988.

[36] J. R. Ryan and P. C. Begeman. The effects of filling experimental large cortical defects with methylmethacrylate. *Clin Orthop*, 185:306–10, 1984.

[37] R. J. O'Donnell, D. S. Springfield, Ready J. E. Motwani, H. K., and M. C. Gebhardt. Recurrence of giant-cell tumors of long bones after curettage and packing with cement. *J Bone Joint Surg Am*, 76:1827–33, 1994.

[38] H. R. Bucholz. Nonallograft osteoconductive bone graft substitutes. *Clin Orthop*, 385:44–52, 2002.

[39] N. J. Dunne and J. F. Orr. Curing characteristics of acrylic bone cement. *J Mater Sci Mater Med*, 13:17–22, 2002.

[40] M. Campanacci, R. Capanna, N. Fabbri, and G. Bettelli. Curretage of giant cell tumor of bone. reconstruction with subchondral grafts and cement. *Chir Organi Mov (Suppl 1)*, 75:212–13, 1990.

[41] S. A. Bini, K. Gill, and J. O. Johnston. Giant cell tumor of bone. curettage and cement reconstruction. *Clin Orthop*, 321:245–50, 1995.

[42] F. V. Vult von Steyern, I. Kristiansson, K. Jonsson, P. Mannfolk, D. Heinegard, and A. Rydholm. Giant-cell tumour of the knee: the condition of the cartilage after treatment by curettage and cementing. *J Bone Joint Surg Br*, 88(3):361–65, 2007.

[43] H. R. Bucholz, A. Carlton, and R.E. Holmes. Hydroxyapatite and tricalcium phosphate bone graft substitutes. *Orthop Clin North Am*, 18:323–34, 1987.

[44] M. Itokazu, T. Matsunaga, M. Ishii, H. Kusakabe, and Y. Wyni. Use of arthroscopy and interporous hydroxyapatite as a bone graft substitute in tibial plateau fractures. *Arch Orthop Trauma Surg*, 115(1):45–8, 1996.

[45] A. Matsumine, A. Myoui, K. Kusuzaki, N. Araki, M. Seto, H. Yoshikawa, and A. Uchida. Calcium hydroxyapatite ceramic implants in bone tumour surgery. a long-term follow-up study. *J Bone Joint Surg Br*, 86(5):719–25, 2004.

[46] P. Laquerriere, A. Grandjean-Laquerriere, E. Jallot, G. Balossier, P. Frayssinet, and M. Guenounou. Importance of hydroxyapatite particles characteristics on cytokines production by human monocytes in vitro. *Biomaterials*, 24(26):2739–47, 2003.

[47] A. Grandjean-Laquerriere, O. Tabary, J. Jacquot, D. Richard, P. Frayssinet, M. Guenounou, D. Laurent-Maquin, P. Laquerriere, and S. Gangloff. Involvement of toll-like receptor 4 in the inflammatory reaction induced by hydroxyapatite particles. *Biomaterials*, 28(3):400–4, 2007.

[48] M. Hirata, H. Murata, H. Takeshita, T. Sakabe, Y. Tsuji, and T. Kubo. Use of purified beta-tricalcium phosphate for filling defects after curettage of benign bone tumours. *Int Orthop*, 30(6):510–13, 2006.

[49] M. Hirn, U. de Silva, S. Sidharthan, R. J. Grimer, A. Abudu, R. M. Tillman, and S. R. Carter. Bone defects following curettage do not necessarily need augmentation. *Acta Orthop*, 80(1):4–8, 2009.

[50] T. Yanagawa, H. Watanabe, T. Shinozaki, and K. Takagishi. Curettage of benign bone tumors without grafts gives sufficient bone strength. *Acta Orthop*, 80(1):9–13, 2009.

[51] A. Kreicbergs, P. A. Lönnqvist, and B. Nilsson. Curettage of benign lesions of bone. *Int Orthop*, 8:287–94, 1985.

[52] J. Elfar, R. M. Menorca, J. D. Reed, and S. Stanbury. Composite bone models in orthopaedic surgery research and education. *J Am Acad Orthop Surg*, 22(2):111–20, 2014.

[53] A. K. Singh, R. C. Sharma, R. K. Sharma, and D. M. Musmade. Challenges in cadaver availability for learning and research in medical sciences. *International Journal of Medical and Clinical Research*, 2(2):67–71, 2011.

[54] R. Hulkower. From sacrilege to privilege: the tale of body procurement for anatomical dissection in the united states. *The Einstein Journal of Biology and Medicine*, 27(1):23–26, 2011.

[55] J. A. Szivek, M. Weng, and R. Karpman. Variability in the torsional and bending response of a commercially available composite "femur". *J Appl Biomater*, 1(2):183–186, 1990.

[56] J. A. Szivek, M. Thomas, and J. B. Benjamin. Technical note. characterization of a synthetic foam as a model for human cancellous bone. *J Appl Biomater*, 4(3):269–272, 1993.

[57] M. Martens, R. Van Audekercke, P. Delport, P. De Meester, and J. C. Mulier. The mechanical characteristics of cancellous bone at the upper femoral region. *J Biomech*, 16(12):971–83, 1983.

[58] MatWeb: *Material Property Data*. Sawbones second-generation simulated cortical bone, March 2013. Available from: http://www.matweb.com/search/datasheet.aspx?matguid=82d1e15c662d4c97b75df5e9d9171da9ckck=1.

[59] J. A. Szivek and R. L. Gealer. Comparison of the deformation response of synthetic and cadaveric femora during simulated one-legged stance. *J Appl Biomater*, 2(4):277–80, 1991.

[60] L. Cristofolini, M. Viceconti, A. Cappello, and A. Toni. Mechanical validation of whole bone composite femur models. *J Biomech*, 29(4):525–35, 1996.

[61] L. Cristofolini and M. Viceconti. Mechanical validation of whole bone composite tibia models. *J Biomech*, 33(3):279–88, 2000.

[62] A. D. Heiner and T. D. Brown. Structural properties of a new design of composite replicate femurs and tibias. *J Biomech*, 34(6):773–81, 2001.

[63] MatWeb: *Material Property Data*. Sawbones third-generation simulated cortical bone, March 2013. Available from: http://www.matweb.com/search/datasheet.aspx?MatGUID=d622f0334d7c4d10987783ab235ed379.

[64] Pacific Research Laboratories Inc. Sawbones product catalogue, March 2013. Available from: http://www.sawbones.com/catalog/pdf/uscatalog.pdf.

[65] A. C. Chong, F. Miller, M. Buxton, and E. A. Friis. Fracture toughness and fatigue crack propagation rate of short fiber reinforced epoxy composites for analogue cortical bone. *J Biomech Eng*, 129(4):487–93, 2007.

[66] ASTM International. About astm international, March 2013. Available from http://www.astm.org/ABOUT/overview.html.

[67] A. D. Heiner. Structural properties of fourth-generation composite femurs and tibias. *J Biomech*, 41(15):3282–4, 2008.

[68] M. P. Gardner, A. C. Chong, A. G. Pollock, and P. H. Wooley. Mechanical evaluation of large-size fourth-generation composite femur and tibia models. *Ann Biomed Eng*, 38(3):613–20, 2010.

[69] A. H. Burstein, D. T. Reilly, and M. Martens. Aging of bone tissue: mechanical properties. *J Bone Joint Surg Am*, 58(1):82–6, 1976.

[70] X. Wang and S. Puram. The toughness of cortical bone and its relationship with age. *Ann Biomed Eng*, 32(1):123–35, 2004.

[71] D. T. Reilly and A. H. Burstein. The elastic and ultimate properties of compact bone tissue. *J Biomech*, 8(6):393–405, 1975.

[72] A. C. Chong, E. A. Friis, G. P. Ballard, P. J. Czuwala, and F. W. Cooke. Fatigue performance of composite analogue femur constructs under high activity loading. *Ann Biomed Eng*, 35(7):1196–205, 2007.

[73] R. Zdero, M. Olsen, H. Bougherara, and E. H. Schemitsch. Cancellous bone screw purchase: a comparison of synthetic femurs, human femurs, and finite element analysis. *Proc Inst Mech Eng H*, 222(8):1175–83, 2008.

[74] D.L. Logan. *A First Course in the Finite Element Method*. Nelson, a division of Thomson Canada Learning, 1120 Birchmount Road, Toronto, Ontario M1K 5G4 Canada, 4th edition, 2007.

[75] J. A. Hipp, N. Edgerton, K, and W. C. Hayes. Structural consequences of transcortical holes in long bones loaded in torsion. *J Biomech*, 23(12):1261–68, 1990.

[76] J. H. Keyak, J. M. Meagher, H. B. Skinner, and C. D. Mote Jr. Automated three-dimensional finite element modeling of bone: A new method. *J Biomed Eng*, 12:389–397, 1990.

[77] J. H. Keyak, S. A. Rossi, K. A. Jones, and H. B. Skinner. Prediction of femoral fracture loads using automated finite element modeling. *J Biomech*, 31:125–133, 1998.

[78] J. H. Keyak. Improved prediction of proximal femoral fracture load using nonlinear finite element models. *Med Eng Phys*, 23:165–173, 2001.

[79] J. H. Keyak and Y. Falkenstein. Comparison of in situ and in vitro ct scan-based finite element model predictions of proximal femoral fracture load. *Med Eng Phys*, 25:781–787, 2003.

[80] J. H. Keyak, T. S. Kaneko, S. A. Rossi, M. R. Pejcic, J. Tehranzadeh, and H. B. Skinner. Predicting the strength of femoral shafts with and without metastatic lesions. *Clin Orthop Relat Res*, 439:161–170, Oct 2005.

[81] M. Viceconti, M. Casali, B. Massari, L. Cristofolini, S. Bassini, and A. Toni. The 'standardized femur program' proposal for a reference geometry to be used for the creation of finite element models of the femur. *J Biomech*, 29(9):1241, 1996.

[82] G. Cheung, P. Zalzal, M. Bhandari, J. K. Spelt, and M. Papini. Finite element analysis of a femoral retrograde intramedullary nail subject to gait loading. *Med Eng Phys*, 26(2):93–108, Mar 2004.

[83] The Bel Repository. The standardized femur solid model, 2003. Available from: https://www.biomedtown.org/biomedtown/LHDL/Reception/datarepository/repositories/BelRepWikiPages/FrontPage.

[84] M. Papini, R. Zdero, E. H. Schemitsch, and P. Zalzal. The biomechanics of human femurs in axial and torsional loading: comparison of finite element analysis, human cadaveric femurs, and synthetic femurs. *J Biomech Eng*, 129(1):12–9, 2007.

[85] C. Salas, D. Mercer, T. A. DeCoster, and M. M. Reda Taha. Experimental and probabilistic analysis of distal femoral periprosthetic fracture: a comparsion of locking plate and intramedullary nail fixation. part a: experimental investigation. *Comput Methods Biomech Biomed Engin*, 14(2):157–64, Feb 2011.

[86] R. C. Johnston and G. L Smidt. Measurement of hip-joint motion during walking. *J Bone Joint Surg Am*, 51(6):899–907, 1974.

[87] J Lemaitre and J.-L. Chaboche. *Mechancis of Solid Materials*. Cambridge University Press, Cambridge, UK, 1990.

[88] G. Tao and Z. Xia. Mean stress/strain effect on fatigue behavior of an epoxy resin. *Int J Fatigue*, 29(12):2180–90, 2007.

[89] J.L. Jordan and J.E. Spowart. Comparison of mechanical properties of polymer-based multi-phase particulate composites. In V. Chalivendra, B. Song, and D. Casem, editors, *Dynamic Behavior of Materials*, volume 1, pages 317–320. Society for Experimental Mechanics, Inc., 2013.

[90] B. Song, W. Chen, S.T. Montgomery, and M.J. Forrestal. Mechanical response of an alumina-filled epoxy at various strain rates. *J Comp Mater*, 43(14):1519–36, 2009.

[91] P. J. Nowotarski, B. Ervin, B. Weatherby, J. Pettit, R. Goulet, and B. Norris. Biomechanical analysis of a novel femoral neck locking plate for treatment of vertical shear pauwel's type c femoral neck fractures. *Injury*, 43(6):802–6, 2012.

[92] A. G. Tsai, M. S. Reich, J. Bensusan, T. Ashworth, E. M. Randall, and O. Akkus. A fatigue loading model for investigation of iatrogenic subtrochanteric fractures of the femur. *Clin Biomech*, 28(9–10):981–7, 2013.

[93] C. C. Wu and C. L. Tai. Retrograde nailing of a femoral supracondyle. *Orthopedics*, 35(4):e491–496, 2012.

[94] C. Salas. *A Biomechanical Comparison of Locking Plates Contrasted with Intramedullary Treatment of Distal Femur Fracture*. Thesis, 2008.

[95] Smooth-On. Smooth-cast 320 series technical overview, 2011. http://www.smooth-on.com/tb/files/Smooth-Cast_320,_321,_322.pdf.

[96] R. Zdero, S. Rose, E. H. Schemitsch, and M. Papini. Cancellous screw pull-out strength and effective shear stress in synthetic third generation composite femurs. *J Biomech Eng*, 129(2):289–293, 2007.

[97] W.F. Lyon, J.R. Cochran, and L. Smith. Actual holding power of various screws in bone. *Ann Surg*, 114:376–384, 1941.

[98] F. W. Baumgart, J. Cordey, K. Morikawa, S. M. Perren, B. A. Rahn, R. Schavan, and S. Snyder. Ao/asif self tapping screws (sts). *Injury Sup.*, 1:S1–S17, 1993.

[99] R. Bolliger Neto, J. D. M. B. Alvarenga Rossi, and T. P. Leivas. Experimental determination of bone cortex holding power of orthopedic screw. *Rev. Hosp. Clin. Fac. Med. Sao Paulo*, 54(6):181–186, 1999.

[100] C. Salas, D. Mercer, T. A. DeCoster, and M. M. Reda Taha. Experimental and probabilistic analysis of distal femoral periprosthetic fracture: a comparsion of locking plate and intramedullary nail fixation. part b: probabilistic investigation. *Comput Methods Biomech Biomed Engin*, 14(2):175–82, Feb 2011.